Dissertation
submitted to the
Combined Faculties for the Natural Sciences and for Mathematics
of the Ruperto-Carola University of Heidelberg, Germany
for the degree of
Doctor of Natural Sciences

Put forward by

Dipl.Phys. Steffen Brinkmann

born in Wesel

oral examination: 7.7.2009

On the numerical simulation of advection dominated accretion flows

Referees:

Prof. Dr. Max Camenzind
Priv.Doz. Dr. Hubert Klahr

Steffen Brinkmann: *On the numerical simulation of advection dominated accretion flows*, Dissertation submitted to the Combined Faculties for the Natural Sciences and for Mathematics of the Ruperto-Carola University of Heidelberg, Germany for the degree of Doctor of Natural Sciences, © 2009

Abstract / Zusammenfassung:

On the numerical simulation of advection dominated accretion flows

In accreting systems of low accretion rate (< 1% Eddington rate) the accretion is dominated by advection rather than by radiation or thermal convection. This type of accretion flow is assumed to cause the observational signatures of quiescent galaxies, X-ray binaries in the low-hard state and other compact objects. The motor that maintains the transport of angular momentum and accretion is the magnetorotational instability fed by the shearing of the magnetic field in the differential rotation of the disc. Direct observation of these objects is difficult due to their small size and because they are often hidden behind accreting matter. Therefore simulating the equations of ideal magnetohydrodynamics is necessary to investigate the structure and dynamics of these accretion flows.

We carried out direct numerical simulations of an accreting torus around a black hole. By performing tests varying the initial magnetisation, the size and position of the torus and the geometry of the magnetic field, we found the crucial parameters that determine accretion and ejection. The results show that the initial geometry of the magnetic field is of almost no relevance for the long term behaviour. However, if the magnetic field strength is to small, no fast outflow arises. Also the presence of radiative cooling will inhibit powerful ejections. Moreover we report retrograde rotation of the jet with respect to the disc rotation.

Über die numerische Simulation advektionsdominierter Akkretionsflüsse

In akkretierenden Systemen niedriger Akkretionsrate (< 1% der Eddington-Rate) wird der Akkretionsfluss durch Advektion dominiert und nicht durch Wechselwirkung mit Strahlung oder thermischer Konvektion. Dieser Akkretionstyp wird gemeinhin für die beobachteten Eigenschaften von inaktiven Galaxien, Röntgen-Doppelsternen im „Low-Hard-State“ und anderen kompakten Objekten verantwortlich gemacht. Der Mechanismus, der den Drehimpulstransport und damit die Akkretion aufrechterhält, ist die Magnetorotationsinstabilität. Diese wird durch die Scherung des Magnetfeldes in der differenziell rotierenden Scheibe erzeugt. Die direkte Beobachtung dieser Objekte ist schwierig aufgrund ihrer geringen Größe und weil sie häufig hinter dem akkretierenden Material verborgen sind. Daher ist es notwendig, magnetohydrodynamische Simulationen dieser Objekte zu erstellen, um ihre Dynamik und Struktur zu erforschen.

Wir haben direkte numerische Simulationen eines Akkretionstorus durchgeführt, in denen wir verschiedene Anfangszustände getestet haben. Durch Variation der Position und Größe des Torus, seiner Magnetisierung und der Geometrie des Magnetfeldes, konnten wir die wesentlichen Parameter für die globale Struktur ausmachen. Es zeigt sich, dass die Geometrie des anfänglichen Magnetfeldes irrelevant für die Langzeitentwicklung der Simulation ist. Wenn das Magnetfeld jedoch zu schwach ist, wird kein schneller, Jet-artiger Materiefluss gebildet. Kühlung durch Abstrahlung verhindert ebenfalls starke Ausflüsse. Außerdem fanden wir retrograde Rotation des Jets bezüglich der Scheibenrotation.

God is always there. But you got to do the footwork.
Mike 'Flea' Balzary

Contents

List of Figures

List of Tables

Black hole sun
won't you come
to wash away the rain.

— Chris Cornell

1 Introduction

Gravity was the first of the four forces known to mankind. Soon after its basic laws were discovered by Kepler and Galilei, a theory of the formation of the solar system was put forward by Descartes (1664). He supposed that an 'universal fluid' formed vortices around stars. In these rotating objects, more vortices formed giving rise to planets and their satellites . This is probably the first scientific mention of an accretion[1] process. The idea of accretion discs was born when Kant (1755), using Newtonian mechanics, showed that a collapsing gas cloud would flatten.

Also the fact that accreting matter would gain internal energy which is eventually emitted was addressed as a possible solution to the problem of the sun's energy. 1854 Hermann von Helmholtz held a speech *On the interactions of the natural forces and the newest investigations relating to* proposing that gravitational energy freed by compression could account for the origin of the sun's heat (von Helmholtz, 1896). This hypothesis was soon disapproved by palaeontological findings which indicated that the earth and therefore the sun was much older than predicted by Helmholtz' contraction theory; but it is the first reference of accretion as a dissipating process.

The discovery of nuclear forces and especially of the mechanism of nuclear fusion (Bethe and Critchfield, 1938) marked the preliminary end of the scientific exploration of accretion physics. Since then fusion of mostly hydrogen nuclei was thought to be the direct or indirect source of any emission of light in the universe.

[1] from Latin *accretio*: growth, increase

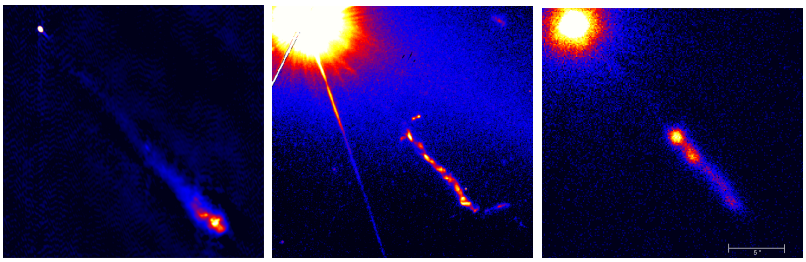

Figure 1.1 – Quasar 3C 273. *The panels show radio, optical and X-ray images of 3C 273 and its jet taken by MERLIN, HST (NASA/STScI) and Chandra (NASA/CXC/SAO) respectively.*

1.1 Accretion physics in the 20th century

In the late 1950's quasi stellar radio sources ('Quasars') were discovered. 1963, Schmidt reported that 3C 273(fig. 1.1), a quasar discovered in 1959, had a redshift of $z = 0.158$. He interpreted that either 3C 273 was a compact star and the redshift was due to gravity or it was the nuclear region of a distant galaxy whose emission lines showed cosmological redshift. The former case was incompatible with the occurrence of permitted and forbidden lines with the same redshift so the author favoured the latter explanation.

For that case he concluded: '*The distance would be around 500 megaparsecs, and the diameter of the nuclear region would have to be less than 1 kiloparsec. This nuclear region would be about 100 times brighter optically than the luminous galaxies which have been identified with radio sources so far... The total energy radiated in the optical range at constant luminosity would be of the order of* 10^{59} *ergs*'

Today we know that assuming isotropic emission, the luminosity of 3C 273 is of the order of 10^{47} erg/s (Ulrich, 1981), resulting in an absolute magnitude of -26.7. We could not ascertain why Schmidt misjudged the luminosity by 12 orders of magnitude.

The most simple and by now widely accepted explication of this high luminosity from such small regions is that energy is emitted due to accretion of matter by a compact object at its centre (Salpeter, 1964). The time scales of periodic variations give upper limits for the size of this object, giving strong evidence that it is a blck hole.

The efficiency of accretion onto a compact object, i.e. the energy emitted per mass m is several orders of magnitude higher than that of nuclear processes such as fusion. The nucleosynthesis of 4 hydrogen nuclei to one helium nucleus occurs with an efficiency of

$$\eta_{\text{fusion}} = \frac{\Delta E_{4\text{H}\to\text{He}}}{4mc^2} = \frac{4m_{\text{p}} - m_\alpha}{4m_{\text{p}}} \approx 0.007.$$

The efficiency obtained by accretion on the other hand depends on the compactness of the central object:

$$\eta_{\text{accretion}} = \frac{\Delta E_{\text{grav}}}{mc^2} = \frac{GMm}{R_* mc^2} = \frac{R_{\text{g}}}{R_*},$$

where

$$R_{\text{g}} = GM/c^2$$

is the gravitational radius of a black hole of mass M and R_* is the surface or horizon of the accreting object. This is just an estimate as time scales on which both processes happen are not taken into account. Even for white dwarfs for which $\eta_{\text{fusion}}/\eta_{\text{accretion}} \approx 50$, accretion can be an important source of observed radiation (Frank *et al.*, 1985).

In the following sections we will take a closer look at the different observed astronomical objects which are referred to as accreting objects.

1.1.1 Active galactic nuclei

Active galactic nuclei (AGN) are centres of galaxies emitting over the entire range of the light spectrum and representing the most luminous steady sources of radiation in the universe. They can reach an absolute luminosity of $10^{47}\,\text{erg/s}$ which is emitted from a region with a diameter of the order of a light-day ($\approx 10^2\,\text{AU}$)[2]. This power corresponds to the Eddington luminosity of an accretor of $10^9\,\text{M}_\odot$. The accretion rate needed to achieve this luminosity is of the order of $1\,\text{M}_\odot/\text{yr}$.

A whole zoo of astronomical objects is referred to as AGN: *Quasars* (quasi-stellar radio sources), *Seyfert galaxies* (radio quiet AGN with weak jets) and *Blazars* (centres of elliptical galaxies with high-energetic gamma emission) just to name a few. Apparently all of these objects can be unified to a standard model put forward by Begelman (1986); Lawrence (1987); Urry and Padovani (1995) and others which is illustrated in figure 1.2. According to this model all AGN consist of

1. **a supermassive rotating black hole at the centre of a host galaxy.** The compactness of the light emitting region (derived from variability timescale studies) and the luminosity and energy of the emitted light points strongly to a black hole with a mass of more than $10^8\,\text{M}_\odot$ as the central object. As interstellar matter is accreted during the active phase, the black hole is expected to spin up quickly.

2. **an accretion disc around the central black hole.** As matter is dragged into the black hole by gravitational forces, its angular momentum is forcing it to form a disc. Turbulent processes and winds

[2] AU = astronomical unit $\approx 1.5 \cdot 10^1 3\,\text{cm}$

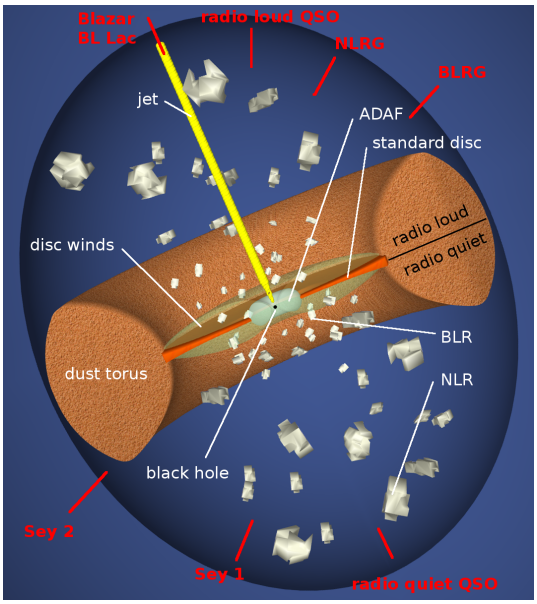

Figure 1.2 – Illustration of the standard model of AGN. *The unified model for radio loud (upper half) and radio quiet (lower half) AGN is shown (Urry and Padovani, 1995, based on fig. 1). The constituents of the AGN are denoted in white (ADAF: advection dominated accretion flow, BLR: broad line region, NRL: narrow line region), while lines of sight and the apparent astronomical object are typed in red (NLRG: narrow line radio galaxy, BLRG: broad line radio galaxy, Sey 1/2: Seyfert galaxy of type 1/2). Figure by J. Aragón and S. Brinkmann.*

transport angular momentum outwards, allowing matter to fall further inwards.

3. **an opaque dust torus at approximately** $10^4\,\mathrm{R_g}$**.** This is the mass reservoir for accretion and can contain up to $5{\cdot}10^6\,\mathrm{M_\odot}$ (Hatziminaoglou *et al.*, 2008). It is composed of warm ($10\,\mathrm{K} < T < 1500\,\mathrm{K}$) dust which will absorb most of the UV–, X– and γ- radiation emitted by the central region and emit this energy in the infrared band mainly as thermal black body radiation.

Arising from the accretion action all AGN show more or less powerful *jets*, well collimated, highly relativistic, bipolar beams of matter. Jets are either observed directly (type FR-I) or indirectly due to their bow shock (type FR-II) as classified by Fanaroff and Riley (1974).

The spectra of AGN are continuous with so called *bumps* in the infrared band due to star formation and the dust torus, in the blue band ('*Big Blue Bump*') due to multicolour black body radiation from the accretion disc and in the high energy regions of the spectrum above 1 keV caused by reflection at the hot inner accretion disc and due to inverse Compton scattering of photons by high energy electrons.

1.1.2 X-ray binaries

X-ray binaries (fig. 1.3) are binary stars with a pronounced emission in the X-ray band. They were discovered in 1962 after launching three Geiger counters to a height of 225 km and observing the X-ray sky for less than

***Figure 1.3** – **Artistic illustration of an X-ray binary.** The compact companion to the right is hidden inside a (tilted) accretion disc (in dark blue) and a hot corona (orange). Courtesy of I. Brinkmann.*

6 minutes (Giacconi *et al.*, 1962). Soon after, Shklovskii (1967) proposed a theoretical model widely accepted today: they consist of a white dwarf, neutron star or black hole which accretes from a main sequence or giant companion star. The high-energy radiation is produced in a hot region close to the accreting companion referred to as the *corona*. The exact location of the corona remains unclear. The most common assumption is that it is located above and below the accretion disc and contains hot ($\gtrsim 10^9\,\mathrm{K}$) plasma.

X-ray binaries radiate at luminosities of $10^{33} - 10^{38}\,\mathrm{erg/s}$ and are mainly located close to the galactic plane. All the sources are found to be highly variable on timescales ranging from milliseconds to years and both random and periodic patterns are observed (Shapiro and Teukolsky, 1983).

Cygnus X-1 for instance – probably one of the most studied X-ray sources in the sky – exhibits the whole range of variability timescales, a very prominent one being its *1ms-bursts* (Oda, 1977). This sets an upper limit to the active region of $r \lesssim 300\,\mathrm{km}$. This corresponds to about $20\,\mathrm{R_g}$ for an assumed mass of approximately $8\,\mathrm{M_\odot}$. As the maximum mass for a stable neutron star is of the order of $2\,\mathrm{M_\odot}$ Cygnus X-1 is considered to be almost certainly a black hole.

X-ray binaries have much in common with their huge relatives, the AGN, which is why they are also called *microquasars*. They show a similar continuous spectrum with a pronounced high energy bump. Depending on the presence or absence of the most energetic arm ($> 10\,\mathrm{keV}$) and the overall X-ray luminosity of the object, X-ray binaries are divided into different *states* (figure 1.4, Remillard and McClintock (2006)). (1) *thermal* or *high-soft-state*: dominant black-body component, shifted only in the high energy regime by non thermal emission. (2) *low-hard*– and *very hard* state: dominant non thermal component, weak thermal component. The exponent of the spectral

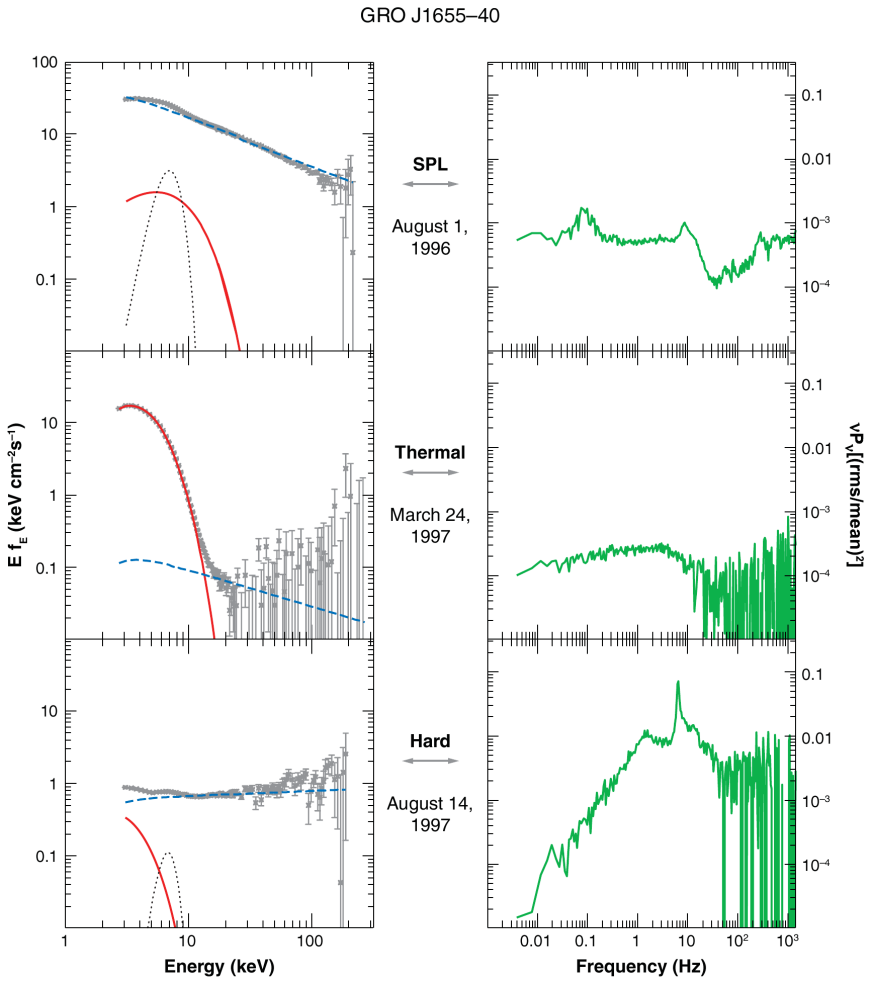

Figure 1.4 – Spectra of black hole binary GRO J1655-40. *The left hand panels show sample spectra for the* steep power law *(SPL also referred to as 'very high state'), the* thermal *(=high-soft) and the (low-)*hard *state. The energy distributions are decomposed into the main components: thermal (solid red), power-law (blue dashed) and relativistically broadened Fe Kα line (dotted black). The right panels plot the power density spectrum. Figure by Remillard and McClintock (2006)*

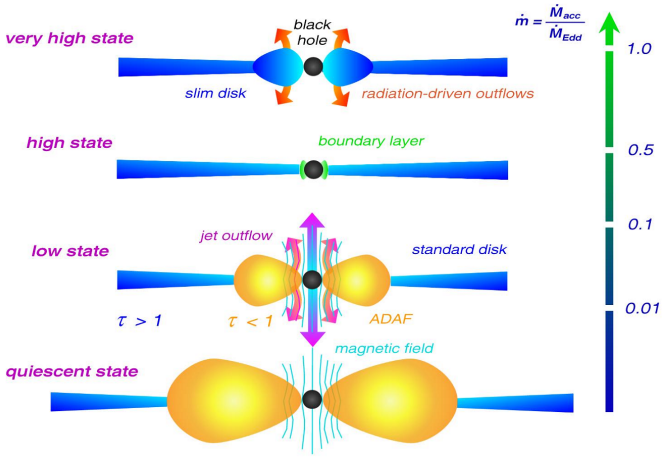

Figure 1.5 – Illustration of the spectral states of black hole accretion discs. *The figure shows the different spectral states found in X-ray binaries and AGN. The right axis gives an approximate scale of the accretion rate in terms of the Eddington accretion limit. Figure by Müller (2004).*

power law in the very hard state is $\alpha < -1$. This state is therefore also referred to as *steep power law* state.

The widely accepted explication for the different spectral states is based in the presence or absence of two types of accretion discs: an optically thick disc at large radii heats up as matter falls inwards. When the temperature is high enough ($> 10^5$ K), the medium is ionised and becomes optically thin. This makes efficient cooling by black body radiation impossible. The disc expands and forms an optically thin accretion torus close to the black hole. In this regime, magnetic fields are a dominant dynamic component of the fluid. Whether the thick disc or the thin torus is dominant and at which radius the transition from one to the other occurs determines the spectral state of the accretor (figure 1.5).

These states are not permanent properties of the X-ray binaries. They rather change their state in a periodic manner. Fender *et al.* (2004) unified the observations of the changing spectra of X-ray binaries into one model illustrated in figure 1.6. In this picture, an initially weakly emitting object in the low-hard-state increases its luminosity by enhanced accretion. Reaching a critical point, the object emits an outburst in the radio and X-ray band. This is associated with a powerful event in the jet such as an internal shock. Subsequently the radio emission decreases steeply and the object passes to the high-soft state which eventually transforms into a low-soft-state when the accretion rate decreases again.

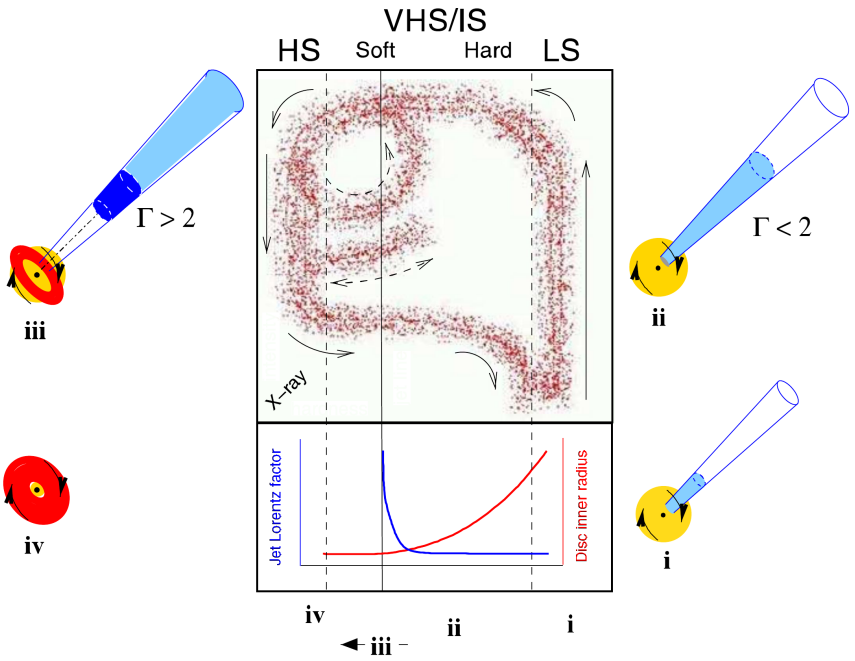

Figure 1.6* – *Schematic of our simplified model for the jet-disc coupling in black hole binaries. *The upper central box panel represents an X-ray hardness-intensity diagram (HID); 'HS' indicates the 'high/soft state', 'VHS/IS' the 'very high/intermediate state', and 'LS' the 'low/hard state'. In this diagram, X-ray hardness increases to the right and intensity upwards. The lower panel indicates the variation of the bulk Lorentz factor γ of the outflow with hardness — in the LS and hard VHS/IS the jet is steady with an almost constant bulk Lorentz factor $\gamma < 2$, progressing from state i to state ii as the luminosity increases. At some point — usually corresponding to the peak of the VHS/IS — γ increases rapidly, producing an internal shock in the outflow (state iii) followed in general by cessation of jet production in a disc-dominated HS (state iv). At this stage fading optically thin radio emission is only associated with a jet/shock which is now physically decoupled from the central engine. As a result the solid arrows indicate the track of a simple X-ray transient outburst with a single optically thin jet production episode. The dashed loop and dotted track indicate the paths that GRS 1915+105 and some other transients take in repeatedly hardening and then crossing zone iii — the 'jet line' — from left to right, producing further optically thin radio outbursts. The sketches around the outside illustrate our concept of the relative contributions of jet (blue), 'corona' (yellow) and accretion disc (red) at these different stages. Figure and description by Fender* et al. *(2004).*

1.1.3 Young stellar objects

Interstellar molecular hydrogen clouds, mainly located in the spiral arms, eventually collapse under the influence of their own gravity if the cloud exceeds the Jeans mass

$$M_{\mathrm{J}} = \frac{1}{\sqrt{\rho}} \left(\frac{\pi \mathcal{R} T}{\mu G} \right)^{3/2} . \tag{1.1}$$

The central core heats up adiabatically to a few thousand K and the molecular hydrogen dissociates. After the core contracts and forms a hydrostatic protostar and the shocked infalling material heats its surface up to $10^6\,\mathrm{K}$. Due to the angular momentum conservation the accreted material forms a ring with a mean radius of

$$R = 10\,\mathrm{AU} \left(\frac{\ell}{10^{20}\,\mathrm{cm^2/s}} \right)^2 \left(\frac{M_\odot}{M_*} \right), \tag{1.2}$$

M_* being the mass of the protostar and ℓ the specific angular momentum. Typical accretion rates are of the order of $10^{-8}\,M_\odot/\mathrm{yr}$ (Hartmann *et al.*, 1998; Muzerolle *et al.*, 2005).

At that stage the protostar is hidden behind cold gas ($\approx 10\,\mathrm{K}$). They are only visible in the radio band and are referred to as class 0 objects. After about $10^5\,\mathrm{yr}$ the stellar wind has sweeped the environment. Now the hot dust and the disc become visible in the infrared band (class I objects). About a million years later the hot dust has been blown away by the stellar wind and only the star and its disc are visible. At this stage protostars are named after the first observed star of this type *T Tauri star* or class II.

In T Tauri stars deuterium burning has started and they produce a strong wind which completely cleans the surroundings of the star so that it is visible optically.

1.2 The physics behind accretion

In section 1.1 we pointed out the discoveries which led to the insight that accretion was responsible for the brightest sources in the universe. However the question *why* matter accretes, i.e. *how* angular momentum is carried outwards remains unanswered.

Microscopic viscosity was ruled out early (von Weizsäcker, 1943, 1948; Lüst, 1952), because the resulting timescales exceed the Hubble time. At age 24, Velikhov (1959) explored the criteria for stability of rotating conducting fluids. The contrary interpretation as an instability that could enhance angular momentum transport was not taken into account. Also Chandrasekhar (1960, 1961) published the effect which as we now know strongly expedites accretion as a condition for stability. The hydromagnetic instability was but

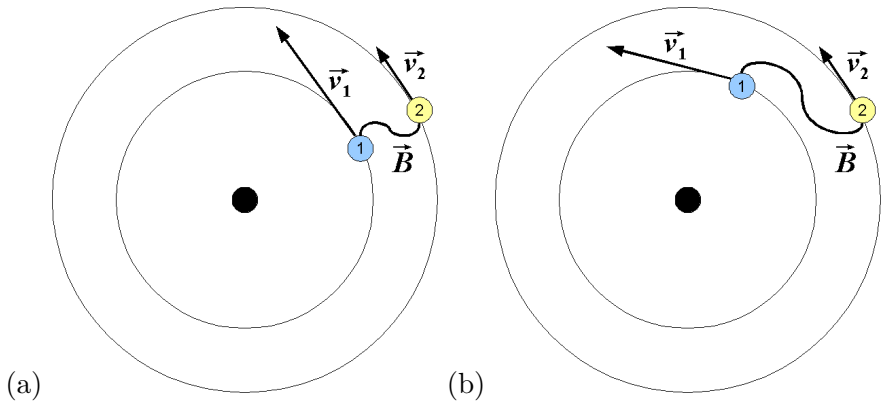

Figure 1.7 – Illustration of the MRI. *Two fluid elements orbit with their Keplerian velocities connected by a magnetic field line (a). The inner one (1, blue) will advance due to its larger velocity (b). If the magnetic field is weak, it will resist the shearing by accelerating the outer (2, yellow) and decelerating the inner particle. Therefore the outer particle gains angular momentum, while the inner one looses angular momentum. They separate radially which repeats and enhances the procedure.*

a merely academic case of the equations of magnetohydrodynamics (MHD) to coaxially rotating cylindrical flows of magnetised fluids. However the case of differentially rotating cylinders is the only case of magnetorotational instability (MRI) which was proven to exist in laboratory experiments (Rüdiger *et al.*, 2006).

In 1991 Balbus and Hawley assumed a perturbed vertical magnetic field in a Keplerian disc and found that the growth rate of the unstable modes is of the order of the local orbital frequency. Although this discovery is closely related to the stability criteria described by Velikhov and Chandrasekhar, it must be accounted an independent merit.

The effect of magnetic fields on a rotating plasma is twofold: on one hand, perturbations are enhanced exponentially by linear instability of the slow magnetosonic mode. This causes turbulence which can transport angular momentum locally (e.g. Bodo *et al.*, 2008) and globally (Mikhailovskii *et al.*, 2008). An analytical introduction to MRI is given in section 2.4. On the other hand radial-azimuthal magnetoviscous stress appears as a source of angular momentum transport The latter is often also referred to as MRI or mixed up with the actual instability. It is *not* an instability though.

Before the exact theory of the action of magnetic fields on accretion discs is derived in section 2.4, we will give an intuitive picture of how magnetorotational instability acts.

Assume two adjacent fluid elements (henceforth also referred to as particles) of a magnetised fluid in differential rotation ($\mathrm{d}\Omega/\mathrm{d}r < 0$) as usually found in astrophysical accretion discs. They reside on the same magnetic

field line. One can show that in the case infinite conductivity, the magnetic flux through the surface of a virtual tube comoving with the fluid vanishes (Biskamp, 1997). That means that the particles will tend to stay on their magnetic field line. In real plasmas it can happen, that a perturbation leads to a small radial separation of the fluid elements (fig. 1.7,(a)).

In that case the inner element will have a slightly distinct angular momentum than the outer one, assuming Keplerian rotation everywhere. Therefore, the inner particle rotates faster than its former companion and will advance azimuthally (fig. 1.7,(b)). The magnetic field by which they still are coupled will resist against this radial-azimuthal separation in two ways: on one hand magnetic field lines resist stretching which reverses the separation and thus has a stabilising effect. For strong magnetic fields, this effect dominates. On the other hand, the field lines resist shearing which results in an effective angular momentum gain of the outer particle and a loss of angular momentum for the inner particle. This leads to further radial separation of the fluid elements since the particels will tend to move towards an orbit according to their new angular momentum. This is a self-enhancing mechanism, and therefore an instability.

1.3 Jets and Winds

Angular momentum is carried away not only radially close to the equator but also vertically through winds and jets (Blandford and Payne, 1982; Casse, 2008). The existence of accretion discs on one hand and of outflows on the other hand seem to be tightly coupled. All of the known accreting systems present fast collimated outflows as well as slow spherical winds.

Depending on the compactness of the object, jets fall in one of two categories:

1. **Jets from compact objects:** Neutron stars and black holes (star sized X-ray binaries as well as AGN) exhibit fast jets with Lorentz factors of a few to hundreds. They are less dense than their ambient medium and reach out into space orders of magnitude further than the size of the originating system. For instance, the jet of 3C273 (figure 1.1) extends over approximately 57 kpc (Uchiyama *et al.*, 2006) while variability studies of the source indicate typical time scales of 10^{-1} to 1 yr which point to an approximate size of the ejection region of the order of 10^{-1} pc (Soldi *et al.*, 2008).

2. **Jets from protostellar sources:** Jets from early stage stars (Herbig-Haro objects) are denser than their surroundings and propagate at speeds of 10^2 to 10^3 km/s. Due to their moderate temperatures they

are observable via line emission giving information about the motion along the line of sight.

Whether these two types of jets are ejected by the same mechanisms is still unclear. The presented work aims at gaining insight into the first type as we are not simulating cool, optically thick discs as present in the vicinity of protostars.

Also one has to keep in mind that the angular resolution of observations is of the order of milliarcseconds (using 'Very Large Baseline Interferometry', VLBI). This corresponds to about $1000\,\mathrm{R_g}$ for the size and distance of M87, a prominent, well-studied AGN in the Virgo cluster. This is of the order of the simulated region in this work. Therefore few conclusions concerning the further propagation, i.e collimation and acceleration of the jet can be drawn from these simulations. We will nevertheless refer to fast outflows in our simulations as *jets* for the sake of simplicity.

1.4 State of the art

The compactness of accreting objects make their direct observation impossible. And not only that the apparent size of the accretors and their surroundings is unresolvable by present (and near future) telescopes; also they are either inactive or hidden behind thick clouds of dust and luminous coronae. Either way the regions where accretion actually happens are invisible. That makes numerical simulation the only possible way to 'observe' accretion in action.

Years before the structure of accretion flows and the underlying physical processes were understood, numerical simulations of these objects have already been carried out. The dynamics of accretion was investigated by n-body simulations (Lin and Pringle, 1976), as well as grid based codes (Sørensen *et al.*, 1975). Today the pile of publications on the subject goes far beyond the scope of this work. Nevertheless we will try and give an overview over the recent progress in numerical accretion physics.

Gracia et al. (2003) performed 1D simulations including radiative cooling and convective heat flux of the region where the optically thick standard disc turns into the optically thin advection dominated accretion flow (ADAF), the truncation radius. They found a quasi-periodic modulation of the mass flux in the domain and interpret their results as a possible explanation of the observed high frequency quasi periodic oscillations (HFQPO).

Turner et al. (2005) in continuation of their former work (Turner *et al.*, 2003), extended a Newtonian MHD code with a flux limiting scheme

treating radiative feedback in an optically thick medium as diffusion. They simulated a local patch of a geometrically thin accretion disc and found the previously predicted photon bubble instability (Arons, 1992). The effect of photon bubbles on the disc dynamics could not be greater; the disc collapses and cools in much less than a dynamical time scale. The global effects of this instability are still to be investigated, since MRI was suppressed by rigid rotation of the simulated patch.

Klahr and Kley (2006) applied the flux limited diffusion method to a hydrodynamic code to investigate the case of protoplanetary discs. They found that treating the thermodynamics correctly leads to pressure supported bubbles around the protoplanets rather than a thin circumplanetary disc.

Hawley et al. (2007) as a continuation of their former work (De Villiers and Hawley, 2003) described the dynamics of a torus made unstable by weak magnetic fields in GRMHD[3] simulations. They found an enhancement of the Maxwell stress due to the MRI even close to the black hole, where the standard disc model predicts an almost empty plunging region inside the radius of the marginally stable orbit at $r_{\mathrm{ms}} = 6GM/c^2$. Also they showed that accretion and jet emission are more efficient at higher spin of the black hole.

Fragile et al. (2007) also applied a GRMHD code but set up a tilted rotating black hole with respect to the axis of rotation of the accretion disc. It turns out that concerning most features, such as the dynamics of the plunging region close to the black hole, the tilted black hole behaves like a non tilted one with less spin. Apart from that there are effects which are rooted in the tilted black hole axis; the ejected jet precesses with a frequency of a few Hz per black hole mass (measured in solar masses). This is proposed to be an explication of the low frequency QPOs[4] observed in black hole accretion systems. As the jet axis precesses it crosses the line of sight of the observer resulting in frequent changes in the luminosity.

Zanni et al. (2007) employed a Newtonian code including resistivity and proved that jets can be accelerated by the magnetocentrifugal mechanism (Blandford and Payne, 1982) provided certain conditions of the magnetic resistivity and the initial field configuration are satisfied.

Goldston et al. (2005) used data from a non radiative simulation of a radiatively inefficient accretion flow by Igumenshchev *et al.* (2003) and

[3] GRMHD = general relativistic magnetohydrodynamics
[4] QPO = quasi periodic oscillation

post-process the synchrotron emission. They pose that their results are 'self-consistent because energy loss via radiation is negligible and does not modify the basic dynamics or structure of the accretion flow.'. This statement is going to be reassessed here.

Romanova et al. (2008) used a Newtonian code on e 'cubed sphere grid' investigated the interaction of a magnetised rotating star with an accretion disc. They found two distinct modes of accretion onto the star: (1) the unstable mode which results in stochastic accretion paths and (2) the stable mode where matter accretes along ordered streams showing a periodic behaviour.

McKinney and Blandford (2009) performed 3D GRMHD simulations of accretion discs and followed the jet out to $1000\,\mathrm{R_g}$. They tested a dipolar and a quadrupolar initial magnetic field and found that in the quadrupole case no strong jet ($\gamma \gtrsim 3$) is produced. Apart from a mainly dipolar field they find a large spin parameter a of the black hole to be crucial for jet production. This work is tightly related to the works of McKinney and Gammie (2004), McKinney (2006) and Beckwith *et al.* (2008).

1.5 Motivation

To gain insight in to the innermost regions of accreting object one has to rely on numerical simulations. Observations give hints about the structure and dynamics of the accretion discs via light curves and spectra but cannot resolved the region of interest. Another observational problem is that the accreting object is often hidden behind accreting matter.

Therefore many questions remain unanswered. To solve some of them we will carry on the previous work done by other researchers as well as our own (Brinkmann, 2004; Brinkmann *et al.*, 2008a,b) and simulate an advection dominated accretion torus around a black hole. Questions we aim to answer include:

- *Is it the effect of the instability or of the stress that is responsible for accretion?* Magnetic fields have two prominent effects on differentially rotating matter. (1) It enhances perturbations via the MRI and quickly leads to turbulence. Turbulence can transport angular momentum. (2) It transports angular momentum via magnetic stress in the r-ϕ-plane. These effects are tightly connected as they are direct results of the equations of MHD in rotating media. We will try and distinguish both effects in our results to give an answer to the posed question.

- *Under which circumstances does an accretion flow result in a (fast) outflow?* On the one hand, outflows are tightly coupled to the accretion process since they provide the channel of carrying away angular momentum. On the other hand, quiescent sources are observed which in their spectra show evidence for accretion discs but not for jets, as the radio-quiet quasars. We will aim to produce simulations with and without fast outflows to explore the physical origin of these.
- *Is there periodic behaviour such as oscillations or recurring features?* In most sources in the sky which are believed to be black hole accretors, periodic and quasi periodic changes in the luminosity have been found (van der Klis, 2000, 2005). The origin of these oscillations remains unknown. Therefore, we will check for periodic behaviour in our simulations.
- *Are the commonly used set-ups too artificial? Will small variations, specially towards more realistic initial configurations alter the result of a simulation?* The widely used set-ups of accretion discs resemble analytical models emulating ideal cases. These do not exist in nature. We want to test for how long the effects of the initial configuration determine the simulation results.
- *What is the effect of cooling on the accretion flow?* Most of the simulations in the literature do not implement interaction of radiation of any kind. We want to test the reliability of non radiative simulation.

1.6 Outline

In chapter 2 we will give an introduction to the theoretical bases which are needed for the investigation of accretion. This includes an introduction to the theory of accretion, the derivation of the governing equations and a their numerical treatment.

We will then focus on the numerical experiments we carried out. In chapter 3 the model case `QUAD` is described in section 3. It evolves an accretion flow close to the equatorial plane, slow spherical winds and a fast jet-like outflow. The fast outflow showed an unexpected periodical retrograde rotation. These features will be studied in detail. In chapter 4 we will alter single parameters of the setup to investigate their influence on the observed properties of the fluid in the simulated domain. Mainly the strength of the magnetic field and the implementation of a cooling term have a strong impact on the the presence or absence of the fast outflow and the efficiency of accretion.

In chapter 4.5 we will finally summarise our results and point out applications to open questions concerning microquasars and AGN.

An overview of the simulations is given in table 1.1.

name	description	section
QUAD	model case: quadrupole field, $r_{\mathrm{in}} = 20$, $r_{\rho_{\max}} = 30$, $\beta = 10^2$, axisymmetry	3
DIP	like QUAD but with dipole field	4.3
MULT	like QUAD but with arbitrary multipole field	4.3
NONMAG	like QUAD but without magnetic field	3
QUAD_15_23	like QUAD but with $r_{\mathrm{in}} = 15$ and $r_{\rho_{\max}} = 23$	4.1
QUAD_20_32	like QUAD but with $r_{\mathrm{in}} = 20$ and $r_{\rho_{\max}} = 32$	4.1
QUAD_30_42	like QUAD but with $r_{\mathrm{in}} = 30$ and $r_{\rho_{\max}} = 42$	4.1
QUAD_3D	like QUAD but with resolution $r \times \theta \times \phi = 256 \times 84 \times 42$	3
QUAD_BETA1.5	like QUAD but with $\beta = 10^{1.5}$	4.2
QUAD_BETA3	like QUAD but with $\beta = 10^3$	4.2
QUAD_MULT	like QUAD but with several radially stacked quadrupole fields	4.3
QUAD_SYN	like QUAD but with a energy sink term emulating synchrotron cooling	4.4
OCT	like QUAD but with octupole field	4.3
SEXT	like QUAD but with sextupole field	4.3

***Table 1.1** – **Summary of the simulation setups.** r_{in} and $r_{\rho_{\max}}$ denote the location of the inner brink and density maximum of the torus and β is the plasma parameter and equals $8\pi p_{\mathrm{gas}}/B^2$*

.

All energy flows according to the whims of the Great Magnet.

— Raoul Duke

2

Essential theory of the magnetohydrodynamics in accretion discs

We will now lay down the basics for understanding accretion and the physical processes leading to it. An analytic approach to predict accretion processes was made by Bondi and Eddington for spherical steady accretion flows. Their theories are introduced in section 2.1.

Soon it was understood that accreting matter will form discs and models for optically thick and optically thin discs were put forward. The most prominent ones, the so called standard disc and the advection dominated accretion flow (ADAF), are explained in section 2.2.

These discs need a potent way to remove angular momentum. Since viscous friction is ruled out due to its large time scale, turbulence was assumed to achieve the required angular momentum transport. The instability leading to the turbulence in the disc was soon found to be of magnetohydrodynamic nature. Therefore after deriving the equations of ideal MHD in the Newtonian as well as the relativistic frame in section 2.3, we can finally explore the magnetorotational instability MRI in section 2.4.

In order to perform numerical simulations of MHD, one has to discretise the governing system of equations. This can be done in numerous ways. In section 2.5 will present the bases of numerical MHD and introduce PLUTO, the code applied in this work.

Finally we will sum up the numerical set-up used for the simulations in section 2.6 and give examples for scaling our results to microquasars and AGN.

2.1 Spherical accretion

Accretion is the infall of matter onto a central object due to gravity[1]. The most simple set-up consists of a point mass in a homogeneous, non rotating, infinite cloud of perfect gas. For this case (Bondi, 1952) found a set of solutions for different values of the mass accretion $\dot{M}$. Only one solution is realistic as the others lead to singularities in the flow outside the horizon of the central object (Shapiro and Teukolsky, 1983). The physically relevant solution leads to a radial velocity increasing from 0 at $r = \infty$ to $v_\mathrm{r} = (2GM/r)^{1/2}$ for small radii. This leads to a constant mass flux which means

$$\frac{dM}{dt} \equiv \dot{M} = 4\pi r^2 \rho v_\mathrm{r} = constant$$

holds for every radius.

Bondi's solution does not take into account any feedback from radiation which is necessarily produced as gravitational energy is freed during the infall of matter.

A simple approach to include radiative feedback has earlier been done by Eddington (1925). He assumed Thompson scattering of photons on free electrons to provide an effectively outwards directed pressure which equilibrates gravitational pressure. Balancing these two forces on a neutral fluid element of mass $m_\mathrm{p} + m_\mathrm{e} \approx m_\mathrm{p}$ gives a limit on the luminosity, the *Eddington limit*

$$\mathcal{L}_\mathrm{Edd} = \frac{4\pi G M m_\mathrm{p} c}{\sigma_T} \approx 1.3 \cdot 10^{38} \left(\frac{M}{M_\odot}\right) \frac{erg}{s},$$

where σ_T is the Thompson cross section. Assuming that matter falls from infinity to the horizon of a black hole one finds the accretion rate limit, the *Eddington accretion rate*

$$\dot{M}_\mathrm{Edd} = \frac{\mathcal{L}_\mathrm{Edd}}{\eta c^2} \approx 1.4 \cdot 10^{17} \left(\frac{M}{M_\odot}\right) \frac{g}{s} \approx 2.2 \cdot 10^{-9} \left(\frac{M}{M_\odot}\right) \frac{M_\odot}{yr},$$

where η is the accretion efficiency. Typical values for η range between 0.01 and 0.5. Accretion rates and luminosity of accreting astrophysical objects are often measured in terms of the Eddington limits.

[1] This definition reflects the astrophysical meaning of accretion. Universally speaking any attracting force can lead to accretion. Also there are other meanings in the geologic, atmospheric and financial sciences.

2.2 Discs

In contrary to the assumption made in section 2.1 realistic gas clouds are neither homogeneous nor non rotating or infinite. Therefore as matter accretes, angular momentum will become dominant, while radial and vertical (i.e. parallel to the spin vector) velocities cancel out. The result is the formation of a disc, a fact first declared by Kuiper (1941). Once the matter moves on Keplerian orbits it needs to loose angular momentum to move further inwards. In other words, angular momentum has to be transported outwards. Momentum transport is usually done by some kind of viscosity. Nevertheless the microscopic viscosity is far to inefficient especially when the plasma is thin and hot (von Weizsäcker, 1943, 1948; Lüst, 1952).

A year after Kuiper proposed the existence of discs, a first hint to the solution of the angular momentum problem can be found in the literature: In his article *'On the Cosmogony of the Solar System'* Alfvén (1942) stated that

'It is found that ions and electrons within the limits of the planetary system are affected very much more by the sun's general magnetic field than by solar gravity. ...

The fact that the main part of the rotational momentum of the solar system belongs to the outer planets and not to the sun has constituted a crucial difficulty all cosmogonies of a Laplacian type. It is shown that this difficulty is removed if electromagnetic forces are introduces into the theory.

The study of the motion of ions and electrons in the sun's general magnetic field leads to a cosmogony of a new type'.

For several decades the physical effect leading to angular momentum transport remained unclear. Shakura and Sunyaev (1973) proposed that turbulence could achieve an effective removal of angular momentum through the disc. The nature of the turbulence was not specified. Almost 20 years later, Balbus and Hawley (1991) discovered the magnetorotational instability (MRI). It requires a weakly magnetised medium to be differentially rotating, two requisites present in probably all accreting systems.

To gain insight in the the processes leading to the MRI we will derive the equations of MHD in the following.

2.3 Magnetohydrodynamics

The mechanics of conducting fluids such as plasmas are governed by the MHD equations. In this section we will derive the equations of non relativistic and relativistic MHD. Our goal is to write the formulae in a form in which their conservative character is visible, i.e. following this scheme:

$$\partial_t U + \nabla F(U) = S_{\text{phys}}(U) + S_{\text{geo}}(U). \tag{2.1}$$

Here U is a conserved variable, $F(U)$ is the flux of this variable, $S_{\mathrm{phys}}(U)$ is a term describing physical sources and sinks (radiation, viscosity, resistivity) and will vanish in the ideal case by definition. $S_{\mathrm{geo}}(U)$ is a source term resulting from the choice of coordinates.

2.3.1 Ideal non relativistic MHD

The MHD equations arise from the combination of the equation of continuity,

$$\partial_{\mathrm{t}}\rho + \nabla \cdot (\rho \mathbf{v}) = 0, \tag{2.2}$$

the Navier-Stokes-equations of fluid dynamics

$$\partial_{\mathrm{t}}(\rho \mathbf{v}) + \nabla \cdot (\rho \mathbf{v} \otimes \mathbf{v} + p1) = 0, \tag{2.3}$$

($\otimes$ denotes the dyadic product, see equation B.1 and 1 is the unit matrix) and the Maxwell equations describing the macroscopic electric and magnetic fields $\mathbf{E}$ and $\mathbf{B}$

$$\nabla \cdot \mathbf{E} = 4\pi\rho \tag{2.4a}$$
$$\nabla \cdot \mathbf{B} = 0 \tag{2.4b}$$
$$\nabla \times \mathbf{E} = -\frac{1}{c}\partial_{\mathrm{t}}\mathbf{B} \tag{2.4c}$$
$$\nabla \times \mathbf{B} = \frac{1}{c}\partial_{\mathrm{t}}\mathbf{E} + \frac{4\pi}{c}\mathbf{J}, \tag{2.4d}$$

$\mathbf{J}$ being the total current density. which for non relativistic plasmas is given by Ohm's law:

$$\mathbf{J} = \sigma(\mathbf{E} + \mathbf{v} \times \mathbf{B}).$$

The **continuity equation** (2.2) is valid without modification because mass is conserved independently of the presence or absence of magnetic fields:

MHD: continuity equation

$$\partial_{\mathrm{t}}\rho + \nabla \cdot (\rho \mathbf{v}) = 0. \tag{2.2}$$

The **momentum balance** (2.3) has to be replenished by the electromagnetic forces acting on the fluid, namely the The Lorentz force

$$\mathbf{F}_{\mathrm{L}} = q\mathbf{E} + \frac{\mathbf{J}}{c} \times \mathbf{B}.$$

It can be shown that the ratio of electric to magnetic force is $\sim (v/c)^2$. Thus for the non relativistic case $v \ll c$, the electric force density $q\mathbf{E}$ and the

displacement current $\partial_t \mathbf{E}$ can be neglected and making use of equation (2.4b) and (2.4d) the electromagnetic force density yields

$$\begin{aligned}\mathbf{F}_L &= \frac{1}{4\pi}(\nabla \times \mathbf{B}) \times \mathbf{B} \\ &= \frac{1}{4\pi}(\mathbf{B} \cdot \nabla)\mathbf{B} - \nabla\left(\frac{B^2}{8\pi}\right) \\ &= \nabla \cdot \left(\frac{1}{4\pi}\mathbf{B} \otimes \mathbf{B} - \frac{B^2}{8\pi}1\right)\end{aligned}$$

Defining the total pressure $p_t = p + \frac{B^2}{8\pi}$ we can summarise the momentum equation of MHD:

MHD: momentum equation

$$\partial_t(\rho \mathbf{v}) + \nabla \cdot \left(\rho \mathbf{v} \otimes \mathbf{v} + p_t 1 - \frac{1}{4\pi}\mathbf{B} \otimes \mathbf{B}\right) = 0. \tag{2.5}$$

To derive the equation governing the **dynamics of the magnetic field**, we replace $\mathbf{J}$ in equation (2.4d) using Ohm's law (Jackson, 1975)

$$\mathbf{J} = \sigma\left(\mathbf{E} + \frac{\mathbf{v}}{c} \times \mathbf{B}\right)$$

(σ stands for the plasma conductivity) and, neglecting the displacement current, we get

$$\nabla \times \mathbf{B} = \frac{4\pi\sigma}{c}\left(\mathbf{E} + \frac{\mathbf{v}}{c} \times \mathbf{B}\right). \tag{2.6}$$

Computing the curl of equation (2.6) and replacing the $\nabla \times \mathbf{E}$ term with equation (2.4c) we can solve for $\partial_t \mathbf{B}$ and get the sought-after induction equation

$$\partial_t B = \nabla \times (\mathbf{v} \times \mathbf{B}) - \nabla \times (\eta \nabla \times \mathbf{B}). \tag{2.7}$$

Here $\eta = \frac{c}{4\pi\sigma}$ is the magnetic diffusivity which in ideal MHD is neglected so that using equation (B.5) the ideal induction equation yields

MHD: induction equation

$$\partial_t B + \nabla \cdot (\mathbf{v} \otimes \mathbf{B} - \mathbf{B} \otimes \mathbf{v}) = 0. \tag{2.8}$$

The **total energy density** of a magnetised fluid consists of the sum of the internal energy, the mechanical energy and the magnetic energy:

$$E_t = \epsilon + \frac{\rho v^2}{2} + \frac{B^2}{8\pi}.$$

As the only source of heat in ideal MHD is compression the equation of internal energy evolution is

$$\partial_\mathrm{t}\epsilon + \nabla\cdot(\epsilon\mathbf{v}) = -p\nabla\cdot\mathbf{v}. \tag{2.9}$$

For the mechanical and magnetic parts we calculate the dot product of the momentum equation (2.5) with $\mathbf{v}$ and combine the result with the dot product of the induction equation (2.8) with $\mathbf{B}$. Using the continuity equation (2.2) we find after some algebra

$$\partial_\mathrm{t}\left(\frac{\rho v^2}{2}+\frac{B^2}{8\pi}\right)+\nabla\cdot\left[\mathbf{v}\left(\frac{\rho v^2}{2}+p\right)+\frac{1}{4\pi}\mathbf{B}\times(\mathbf{v}\times\mathbf{B})\right]=p\nabla\cdot\mathbf{v} \tag{2.10}$$

With the use of equation (B.2) and summing up equations (2.9) and (2.10) we find the total energy balance for ideal MHD:

MHD: total energy equation

$$\partial_\mathrm{t}E+\nabla\cdot\left(\mathbf{v}(E+p_\mathrm{t})-\frac{1}{4\pi}(\mathbf{v}\cdot\mathbf{B})\mathbf{B}\right)=0. \tag{2.11}$$

In summary we can write down the **eight coupled, non-linear differential equations of ideal magnetohydrodynamics** as a vector equation of the form (compare to equation 2.1):

equations of ideal MHD

$$\partial_\mathrm{t}\begin{pmatrix}\rho\\ \rho\mathbf{v}\\ E\\ \mathbf{B}\end{pmatrix}+\nabla\cdot\begin{pmatrix}\rho\mathbf{v}\\ \rho\mathbf{v}\otimes\mathbf{v}+p_\mathrm{t}1-\frac{1}{4\pi}\mathbf{B}\otimes\mathbf{B}\\ \mathbf{v}(E_\mathrm{t}+p_\mathrm{t})-\frac{1}{4\pi}(\mathbf{v}\cdot\mathbf{B})\mathbf{B}\\ \mathbf{v}\otimes\mathbf{B}-\mathbf{B}\otimes\mathbf{v}\end{pmatrix}=0. \tag{2.12}$$

This system of equations has to be completed by an equation of state relating the internal energy ϵ to the pressure p. The conservation of $\operatorname{div}\mathbf{B}$ is not assured by these equations. A divergence-free magnetic field has to be assured separately.

2.3.2 The angular momentum balance

For later use we will point out the axisymmetric equation of angular momentum. It is derived from the general momentum equation (equation 2.12, see also Balbus (2004)),

$$\partial_t(R\rho v_\phi)+\nabla\cdot(\langle\rho\mathbf{v}_\mathrm{p}\rangle R^2\Omega)=-\nabla\cdot(\langle\rho\rangle R\mathbf{W}_\mathrm{p}). \tag{2.13}$$

The poloidal (r,θ) component of the stress tensor

$$\mathsf{W}=\langle\boldsymbol{\delta}\mathbf{v}\otimes\boldsymbol{\delta}\mathbf{v}-\frac{\mathbf{B}\otimes\mathbf{B}}{4\pi\rho}\rangle, \tag{2.14}$$

yields

$$\mathbf{W}_{\mathrm{p}} = \langle \delta v_\phi \boldsymbol{\delta}\mathbf{v}_{\mathrm{p}} - \frac{B_\phi \mathbf{B}_{\mathrm{p}}}{4\pi\rho} \rangle. \tag{2.15}$$

Angle brackets $\langle\rangle$ denote the volume average of a value; the index $_{\mathrm{p}}$ denotes the poloidal part of a vector or tensor.

2.3.3 Ideal relativistic MHD

The system of special relativistic MHD will consist of the same ingredients as the non relativistic set of equations: conservation laws for mass, energy and momentum and an induction equation describing the dynamics of the magnetic field. For a detailed derivation refer to Anile (1990). Please note that we chose to omit factors of c for better readability.

Due to special relativity we will apply the Minkowski metric which, with the use of the metric tensor $\eta_{\alpha\beta} = \mathrm{diag}\,(-1, +1, +1, +1)$ and the coordinates $x^\alpha = (t, x_1, x_2, x_3)$ is given by [2]

$$ds^2 = \eta_{\alpha\beta} dx^\alpha dx^\beta.$$

Indices are lowered and raised by applying the metric:

$$x_\alpha = \eta_{\alpha\beta} x^\beta. \tag{2.16}$$

Continuity of mass in covariant form is equivalent to the non relativistic case:

$$\partial_\alpha (\rho u^\alpha) = 0,$$

u_α being the relativistic four-velocity. We will derive the equations in the local rest ($\equiv$ comoving) frame.

Conservation of energy and momentum is usually combined to one tensor equation

$$\partial_\alpha T^{\alpha\beta} = 0.$$

The energy momentum tensor $T^{\alpha\beta}$ will consist of an hydrodynamic and an electro-magnetic part.

$$T^{\alpha\beta} = T^{\alpha\beta}_{\mathrm{HD}} + T^{\alpha\beta}_{\mathrm{EM}}.$$

For an ideal gas the hydrodynamic part can be rewritten directly from the Newtonian case (equation (2.3)):

$$T^{\alpha\beta}_{\mathrm{HD}} = (e + p) u^\alpha u^\beta + p \eta^{\alpha\beta},$$

where e and p are the total energy density and the pressure, both measured in the local rest frame.

[2] Einstein's sum notation is used: $a_\alpha b^\alpha \equiv \sum_\alpha a_\alpha b^\alpha$. Greek indices run from 0 to 3

For the electromagnetic part $T^{\alpha\beta}_{\mathrm{EM}}$ we will need the Maxwell equation which in a relativistic treatment can be summed up using the electromagnetic field tensor (*Faraday tensor*) (Jackson, 1975):

$$F^{\alpha\beta} = \begin{pmatrix} 0 & -E_1 & -E_2 & -E_3 \\ E_1 & 0 & -B_3 & B_2 \\ E_2 & B_3 & 0 & -B_1 \\ E_3 & -B_2 & B_1 & 0 \end{pmatrix},$$

where E and B are the electric and magnetic field strength, respectively. Now one can write the Maxwell equations as follows:

$$\begin{aligned} \partial_\alpha F^{\alpha\beta} &= 4\pi J^\beta \\ \partial_\alpha F_{\beta\gamma} + \partial_\gamma F_{\alpha\beta} + \partial_\beta F_{\gamma\alpha} &= 0, \end{aligned} \tag{2.17}$$

where $J^\alpha = (c\rho, \mathbf{j})$ is the charge current four-vector.

In the ideal case the electric conductivity σ is infinite and from Ohm's law $J^\alpha = \rho u^\alpha + \sigma F^{\alpha\beta} u_\beta$ we get the condition $F^{\alpha\beta} u_\beta = 0$. Now we can express the electric field E with the magnetic field B (similarly to $\mathbf{E} = -\mathbf{v} \times \mathbf{B}$ in the Newtonian limit) by

$$E^\alpha = \epsilon^{\alpha\beta\gamma} u_\beta B_\gamma$$

and a simpler expression for the Faraday tensor can be written as:

$$F^{\alpha\beta} = \epsilon^{\alpha\beta\gamma\delta} B_\gamma u_\delta, \tag{2.18}$$

where ϵ is the Levi-Civita symbol.

Finally, assuming locally vanishing and minimal entropy flux (Dixon, 1978) one identifies the electromagnetic component as:

$$T^{\alpha\beta}_{\mathrm{EM}} = \frac{1}{4\pi}(-B^\alpha B^\beta + \frac{1}{2} B_\gamma B^\gamma \eta^{\alpha\beta} + B_\gamma B^\gamma u^\alpha u^\beta)$$

Thus the energy momentum tensor of relativistic magnetohydrodynamics can be written as

$$T^{\alpha\beta} = (e + p + \frac{1}{4\pi} B^2) u^\alpha u^\beta + (p + \frac{1}{8\pi} B^2) \eta^{\alpha\beta} - \frac{1}{4\pi} B^\alpha B^\beta.$$

To find the **induction equation** will use equation (2.17) and extract the magnetic part of the field tensor using (2.18) and get

$$\partial_\alpha (u^\alpha B^\beta - B^\alpha u^\beta) = 0.$$

In summary, the equations of relativistic magnetohydrodynamics are

equations of ideal relativistic MHD

$$\partial_\alpha (\rho u^\alpha) = 0 \tag{2.19}$$

$$\partial_\alpha \left((e + p + \frac{1}{4\pi} B^2) u^\alpha u^\beta + (p + \frac{1}{8\pi} B^2) g^{\alpha\beta} - \frac{1}{4\pi} B^\alpha B^\beta \right) = 0 \tag{2.20}$$

$$\partial_\alpha (u^\alpha B^\beta - B^\alpha u^\beta) = 0. \tag{2.21}$$

Applying the Lorentz transformation and renormalising the magnetic field with $\frac{1}{\sqrt{4\pi}}B \to B$ we can rewrite these equations in the laboratory frame and get the equations actually implemented in PLUTO:

equations of ideal relativistic MHD in the laboratory frame

$$\partial_t \begin{pmatrix} D \\ \mathbf{m} \\ e \\ \mathbf{B} \end{pmatrix} + \nabla \cdot \begin{pmatrix} D\mathbf{v} \\ w_t \gamma^2 \mathbf{v} \otimes \mathbf{v} - \mathbf{b} \otimes \mathbf{b} + p_{tot} 1 \\ \mathbf{m} \\ \mathbf{v} \otimes \mathbf{B} - \mathbf{B} \otimes \mathbf{v} \end{pmatrix} = 0. \tag{2.22}$$

with $\gamma = (1 - v^2)^{-1/2}$ being the Lorentz factor and using the new variables D (density in the laboratory frame), $\mathbf{m}$ (momentum density) and e (total energy including rest mass):

$$\begin{aligned} D &= \gamma\rho \\ \mathbf{m} &= w_t \gamma^2 \mathbf{v} - b^0 \mathbf{b} \\ e &= w_t \gamma^2 - b^0 b^0 - p_{tot} \end{aligned}$$

b^0, $\mathbf{b}$, w_t and p_t have the following meaning:

$$\begin{aligned} b^0 &= \gamma \mathbf{v} \cdot \mathbf{B} \\ \mathbf{b} &= {}^{\mathbf{B}}/_{\gamma} + \gamma(\mathbf{v} \cdot \mathbf{B})\mathbf{v} \\ w_t &= \rho h + {}^{\mathbf{B}^2}/_{\gamma^2} + (\mathbf{v} \cdot \mathbf{B})^2 \\ p_{tot} &= p + \frac{{}^{\mathbf{B}^2}/_{\gamma^2} + (\mathbf{v} \cdot \mathbf{B})^2}{2}. \end{aligned}$$

h is the specific enthalpy defined by

$$h = 1 + \mathcal{E} + \frac{p}{\rho}, \quad \text{(specific internal energy } \mathcal{E} = \frac{\epsilon}{\rho}) \tag{2.23}$$

which has to be determined by a closure relation.

2.3.4 Source and sink terms in MHD

The system of ideal MHD equations is homogeneous which in a physical context means that the dynamic variables are conserved. As pointed out in section 2.3 the choice of a curvilinear coordinate system or physical processes make it necessary to expand the equations by source terms. These are terms that cannot be written as the flux of a physical quantity and therefore cannot appear on the left hand side of eq. (2.1).

In the following we will discuss terms which will be used in our simulations. Other common sources and sinks of energy, momentum and mass such as viscosity, resistivity, and chemical or nuclear reactions will not be discussed as they are not taken into account in the presented simulations.

Gravity

In principal in an accreting system there are two sources of gravity: the central object and the disc itself. The latter is referred as *self-gravity*. Due to the low mass of the disc compared to the central object, in the case studied here, we neglect self-gravity. Denser discs exist e.g. around protostars were (self-)gravitational instabilities are believed to lead to the formation of planets.

The centre of accretion in an X-ray-binary is a neutron star or a black hole, i.e. a relativistic object. Therefore, to treat this case correctly we would have to apply a general relativistic magnetohydrodynamics (GRMHD) code. These codes exist since a few years. But still the treatment of non ideal terms (e.g. radiation) is under development by the international community, so for the sake of versatility we chose to use a special relativistic code and emulate the gravitational effects of the central object by the use of a so called *pseudo potential*.

A pseudo potential defines the gravitational potential on a flat time space. Thus it can be used in conjunction with a Newtonian or special relativistic numerical scheme. The disadvantage is that it will not reproduce every feature of the correct relativistic potential. Different pseudo potentials have been proposed in the literature. The one used in this work is presented in the following.

Pseudo Schwarzschild potential by Paczynsky & Wiita In order to reproduce the relativistic properties of the inner disc, Paczynsky and Wiita (1980) proposed a pseudo Newtonian potential which is able to reproduce the radii of a black hole's marginally stable orbit at $r_{\mathrm{ms}} = 6\,\mathrm{R_g}$ and of the marginally bound orbit at $r_{\mathrm{mb}} = 4\,\mathrm{R_g}$. It follows a simple form:

$$\Phi_{\mathrm{PW}} = -\frac{1}{r-2} \tag{2.24}$$

It is not capable of emulating the effects of black hole spin which become more and more dominant at radii of $r < 10\,R_{\mathrm{g}}$.

Radiative cooling

It turns out that of all possible cooling mechanisms, non thermal synchrotron radiation is the most officiants one when magnetic fields are present and matter is hot. so for the application of optically thin accretion tori in the vicinity of a black hole, it is a good approach to implement a sink term emulation synchrotron losses in the energy balance of ideal MHD.

In the following we will derive the needed equation of energy loss rate due to synchrotron radiation.

Synchrotron cooling For an electron in a uniform magnetic field the emitted power integrated over all frequencies ν becomes (Shu, 1991)

$$P_{\mathrm{em}} = 2(\gamma^2 - 1)c\sigma_{\mathrm{T}} P_{\mathrm{mag}} \sin^2 \alpha,$$

where γ is the Lorentz-factor, $\sigma_{\mathrm{T}} = 8\pi r_{\mathrm{e}}^2/3$ is the Thomson cross section (with $r_{\mathrm{e}} = e^2/m_{\mathrm{e}}c^2$ being the classical electron radius) and $P_{\mathrm{mag}} = B^2/8\pi$ is the magnetic pressure or energy density. Assuming isotropy and averaging over all angles the emission of one particle is given by

$$\langle P_{\mathrm{em}} \rangle = \frac{4}{3}(\gamma^2 - 1)c\sigma_{\mathrm{T}} P_{\mathrm{mag}}.$$

This may for a single electron differ from the total received power $\langle P \rangle$ due to relativistic motion of the electron toward or away from the observer. But the average power of an *isotropic* collection of electrons must equal the average received power, thus $\langle P \rangle = \langle P_{\mathrm{em}} \rangle$.

The luminosity results from integration over all γ and the source volume as

$$\begin{aligned} L &= \int_V dV\, \rho j, \\ &= \int_V dV \int_1^\infty d\gamma\, \langle P(\gamma) \rangle n_{\mathrm{e}}(\gamma), \end{aligned} \tag{2.25}$$

where ρj is the emission coefficient, defined as the energy emitted spontaneously per time, angle and volume[3], given by

$$\rho j_\nu = \int_1^\infty d\gamma\, \langle P_\nu(\gamma) \rangle n_{\mathrm{e}}(\gamma). \tag{2.26}$$

$n_{\mathrm{e}}(\gamma)$ represents the electron number density, which is in a first approach approximated by a gauge value n_0 weighted by the relativistic Maxwell distribution (Wardziński and Zdziarski, 2000):

$$f(\gamma) = \frac{\gamma(\gamma^2 - 1)^{1/2}}{\Theta K_2(1/\Theta)} e^{-\gamma/\Theta}, \tag{2.27}$$

with

$$\Theta = \frac{kT}{m_{\mathrm{e}}c^2}$$

being the dimensionless plasma temperature (m_{e} is the electron mass) and K_2 the second modified Bessel function. Since electrons are fast ($\gamma \gg 1$) and hot ($\Theta \gg 1$) equation (2.27) can be approximated as

$$f(\gamma) = \frac{\gamma^2}{2\Theta^3} e^{-\gamma/\Theta},$$

[3] In *Radiative Processes in Astrophysics* (Rybicki and Lightman, 1979) this quantity is denoted as j. The *emissivity* here written as j_ν is there indicated as ϵ_ν.

using (Abramowitz and Stegun, 1972)

$$K_2(1/\Theta) \approx 2\Theta^2 \quad for \quad 1/\Theta \to 0$$

The Luminosity, i.e. the radiated power from a volume V, averaged over all electrons and integrated over all frequencies is then found to be

$$\begin{aligned} L &= \int_V dV \int_1^\infty d\gamma \, \langle P(\gamma) \rangle n_0 f(\gamma) \\ &= \frac{2}{3} c \sigma_\mathrm{T} n_0 P_\mathrm{mag} \int_V dV \int_1^\infty d\gamma \, \frac{\gamma^4}{\Theta^3} e^{-\gamma/\Theta} \\ &= \frac{2}{3} c \sigma_\mathrm{T} \int_V dV \Big[n_0 P_\mathrm{mag} \cdot \\ &\qquad \Theta^{-2} e^{-1/\Theta} (24\Theta^4 + 24\Theta^3 + 12\Theta^2 + 4\Theta + 1) \Big]. \end{aligned} \tag{2.28}$$

For volumes V sufficiently small to be treated as homogeneous concerning n_0, P_mag and Θ and (again) $\Theta > 1$ equation (2.28) simplifies to

$$L = 16 c \sigma_\mathrm{T} V n_0 P_\mathrm{mag} \Theta^2 e^{-1/\Theta} \tag{2.29}$$

The approximation of the Θ-term suits a relative error of less than 0.021 for $\Theta = 0.65$ (i.e. $T = 3.85 \cdot 10^9 \mathrm{K}$) and decreases rapidly with larger Θ.

As the electron number density calculates as follows

$$n_0 = \frac{\rho}{m_\mathrm{p}} \tag{2.30}$$

equation (2.29) becomes

$$L = 16 c \sigma_\mathrm{T} V \frac{\rho}{m_\mathrm{p}} P_\mathrm{mag} \Theta^2 e^{-1/\Theta} \tag{2.31}$$

Consequently the rate at which internal energy density in a simulation diminishes is given by

$$\partial_\mathrm{t} S_{synchrotron} = 16 c \sigma_\mathrm{T} \frac{\rho}{m_\mathrm{p}} P_\mathrm{mag} \Theta^2 e^{-1/\Theta}. \tag{2.32}$$

2.4 Magnetorotational instability

In section 1.2 we gave an intuitive introduction to the basic mechanisms behind MRI. In this section we will describe this instability on an analytical base.

First we will treat the ideal case of vanishing resistivity and no interaction with radiation. The derivation of the ideal dispersion relation is loosely based on the review by Balbus and Hawley (1998). In the 2$^{\mathrm{nd}}$ section we will summarise how radiation and finite conductivity alter the ideal results.

2.4.1 MRI in ideal fluids

To derive the dispersion relation of MHD in a rotating medium we will use cylindrical coordinates. These are more suitable than spherical coordinates (which will be used for the simulations) because they contain a uniform, non curved dimension (z) in which we will apply the perturbation needed for the linear analysis. Cartesian coordinates are not the optamal choice either because we are seeking dependencies on the rotation which is a movement in the coordinate ϕ.

We consider a weakly magnetised medium all the variables of which are perturbed locally by linear disturbances of the form $e^{i(\mathbf{k}\cdot\mathbf{r}-\omega t)}$. $\mathbf{k}$ is the wave vector of the perturbation, $\mathbf{r}$ denotes the position of the perturbed fluid element, ω is the angular frequency of the perturbation and t is the time. For the sake of simplicity we assume the radial magnetic field to vanish. A radial component would lead to a time dependence of B_ϕ which would have little effect on a weak-field axisymmetric instability. Also we restrict the perturbations to $\mathbf{k} = k\mathbf{e}_\mathrm{z}$.

The perturbed equations of ideal non relativistic MHD can be written in Matrix form:

$$0 = \begin{pmatrix} -\frac{\omega}{\rho} & 0 & 0 & 0 & k & 0 & 0 & 0 \\ 0 & 0 & i\omega & 2\Omega & 0 & \frac{ikB_\mathrm{z}}{4\pi\rho} & 0 & 0 \\ 0 & 0 & \frac{\kappa^2}{2\Omega} & 0 & -i\omega & 0 & -\frac{ikB_\mathrm{z}}{4\pi\rho} & 0 \\ 0 & \frac{k}{\rho} & 0 & 0 & -\omega & 0 & \frac{kB_\phi}{4\pi\rho} & 0 \\ 0 & 0 & kB_\mathrm{z} & 0 & 0 & \omega & 0 & 0 \\ 0 & 0 & 0 & ikB_\mathrm{z} & -ikB_\phi & \frac{\mathrm{d}\Omega}{\mathrm{d}\ln R} & i\omega & 0 \\ -\gamma\rho & \frac{1}{P} & 0 & 0 & 0 & 0 & 0 & 0 \\ 0 & 0 & 0 & 0 & 0 & 0 & 0 & 1 \end{pmatrix} \cdot \begin{pmatrix} \delta\rho \\ \delta P \\ \delta v_\mathrm{r} \\ \delta v_\phi \\ \delta v_\mathrm{z} \\ \delta B_\mathrm{R} \\ \delta B_\phi \\ \delta B_\mathrm{z} \end{pmatrix} \equiv \mathsf{A}\cdot\delta\mathbf{U} \tag{2.33}$$

The perturbation amplitudes are denoted by a δ, $\mathbf{U}$ is the state vector of the fluid and κ is the epicycle frequency. Non linear perturbations, i.e. terms quadratic in one perturbed variable ($\propto (\delta\mathbf{U})^2$) are neglected.

The dispersion relation is obtained by computing the determinant of A and setting it to 0:

$$\det \mathsf{A} = 0$$

With the use of the speed of sound in an ideal gas

$$c_\mathrm{s}^2 = \gamma\frac{p}{\rho},$$

the definition of the Alfvén speed in the z and ϕ direction

$$v_{\mathrm{A}z/\phi}^2 = \frac{B_{z/\phi}^2}{4\pi\rho},$$

one obtains after of some algebra the dispersion relation of MHD in rotating media:

MRI: dispersion relation of MHD in rotating media

$$\begin{aligned}\omega^6 &+ \omega^4 \cdot \left(-2k^2 v_{\mathrm{A}z}^2 - k^2 v_{\mathrm{A}\phi}^2 - \kappa^2 - k^2 c_{\mathrm{s}}^2 \right) \\ &+ \omega^2 \cdot \left(2k^4 c_{\mathrm{s}}^2 v_{\mathrm{A}z}^2 + k^2 c_{\mathrm{s}}^2 \kappa^2 - 2k^2 v_{\mathrm{A}z}^2 \Omega \frac{\mathrm{d}\Omega}{\mathrm{d}\ln R} \right. \\ &\qquad \left. + k^4 v_{\mathrm{A}z}^4 + k^2 v_{\mathrm{A}\phi}^2 \kappa^2 + k^4 v_{\mathrm{A}\phi}^2 v_{\mathrm{A}z}^2 \right) \\ &+ \left(2k^4 c_{\mathrm{s}}^2 v_{\mathrm{A}z}^2 \Omega \frac{\mathrm{d}\Omega}{\mathrm{d}\ln R} - k^6 c_{\mathrm{s}}^2 v_{\mathrm{A}z}^4 \right) \quad = 0.\end{aligned} \tag{2.34}$$

Examining the case of Keplerian rotation

$$\Omega \propto R^{3/2} \quad , \quad \frac{\mathrm{d}\Omega}{\mathrm{d}\ln R} = -\frac{3}{2}\Omega = \frac{1}{2\Omega}\frac{\mathrm{d}\Omega^2}{\mathrm{d}\ln R},$$

the epicycle frequency becomes

$$\kappa = \Omega$$

and equation (2.34) yields

$$\begin{aligned}\omega^6 &+ \omega^4 \cdot (-2k^2 v_{\mathrm{A}z}^2 - k^2 v_{\mathrm{A}\phi}^2 - \Omega^2 - k^2 c_{\mathrm{s}}^2) \\ &+ \omega^2 \cdot (2k^4 c_{\mathrm{s}}^2 v_{\mathrm{A}z}^2 + k^2 c_{\mathrm{s}}^2 \Omega^2 - 3k^2 v_{\mathrm{A}z}^2 \Omega^2 \\ &\qquad + k^4 v_{\mathrm{A}z}^4 + k^2 v_{\mathrm{A}\phi}^2 \Omega^2 + k^4 v_{\mathrm{A}\phi}^2 v_{\mathrm{A}z}^2) \\ &+ (3k^4 c_{\mathrm{s}}^2 v_{\mathrm{A}z}^2 \Omega^2 - k^6 c_{\mathrm{s}}^2 v_{\mathrm{A}z}^4) \quad = 0.\end{aligned} \tag{2.35}$$

In the non rotating case ($\Omega = 0$) equation (2.34) simplifies to

$$\begin{aligned}\omega^6 &+ \omega^4 \cdot (-2k^2 v_{\mathrm{A}z}^2 - k^2 v_{\mathrm{A}\phi}^2 - k^2 c_{\mathrm{s}}^2) \\ &+ \omega^2 \cdot (2k^4 c_{\mathrm{s}}^2 v_{\mathrm{A}z}^2 + k^4 v_{\mathrm{A}z}^4 + k^4 v_{\mathrm{A}\phi}^2 v_{\mathrm{A}z}^2) \\ &- k^6 c_{\mathrm{s}}^2 v_{\mathrm{A}z}^4 \quad = 0.\end{aligned} \tag{2.36}$$

Equation (2.36) is the general dispersion relation for MHD in a non moving medium. Naming θ the angle between $\mathbf{B}$ and $\mathbf{k}$ and assuming either $c_{\mathrm{s}} \ll v_{\mathrm{A}}$, $v_{\mathrm{A}} \ll c_{\mathrm{s}}$ or $\cos\theta \approx 0$, we find three solutions to this equation, representing the three wave modes present in magnetised fluids:

$$\omega_{\mathrm{A}}^2 = k^2 v_{\mathrm{A}}^2 \cos^2\theta \qquad \text{Alfvén mode,} \tag{2.37}$$

$$\omega_{+}^2 = k^2 (v_{\mathrm{A}}^2 + c_{\mathrm{s}}^2) \qquad \text{fast (magnetosonic) mode,} \tag{2.38}$$

$$\omega_{-}^2 = \frac{k^2 v_{\mathrm{A}}^2 c_{\mathrm{s}}^2 \cos^2\theta}{v_{\mathrm{A}}^2 + c_{\mathrm{s}}^2} \qquad \text{slow mode.} \tag{2.39}$$

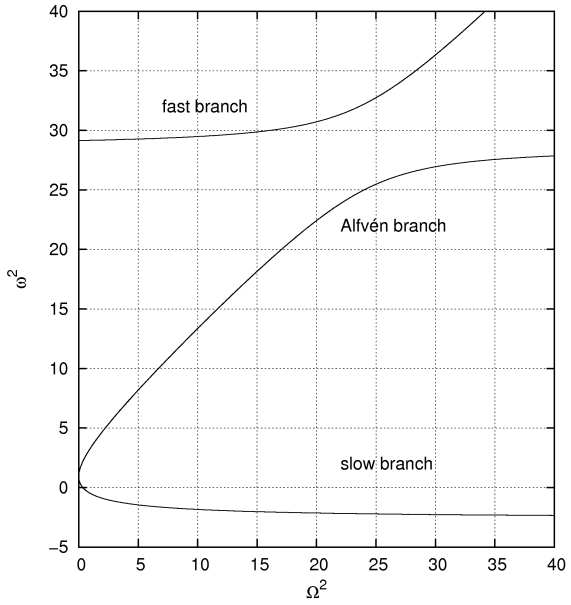

***Figure 2.1** – Branches of the MHD modes.*

It can be easily shown that $\omega_+^2 > \omega_\mathrm{A}^2 > \omega_-^2 > 0$ for the non rotating case. Thus there are no unstable modes which require $\omega^2 < 0$. Not so in the rotating case. To show the effects of Keplerian rotation, we will fix the values of $kv_{\mathrm{A}z} = 1$, $kv_{\mathrm{A}\phi} = 2$ and $ka = 5$ (i.e. we scale all quantities to units of $kv_{\mathrm{A}z}$) and plot the angular frequency of the perturbation ω^2 versus the angular frequency of the fluid Ω^2 (figure 2.1). The slow branch becomes unstable for $\Omega^2 > \frac{1}{3}\, kv_{\mathrm{A}z}$.

To find the fastest growing wave we will use the Boussinesq approximation which consists in neglecting the inertia variations of a fluid, i.e. assuming a uniform density except in terms which describe the effect of gravity. Because sound is transmitted via inertia variations, formally the sound speed reaches infinity (i.e. $c_\mathrm{s} \to \infty$). In this case we can divide equation (2.34) by c_s^2 and neglect terms proportional to $1/c_\mathrm{s}^2$:

$$\omega^4 - \omega^2 \cdot (\kappa^2 + 2k^2 v_{\mathrm{A}z}^2) + k^2 v_{\mathrm{A}z}^2 \left(k^2 v_{\mathrm{A}z}^2 + 2\Omega \frac{\mathrm{d}\Omega}{\mathrm{d}\ln R} \right) = 0 \tag{2.40}$$

Equation (2.40) can be interpreted as a wave equation for the perturbations of the fluid and thus will be stable only if

$$k^2 v_{\mathrm{A}z}^2 > -2\Omega \frac{\mathrm{d}\Omega}{\mathrm{d}\ln R}. \tag{2.41}$$

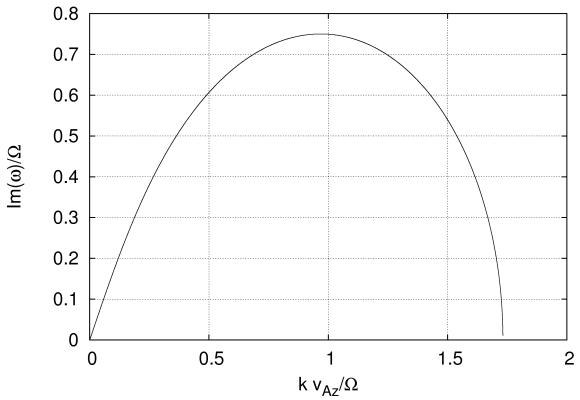

Figure 2.2 – Growth rate of the MRI.

This means that for a sufficiently small k the medium is always unstable unless

$$\frac{\mathrm{d}\Omega}{\mathrm{d}\ln R} > 0 \tag{2.42}$$

which is virtually never true for astrophysical plasmas.

Equation (2.40) also is a quadratic in ω^2 (figure 2.2) which yields a maximum unstable growth rate

$$\omega_{\max} = \frac{1}{2}\left|\frac{\mathrm{d}\Omega}{\mathrm{d}\ln R}\right|$$

and a maximum unstable wave number

$$k^2_{\max} = -\frac{1}{v^2_{\mathrm{A}z}}\left(\frac{1}{4} + \frac{\kappa^2}{16\Omega^2}\right)\frac{\mathrm{d}\Omega^2}{\mathrm{d}\ln R},$$

which for the case of Keplerian rotation result in

MRI: fastest growing modes

$$\omega_{\max} = \frac{3}{4}\Omega \tag{2.43}$$

$$k_{\max} = \frac{\sqrt{15}}{4\,v^2_{\mathrm{A}z}}\Omega. \tag{2.44}$$

Equation (2.43) indicates that the typical growth rate, i.e. the time in which a perturbation growth by a factor of e, is of the order of an orbital period. This makes MRI an extremely fast operating instability.

Equation (2.44) gives upper and lower limits for the magnetic field to allow the MRI to act on the fluid. For a magnetic field that is too strong, $k_{\max}$ is too small, which means that the fastest growing wave mode will not fit into

the disc. Thus the height of the disc gives an upper limit for the magnetic field strength.

One the other hand when the magnetic field is too weak, the unstable wave modes will have a wavelength of the microscopic scale or in the case of numerical simulation of the size of a grid cell. In both cases diffusion (physical or numerical, respectively) will inhibit the growth of perturbations. This results in a lower boundary to the magnetic field strength.

2.4.2 MRI in the radiative case

Starting from the ideal linear theory of the MRI one can extend the analysis to more general cases. For the presented work the most interesting effect not covered by ideal MHD is radiation. A well studied approximation is the *flux limited diffusion* approach. Radiation is treated as diffusing photons. To assure the diffusion velocity to be less than the speed of light, a *flux limiter* λ is introduced into the diffusion equation:

$$F_{\mathrm{phot}} \propto -\left(\frac{c\lambda}{\chi}\right) \nabla e_{\mathrm{phot}},$$

where F_{phot} is the photon flux, χ the total extinction coefficient and e_{phot} is the energy density of the radiative field.

Adding additional equations for the photon energy and flux to the MHD equations enables the treatment of both optically thick and thin media. The disadvantages of this approach are that (1) the regime of intermediate optical thickness must be modelled with the use of further assumptions, (2) radiation is assumed to be isotropic and always diffusion from hot to cold regions, which is not the case in optically thin regions where non local irradiation is present and (3) spectral information is neglected.

In spite of the deficiencies one can redo the linear analysis of the MRI with radiation. The result is that the interaction of an optically thick gas with radiation is twofold (Flaig *et al.*, 2009): on the one hand, vertical MRI modes (which are the fastest growing ones) are damped while on the other hand non vertical modes are enhanced. As mentioned in section 1.4, more investigation and global simulations are needed to explore the interaction of the MRI and the effects of radiation with respect to the global disc dynamics.

2.5 Numerical MHD

As we showed in section 2.3 the equations of MHD can be written as a set of coupled conservation laws of the form

$$\partial_{\mathrm{t}} U + \nabla F(U) = S(U).$$

where $U = U(\mathbf{x}, t)$ is the conserved variable and a function of space and time, $F(U)$ the respective flux function and $S(U)$ is the sum of source terms. In order to obtain information about future states, the equations have to be evolved in time; a closed analytical solution of the equations of MHD does not exist due to their non linear character. One way to evolve the system of equations in time relies on discretising it in space and time[4]. This is done by evaluating the variables on a spatial grid and at discrete time levels.

The variables are defined at the cell centres and the flux function describes the flux across the cell faces. At each time step the fluxes and sources have to be calculated and the physical variable is updated. This corresponds to solving the dynamical behaviour of a discontinuity in the variables, which is commonly referred to as the 'Riemann problem' (Toro, 2008). By summing up the fluxes at all interfaces of a cell, this method (called *Riemann solver* or *finite volume* method) assures the correct evolution of the variables as required by the conservation laws. Another important property of Riemann solvers for our purposes is the stability at shocks (large gradients) which is not guaranteed by *finite difference* methods which formally are a subset of finite volume methods of first order (Toro, 2009). In finite volume methods additional techniques (such as limiters) assure the capability of resolving shocks correctly. Therefore these methods are also called *shock capturing* methods.

The change of the physical values in every cell depends on the characteristic wave modes (hereafter *characteristics*) travelling in the fluid, the motion of the fluid and the discontinuity itself. In MHD the characteristics are the fast mode, the Alfvén mode, the slow mode, the hydrodynamic sound speed and the displacement speed of the discontinuity.

Depending on which characteristics are taken into account to evaluate the flux function and on the method to compute the derivatives, a number of Riemann solvers have been proposed in the literature and implemented in numerical codes. Since we are interested in the MRI, we need a solver which evaluates the slow mode of MHD (see section 2.4). Mignone *et al.* (2009) developed a solver named *HLLD*[5] with these properties and implemented it in their code *PLUTO* (Mignone *et al.*, 2007). We use this freely available

[4] Another technique, the *spectral* method discretises the equations in the Fourier space, i.e. in frequencies and wave numbers.

[5] HLLD = Harten-Lax-van Leer solver with discontinuity treatment

code for the option of applying this HLLD solver, its versatility and its user-friendliness.

2.5.1 The code: PLUTO

PLUTO is a versatile code by Mignone *et al.* (2007) which provides several modules to solve the equations of Newtonian and relativistic HD and MHD with different Riemann solvers one can choose of. It is possible to initialise uniform and non uniform grids in Cartesian, cylindrical and spherical coordinates.

There is a number of codes available solving the equations of MHD on a grid. In principle one can perform the simulations presented in this work with any of these codes. However there are differences which require the evaluation of the advantages and disadvantages of every code to chose the one which will be best suited for the purpose. In the following we will give a short overview over some other available codes.

ATHENA (Stone *et al.*, 2008), is a code very similar to PLUTO. It includes high-order spatial reconstruction, the flux constraint transport (FCT, see below) technique to assure a divergence-free magnetic field and MHD solver in 3 dimensions. It does not include higher-order time stepping algorithms and is not as versatile concerning the details of the numerical implementation as PLUTO. We tested different time stepping methods with PLUTO and found that a 2^{nd} order scheme has a significant higher accuracy then the first order (Euler) method implemented in ATHENA.

FLASH (Dubey *et al.*, 2009), is probably one of the most used codes in astrophysical simulations. It features different solvers and physics modules and is highly customisable by a modular architecture. However it is not possible to simulate MHD on a spherical grid which is needed for our simulations.

ZEUS (Hayes *et al.*, 2006) is a widely-used code whose first implementations date back to 1980. It uses a finite difference scheme which, as mentioned before, do not solve the equations fluid dynamics correctly in the vicinity of shocks. Also ZEUS does not simulate the linear phase of the MRI as accurate as PLUTO with the HLLD solver (Flock, 2008).

Finally, PLUTO is the only freely available code which implements the equations of MHD in a special relativistic formulation. As we expect to find regions of small density and strong magnetisation, i.e. a Alfvén speed close to the speed of light, the use of a relativistic code is crucial for simulating black hole accretion flows. In a Newtonian code the Alfvén speed will exceed the speed of light which causes the simulation to eventually stall due to

the small time step needed to resolve the propagation of the Alfvén waves (Brinkmann, 2004).

2.6 Numerical set-up

In this section we will describe the basic numerical set-up of the simulations. As illustrated before, PLUTO enables the user chose from a wide variety of solvers, time stepping algorithms, spatial reconstruction schemes etc. The algorithmic set-up is given as a list with references (section 2.6.1) since a detailed description is beyond the scope of this work. When no references are given, details can be found in the standard literature on numerical fluid dynamics such as the books by Toro (2009) or LeVeque (2002).

Detailed information is given about the set-up of the grid (section 2.6.2), the boundary conditions (section 2.6.3)and the treatment of magnetic monopoles (section 2.6.4).

2.6.1 Algorithmic setup

Solver: As a solver we used HLLD for the relativistic MHD physics module (Mignone *et al.*, 2009). This solver takes into account the characteristic speeds of the fast magnetosonic wave, the discontinuity and the slow mode of MHD. The latter is important for the simulation of the MRI as it is the slow mode that is unstable (see section 2.4).

Spatial reconstruction: The reconstruction of the cell centred variables at the cell faces was done in a linear (2^{nd} order) manner.

Time stepping: Also time stepping was set to be of 2^{nd} order (*Runge-Kutta integrator*).

Equation of state: As the closure relation for the system of MHD equations we used Taub's equation of state(Mignone *et al.*, 2009)

$$(h - 4\frac{p}{\rho})(h - 1\frac{p}{\rho}) = 0,$$

where h is the specific enthalpy defined in equation 2.23.

Electromotive forces: For the reconstruction of the electromotive forces at the cell faces we chose a a two dimensional Riemann solver based on a four-state HLL flux function as described by Del Zanna *et al.* (2003). A reconstruction scheme is needed due to the use of the FCT method (see below).

2.6.2 Grid

The simulations were carried out on a spherical uniform grid consisting of $N_\mathrm{r} \times N_\theta \times N_\phi = 768 \times 256 \times 1$ cells, spanning from $r_\mathrm{min} = 5\,\mathrm{R_g}$ to $r_\mathrm{max} = 150\,\mathrm{R_g}$, $\theta_\mathrm{min} = 0.05$ to $\theta_\mathrm{max} = \pi - 0.05$ and $\phi_\mathrm{min} = 0$ to $\phi_\mathrm{max} = 2\pi$. The grid spacings were chosen such that the grid cells have equal extension in r and θ at a radius of $\approx 15\,\mathrm{R_g}$.

The model case was simulated with the same grid resolution (cells/physical length) but with an radially extended domain reaching out to $r_\mathrm{max} = 800\,\mathrm{R_g}$. In the 3D case we initialised the grid with $256 \times 84 \times 42$ and let the azimuthal dimension of the simulation range from $\phi_\mathrm{min} = 0$ to $\phi_\mathrm{max} = \pi/2$.

2.6.3 Boundary conditions

Boundary conditions in the azimuthal direction are *periodic*; in the poloidal direction we applied *axisymmetric* boundaries which means that at the boundary, vector components parallel to the axis and scalar values are set to be equal to the value next to the boundary; other vector components are set to 0. The outer radial boundary consists of two zones. A layer of 35 logarithmically scaled cells ranging from the outer boundary r_max to $r_\mathrm{max} + 35\,\mathrm{R_g}$ surrounds the computational domain. The equations of MHD are evaluated in the same manner as inside the domain. Actually it is implemented as a part of the domain but will not be taken into account for analysis. Its only purpose is to omit reflection of waves and numerical problems at the outer boundary. The 2^nd zone is the actual numerical boundary which enables matter to flow in and out freely (commonly called *zero-gradient*, within PLUTO *outflow*), but the density is set to the atmospheric value for inflow. For the inner boundary we implemented a real *outflow* condition assuring the matter to have a radial velocity $v_\mathrm{r} \leq 0$ at the inner face of the boundary cells.

2.6.4 Avoiding magnetic monopoles

In a numerical implementation of the equations of MHD, the magnetic field can suffer from an increasing divergence. Additional techniques are required to prevent $\mathrm{div}\,\mathbf{B}$ from growing. PLUTO includes three different approaches to this task, namely (1) the *constraint transport* Balsara and Spicer (1999) (described below), (2) the *eight-wave* method by Powell *et al.* (1999) in which $\mathrm{div}\,\mathbf{B}$ is treated as a conserved 8^th free variable of the system and (3) the *divergence cleaning* method by Dedner *et al.* (2002) in which numerical divergence of the magnetic field is advected to the boundaries and damped at the same time.

In our set-up the conservation of $\mathrm{div}\ \mathbf{B}$ is assured by use of flux constrained transport (FCT) algorithm developed by Balsara and Spicer (1999). In this

scheme, the magnetic field components are define on the cell faces instead of the cell centres. This minimises the error when calculating the magnetic flux (which is computed on the faces).

An initially divergence-free magnetic field distribution is set up by providing a vector potential $\mathbf{A}$ and then calculating $\mathbf{B} = \nabla \times \mathbf{A}$.

2.6.5 Physical scaling

All simulations except for case `QUAD_SYNC` can be scaled to any black hole mass and initial torus density because there are no microscopic physics in the equations of ideal MHD.

The code units for length and time are given by:

$$R_\mathrm{g} = \frac{MG}{c^2} \approx 1.48 \cdot 10^5 \left(\frac{M}{M_\odot}\right) \mathrm{cm}$$
$$lct = \frac{MG}{c^3} \approx 4.92 \cdot 10^{-6} \left(\frac{M}{M_\odot}\right) \mathrm{s}.$$

For the radiative case the absolute value of density is of importance. In that case and for application of our results to real objects we set the code unit for density to

$$\rho_0 = 10^{-7}\,\mathrm{g/cm^3}.$$

All other quantities can be calculated by these three units, e.g. the characteristic velocity is given by $R_\mathrm{g}/lct = c$.

For better comparability to the two known classes of black hole accretors we will provide the characteristic length and time scales for a typical AGN and microquasar.

AGN ($M = 10^9\,\mathrm{M}_\odot$):

$$R_\mathrm{g} \approx 1.48 \cdot 10^{14}\,\mathrm{cm} \approx 9.9\,\mathrm{AU}$$
$$lct \approx 4.92 \cdot 10^3\,\mathrm{s} \approx 1\,\mathrm{h}\,22\,\mathrm{min}.$$

Microquasar ($M = 10\,\mathrm{M}_\odot$):

$$R_\mathrm{g} \approx 1.48 \cdot 10^6\,\mathrm{cm} \approx 14.8\,\mathrm{km}$$
$$lct \approx 4.92 \cdot 10^{-5}\,\mathrm{s} \approx 49.2\,\mu\mathrm{s}.$$

I'm slow to finish but I'm quick to start.

— Anthony Kiedis

3 The model case

The model case `QUAD` described in this chapter represents the basis of the different tests presented in the following. It consists of a hydrodynamically stable torus in the effective potential well given by the Keplerian angular momentum and gravitational forces. The magnetic field is purely poloidal and consists of to vertically stacked loops forming a quadrupole.

This configuration or variations of it are widely used to set-up advection dominated accretion discs. As the simulation progresses it shows all of the features of an accretion flow we are interested in: A turbulent torus body, a structured accretion flow that forms channels and a fast outflow.

We let this simulation run for longer time than the cases presented in chapter 4 to test the long term behaviour of the accretion flow. The domain was extended radially to obtain information about the dynamics of ejected material at larger radii. Also a hydrodynamic simulation was performed to test for the stability of the set-up.

Furthermore, a three dimensional simulation was carried out to test a major deficiency of two-dimensional simulations: treating a system which is unstable to MRI in an axisymmetric manner leads to an enhanced 'two-channel-solution' of poloidal MRI (Hawley and Balbus, 1992), which tends to exhibit long lasting radial filaments along which angular momentum can be carried away (Bodo *et al.*, 2008). These structures are destroyed by toroidal modes of parasitic instabilities in the full 3D treatment (Goodman and Xu, 1994). Another known problem of 2D simulations of MRI is that magnetic turbulence will fade due to the absence of dynamo modes. While the latter is only important on a much larger time scale than those of the simulations presented here, we will have to live with the former when performing axi-

name	N_r	N_θ	N_ϕ	$r_\mathrm{min}\,[R_\mathrm{g}]$	$r_\mathrm{max}\,[R_\mathrm{g}]$	θ_min	θ_max	$\Delta\phi$
QUAD	4096	256	1	5	800	0.05	$\pi - 0.05$	2π
NONMAG	768	256	1	5	150	0.05	$\pi - 0.05$	2π
QUAD_3D	256	84	42	5	150	0.05	$\pi - 0.05$	$\pi/2$

***Table 3.1** – **Set-up of the simulations** QUAD, NONMAG **and** QUAD_3D. $N_{\mathrm{r},\theta,\phi}$ denote the number of cells in each spatial dimension, $r_\mathrm{min,max}$ indicate the inner and outer boundary of the domain, $\theta_\mathrm{min,max}$ the upper and lower limit of the poloidal angle and $\Delta\phi$ denotes the extension of the domain in the azimuthal direction.*

symmetric simulations, since the rate at which these parasitic instabilities act is proportional to the amplitude of the magnetic perturbations.

To check hydrodynamic stability and the effect of axisymmetry we performed two tests (see table 3.1):

NONMAG: Same as QUAD but magnetic field vanishes.

QUAD_3D: Three dimensional simulation with magnetic field.

In the following we will describe the general set-up (section 3.1) and the results of the non magnetised case NONMAG (section 3.2), the basic quadrupole simulation QUAD (section 3.3), the 3D simulation QUAD_3D (section 3.4) and discuss the results in section 3.5.

3.1 Set-up

The computational domain was initialised containing a torus in the well of the effective potential (Igumenshchev *et al.*, 1996):

$$\Phi_\mathrm{eff} = \Phi_\mathrm{PW} + \int_r^\infty \frac{L^2(r')}{r'^3}\,dr'. \tag{3.1}$$

Φ_PW is the pseudo potential proposed by Paczynsky and Wiita presented in section 2.3.4. For a constant angular momentum L, the integral can be solved analytically. The isocontours of the effective potential then determine the shape of the torus. In figure 3.1 the effective potential is shown for different values of the angular momentum L (left panel) and as a contour plot (right panel). The contour chosen for our simulations is printed with a bold line. This results in a torus which on the equatorial plane extends from $20\,\mathrm{R_g}$ to $60\,\mathrm{R_g}$ ($R_\mathrm{g} = MG/c^2$). Its density and pressure maximum then reside at a distance of $30\,\mathrm{R_g}$ from the centre of gravitation on the equatorial plane.

The density of the atmosphere is 10^{-4} in code units where the maximum density of the torus is defined to be of unity. Initially the pressure was calculated assuming an isothermal plasma with a constant speed of sound of approximately 5% of the speed of light.

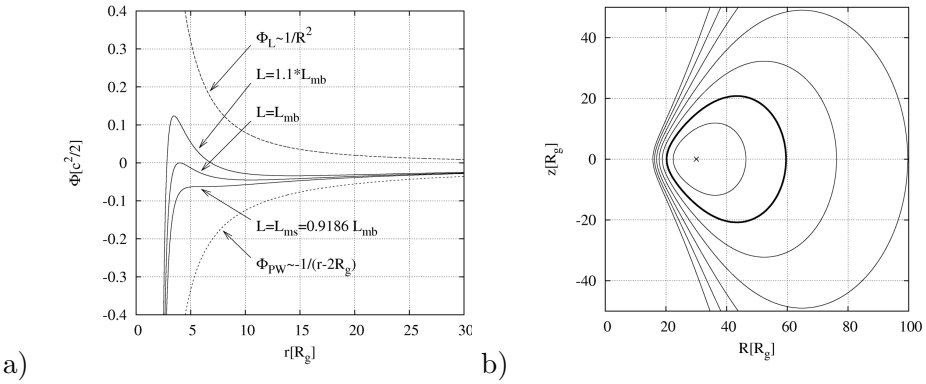

***Figure 3.1** – **Effective potential**. The left panel shows the gravitational pseudo potential Φ_{PW}, the angular momentum potential Φ_{L}, and the resulting effective potential Φ_{eff} for different values of the angular momentum L (solid curves). Lmb and Lms mean the angular momentum at the marginally bound and the marginally stable orbit, respectively. The right panel shows contour lines of $\Phi_{\mathrm{eff},L=1.47}$ which is the angular momentum used for the simulations of this work. The bold contour line indicates the surface of the resulting torus the density maximum is marked with a cross.*

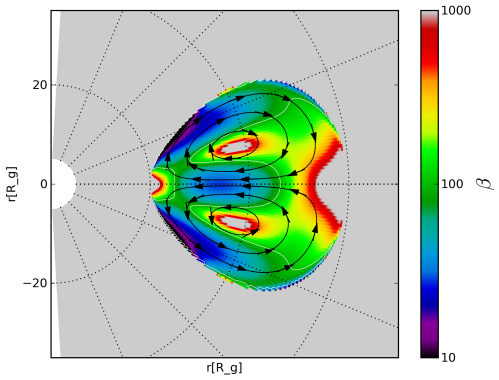

***Figure 3.2** – **Setup of case** `QUAD`. Colours indicate the plasma $\beta \equiv 8\pi p_{\mathrm{gas}}/B^2$, field lines show the magnetic field. The contours (white) marks $\beta = 100$.*

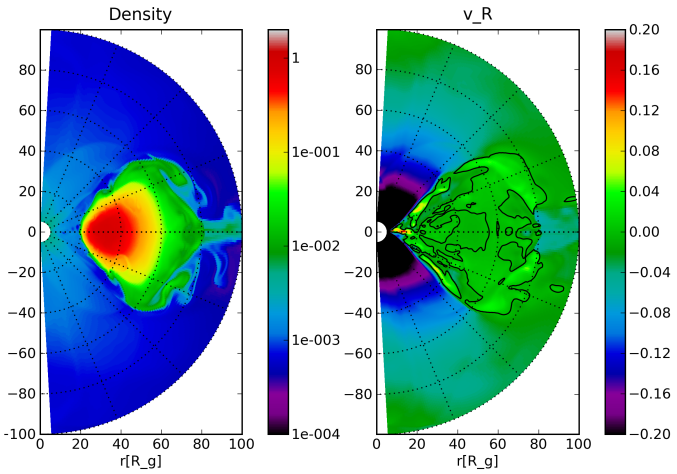

Figure 3.3 – Density and radial velocity of case `NONMAG`***.*** *Density is shown on the left panel in a logarithmic scale in code units (initial density maximum = 1). The right panel shows radial velocity in linear colour scale in units of c. The snapshot was taken after* 5000 lct *from a simulation without initial magnetic field. Minor turbulence occurs but the torus persists.*

The torus rotates with constant angular momentum around the axis, the atmosphere is not rotating. The velocity field was perturbed randomly by 1% of its original value.

The magnetic field was initialised setting the vector potential $\mathbf{A} = A_\phi \mathbf{e}_\phi$ proportional to the density and a sine functions in the θ and r direction:

$$A_\phi \propto \rho \sin(f(\theta)) \sin(g(r)).$$

Well-directed use of the functions $f(\theta)$ and $g(r)$ makes it possible to get the desired number and arrangement of the magnetic loops. For this case we set up two vertically stacked poloidal loops resulting in a quadrupole (fig. 3.2). After determining the geometry of the magnetic field, its strength was set to satisfy $\beta \equiv 8\pi p_{\mathrm{gas}}/B^2 = 100$ on average. For the non magnetised case `NONMAG`, A_ϕ was set to 0 and the same solver (RMHD/HLLD) (see section 2.5) was used.

An overview of the set-ups is given in table 3.1.

3.2 Test case without initial magnetic field

In the absence of a magnetic field, the torus was tested to be stable in the axisymmetric set-up (figure 3.3). In full 3D simulations it would be subject to hydrodynamic instabilities (Papaloizou and Pringle, 1983), but the typical time scale of 3D hydrodynamic instabilities is several orders of magnitude larger than the integration times of the simulations presented here.

In fact the torus is subject to some turbulence fringing at its surface. Also small amounts of matter flow radially outwards mainly along the equatorial plane. The former can be explained by numerical noise, minor deviations from the stationary solution due to the finite resolution of the grid and

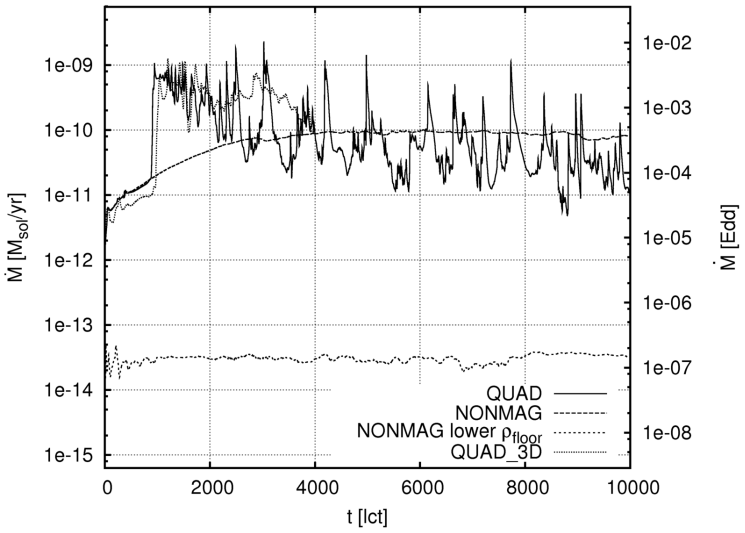

***Figure 3.4* – *Accretion rate for* NONMAG, QUAD *and* QUAD_3D.** *Mass flux at the inner boundary for the cases NONMAG, QUAD and QUAD_3D. We assumed an accretion efficiency of $\eta = 0.1$ for the Eddington scale at the right vertical axis. As an application to accretion on a stellar black hole we assumed $M_{\mathrm{BH}} = 10 M_{\odot}$ and $\rho_{\max} = 10^{-7}\,\mathrm{g/cm^3}$. 'NONMAG lower ρ_{floor}' is the result of a test similar to case NONMAG but with the atmospheric density and numerical floor value for the density set to 10^{-6}, i.e. 2 orders of magnitude lower than in the other cases.*

mostly from friction with the non rotating atmosphere. The latter, matter loss at the back of the torus, is caused by the flat potential at large radii which makes it easy for matter to escape.

As seen in figure 3.4 accretion occurs also in the non magnetic case. This is expected, because the atmosphere is set up to be non rotating. Thus gravitational pull is not equilibrated by centrifugal forces. Therefore a stationary mass inflow as according to (Bondi, 1952) builds up.

This infall of matter sets off much slower than in the magnetised case but finally reaches the same value as in the case of the magnetised torus when the minimum density is set to 10^{-4} in code units. To check whether the saturation value of the accretion rate is determined by the density in the atmosphere, we simulated the NONMAG set-up with a lower floor value (and initial atmospheric value) of 10^{-6} in code units. Figure 3.4 shows that the accretion rate drops even more than two orders of magnitude. This indicates that accretion is a mere result of the non rotating atmosphere filled with low density matter.

The velocity map (figure 3.3) for case NONMAG also indicates that mass inflow takes place only in the atmosphere, while the radial velocity in the

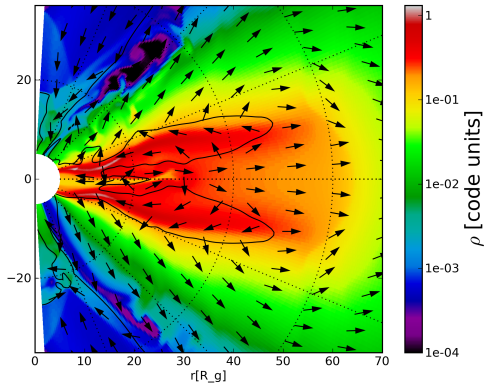

***Figure 3.5** – **Density and velocity of the inner region of case `QUAD` after 1000 lct.** Density is shown in a logarithmic colour scale in code units (initial density maximum = 1). Arrows indicate the direction of velocity and the contours mark $v_r = 0$, i.e. separates outflow from inflow regions. The snapshot was taken after 1000 lct.*

torus remains close to zero. In the atmosphere, density was set to the minimal allowed density of 10^{-4} in code units to avoid numerical problems in the presence of magnetic fields. Setting the density lower we would get less accretion for the non magnetic case and in the limit of an absolute vacuum (which is impossible to be simulated with the applied numerical scheme) the accretion rate would vanish.

Accretion through the atmosphere does not alter the results for the magnetic cases because as we will see below, accretion in these cases happens close to the equatorial plane, while the atmosphere is filled with outflowing material.

3.3 General structure of accretion and outflows

3.3.1 Accretion flow

Due to the weak magnetisation and differential (Keplerian) rotation the torus is unstable to the magnetorotational instability. The MRI enhances perturbations within 4/3 of a local orbital period (compare to equation (2.43)) inside the torus. This corresponds to 562 lct at the inner edge of the initial torus. Since the MRI and the magnetic tension cause angular momentum to be transported outwards, matter starts to accrete (see fig. 3.4).

Shortly after the onset of the simulation, matter concentrates in two regions located in the centres of the magnetic loops. Matter accretes along two paths having their origin in these regions (fig. 3.5). This pattern is disrupted at small radii after few orbits. Nevertheless, the primary structure of two accretion channels persist at larger radii. Matter keeps concentrating inside magnetic loops where magnetic pressure is low and avoids regions with large magnetic pressure (fig. 3.6). In figure 3.7 a schematic illustrates the global structure of an accretion flow with an initial quadrupole field.

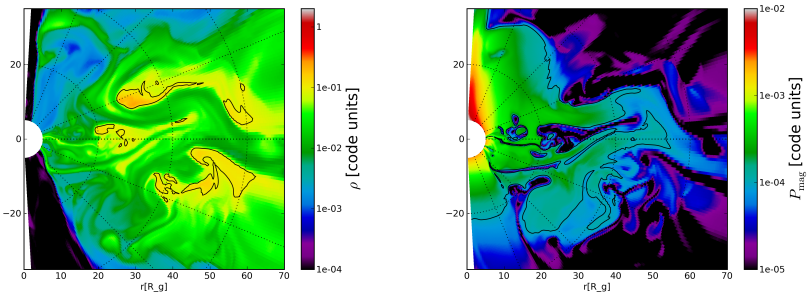

***Figure 3.6** – **Density and magnetic pressure of case `QUAD` after 4000 lct.** On the left hand side density is shown in logarithmic colour scale in code units (initial density maximum = 1), the contour line marks $\rho = 0.1$. On the right hand side the magnetic pressure is plotted in logarithmic colour scale in code units with a contour line at 10^{-4}. The snapshots were taken after 4000 lct.*

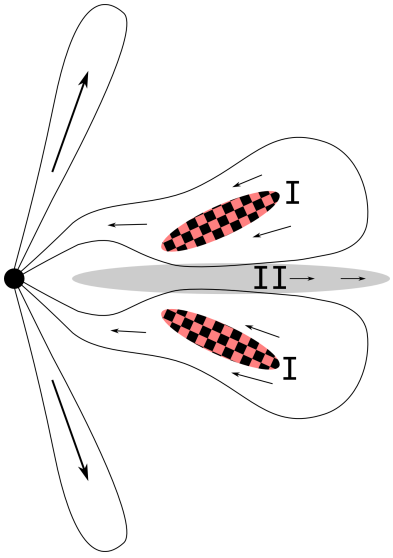

***Figure 3.7** – **Schematic of the accretion flow structure for case `QUAD`.** Lines denote magnetic field and arrows symbolise radial velocity. Please note that the θ-component of the velocity was not taken into account for the sake of clarity. Region `I` (chequerboard pattern) and `II` (grey) are regions of high and low density, respectively.*

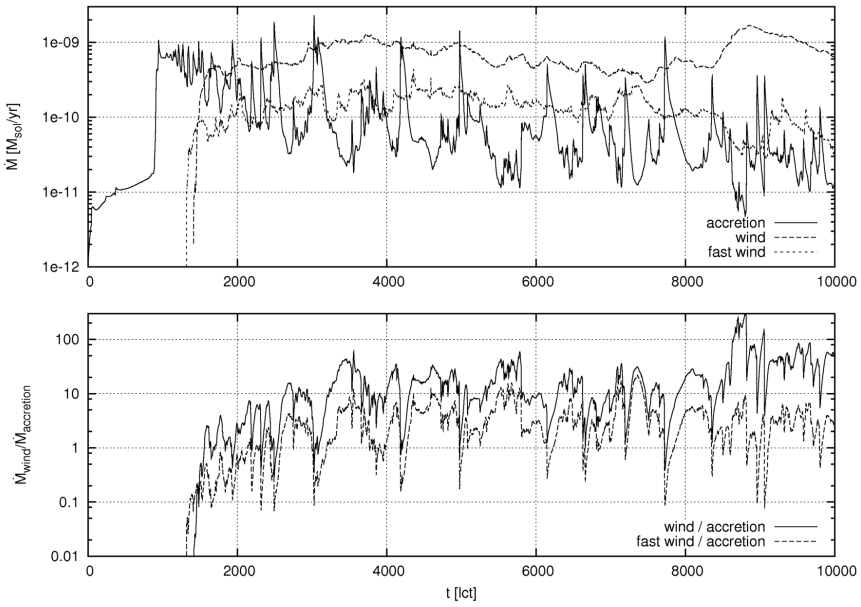

***Figure 3.8* – *Accretion and wind for case* `QUAD`.** *The upper panel shows accretion rate (like in fig. 3.4) and rate of mass flow at* $150\,\mathrm{R_g}$*. During the first* 1200 lct*, mass falls in at that radius and is not plotted. With* fast wind *we denote winds with a radial velocity* $> 0.2\,c$*.*

3.3.2 Coronal winds

Most of the torus' matter forms a coronal wind that sets off approximately 1300 lct after the beginning of the simulation (fig. 3.8), which forms directly above and below the torus and at the outer edge of the initial torus (fig. 3.5). The loss rate of matter due to the coronal wind is 10 to 100 times larger than the rate of accreted matter. An analysis of the total energy in the corona indicates that the wind is energetically unbound. Therefore it can be interpreted as the main transport channel for angular momentum.

We find a notable coupling between the rate of mass loss by winds and the accretion rate: small rises in the wind rate are often followed by a sharply augmented accretion. This supports the hypothesis that winds are an essential component of an accreting system.

3.3.3 Fast winds

Close to the inner boundary ($r < 10\,R_\mathrm{g}$) a fast, narrow, tenuous outflow is ejected. This outflow forms at approximately $1300\,lct$ simultaneously with the slow wind (fig. 3.8) and propagates at an angle of $\theta \lesssim 30°$ measured from the axis of rotation. Its matter has its origin some R_g above and below the equatorial plane. Radially it arises from a zone between the zone of accretion

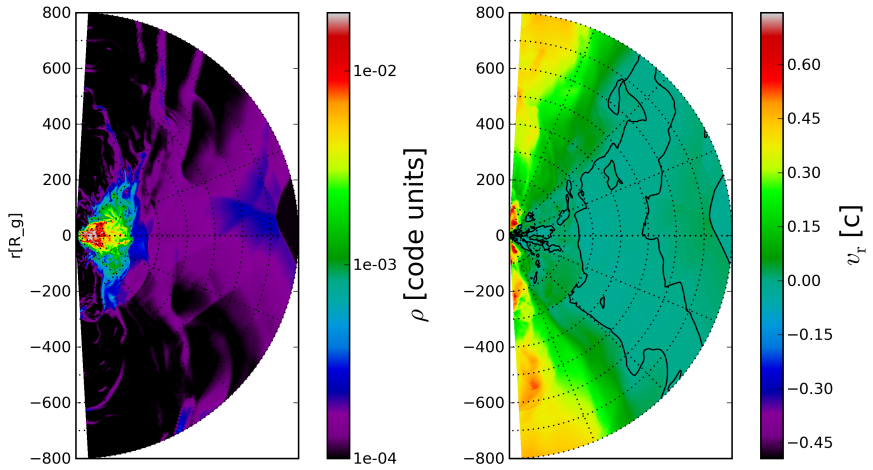

Figure 3.9 – Density and radial velocity for case `QUAD` ***after10000 lct.*** *The panels show the density (left) and the radial component of the velocity (right) in logarithmic and linear colour scale, respectively. The contours in the velocity map indicate* $v_r = 0$.

(on and adjacent to the equatorial plane) and the region from which the slow wind arises (at radii greater than $20\,R_g$) (see figure 3.5).

It carries almost no angular momentum due to its low density, which is close to the numerical floor value, and due to its relatively small distance from the axis of rotation. Nevertheless it is rotating as described in detail in section 3.3.4 The rate at which mass is ejected through this jet-like outflow is about an order of magnitude lower than the accretion rate (figure 3.8). A closing interpretation of the mass flux through the fast wind is difficult because choosing a smaller numerical floor value for the density will certainly result in a lower rate for the fast wind. This could not be tested however, because a smaller floor value results in a higher Alfvén speed causing a dramatically smaller time step which makes it impossible to reach even a few hundred light crossing times. Furthermore the applied numerical scheme is not stable for the force free limit of low β plasmas.

3.3.4 Rotation patterns

While in the former sections we focused on the radial movement of the outflows we will now examine the azimuthal velocity structure. As expected, the coronal winds corotate with the disc. This makes them a strong channel for carrying angular momentum outwards.

In contrary to intuition, the fast jet-like winds show a different behaviour: they show recurring events of retrograde rotation. They are launched with a period of approximately 100 lct which corresponds to a frequency of 200 Hz

for a central black hole of $M = 10\,M_\odot$. They reach the outer boundary and we expect them to persist as long as the outflow, as they are energetically unbound.

In fig. 3.10, we observe a strong correlation between the orientation of the azimuthal magnetic field and the sense of rotation in the region of fast outflow. The magnetic field seems to be responsible for turning around the orientation of rotation.

In order to get insight into this behaviour, we inspect the toroidal component of the induction equation (equation (2.7)) for the axisymmetric case which is

$$\partial_t B_\phi = -(\mathbf{v}_\mathrm{p} \cdot \nabla) B_\phi + R\,\mathbf{B}_\mathrm{p} \cdot \nabla\Omega - B_\phi\,\nabla \cdot \mathbf{v}, \tag{3.2}$$

where $\mathbf{B}_\mathrm{p}$ denotes the poloidal part of $\mathbf{B}$. The index p refers to the poloidal part of a vector, R denotes the radius in cylindrical coordinates and $\Omega = v/R$ is the angular velocity. The first term on the right hand side describes advection, the second term inserts a dependence on shearing and the last term is a compression term. As a first approximation, we assume that compression is of minor importance in the region of interest and neglect the this last term.

To investigate how the azimuthal velocity switches orientation, we suppose B_ϕ is positive. Due to the Keplerian rotation of the disc, $\nabla\Omega$ is negative and mainly parallel to e_r (close to the black hole this holds for all angles θ). $\mathbf{B}_\mathrm{p}$ can have either sign and is, close to the central mass, also radially dominated. In regions where $\mathbf{B}_\mathrm{p}$ is positive, the second term becomes negative, which leads to a decrease in B_ϕ. The azimuthal components of the magnetic field and the velocity are coupled by the axisymmetric equation of angular momentum which one derives from the general momentum equation (equation (2.5), see Balbus (2004) for details),

$$\partial_t(R\rho v_\phi) + \nabla \cdot (\langle \rho \mathbf{v}_\mathrm{p} \rangle R^2 \Omega) = -\nabla \cdot (\langle \rho \rangle R \mathbf{W}_\mathrm{p}). \tag{3.3}$$

The poloidal component of the stress tensor (given in equation (2.14)) yields

$$\mathbf{W}_\mathrm{p} = \langle \delta v_\phi \boldsymbol{\delta} \mathbf{v}_\mathrm{p} - \frac{B_\phi \mathbf{B}_\mathrm{p}}{4\pi\rho} \rangle.$$

From equation (3.3) we find – provided the Alfvén speed is of the order of the kinetic velocity fluctuations – that magnetic fields will drag matter along. That means that when B_ϕ becomes negative, it forces matter into a negative rotation as well. Now the shearing term in equation (3.2) will switch sign, because locally, $\nabla\Omega$ becomes positive. This will invert the described mechanism: B_ϕ increases until it becomes positive, v_ϕ follows and the process starts again.

The same scheme works at places where B_ϕ and $\mathbf{B}_\mathrm{p}$ are both negative.

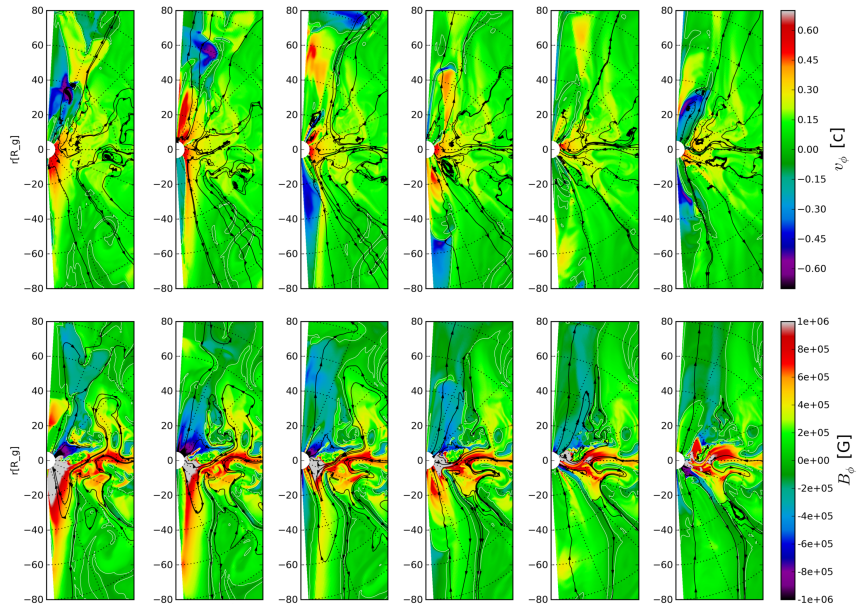

Figure 3.10* – *Recurring events of retrograde rotation in the fast outflow *The upper set of panels show the azimuthal velocity in colour code and the poloidal velocity as streamlines. The lower panels show the azimuthal component of the magnetic field in colour code and the poloidal component as field lines. White contours mark $v_\phi = 0$ and $B_\phi = 0$ respectively. Velocity is measured in units of c, magnetic field in cgs (Gauss). The snapshots were taken with a frequency of* 50 lct *starting* 4000 lct *after the beginning of the simulation.*

3.4 Simulation in three dimensions

A simulation in 3D was performed to check our axisymmetric set-up for consistency. In three dimensions, matter starts to accrete about 100 lct later and the initial peak of the accretion rate is a little bit lower than in case `QUAD` (figure 3.4). After another hundred light crossing times the same mean value of accretion is reached, but the fluctuations are somewhat smaller. These differences can be explained by the lower resolution of the three dimensional grid.

3.5 Discussion

The model set-up `QUAD` (magnetic field is a poloidal quadrupole, $\beta = 100$) shows all features of interest for this work: a turbulent accretion body, spherical wind production and a fast jet-like outflow along the axis of rotation.

A test with vanishing magnetic field strength and a another test in three dimensions showed that the results of this set-up are quite reliable:

- It is the magnetic effect which drives turbulence and accretion, since neither of them happen in the non magnetised case `NONMAG`.
- The non axisymmetric effects are minor, as the results of the 3D case `QUAD_3D` and the model case `QUAD` resemble each other to a high degree. Minor differences can be explained by the differences in poloidal resolution of the grid.

Accretion sets off after approximately one orbital period at the density maximum. This time scale of the magnetic fields acting on the torus is in good accordance with other simulations (e.g. De Villiers and Hawley, 2003; Beckwith *et al.*, 2008).

Coronal winds form simultaneously with accretion due to the requirement of angular momentum to be transported outwards. The speed of the wind is less than 0.1 c. It propagates spherically providing a mass flux 10–100 times higher than the accretion rate.

The **fast outflow** can be interpreted as the seed of a collimated jet further out from the accreting system. Its radial and azimuthal velocity reach up to 60% of the speed of light, which is in very good agreement with measurements of the jet of CYG-X1 (Stirling *et al.*, 2001) and other observations. Other observed jets from black hole accretors evince velocities ranging from about 0.1 c to 0.99 c.

The jet is energetically unbound (figure 3.9), which bears the possibility that the outflow gets accelerated further out. Also physical mechanisms not covered by these simulations can cause the collimation and speed observed in real jets. Such a mechanism could be the gravitomagnetic forces of a

rotating black hole (Blandford and Znajek, 1977) or rotating large scale magnetic fields seeded in the outer parts of the accretion disc (Blandford and Payne, 1982).

The jet was found to **rotate in retrograde direction** recurrently. We proposed an explanation by the coupling of angular momentum and azimuthal magnetic field in ideal MHD. This bulk movement of parts of the jet can be interpreted as an *extreme zonal flow* as described by Johansen *et al.* (2009). They simulated a high β plasma in shearing box simulations representing a local patch of an accretion disc. In these simulations the found zones of disc matter moving with alternating sub- and super-Keplerian velocity and explain this by the structure of the magnetic field. In our simulation this effect could be enhanced due to the low plasma β which makes the matter much more dependent on the magnetic field dynamics.

In order to investigate which property of the set-up causes, enhances or inhibits the formerly described features, we need to systematically alter parts of the set-up leaving all other the same. This will be done in the following section. We will change the torus' size and position (section 4.1), the strength of the magnetic field (section 4.2), the topology of the poloidal magnetic field (section 4.3) and finally add a cooling term to the algorithm (section 4.4).

Nobody said it was easy.
No one ever said it would be this hard.
— Chris Martin

4 Variations of the model case and their consequences

Numerical Simulations tend to be set up in a simplified manner. Partly this is an intrinsic problem of the method. One needs to initialise the domain with a well-defined state in order to grant comparability to other works and to be able to extract the physical effect of interest. But we should be aware that initial set-ups based on analytical solutions will always be artificial. Experience shows that small changes in the setup can lead to big differences in the results.

To avoid extrapolating results of one specific set-up to the general case, we will vary different parameters of the set-up `QUAD`. In section 4.1 we will initialise tori with different size and positions, in section 4.2 we simulate tori with a stronger and weaker magnetic field, in section 4.3 we alter the geometry of the magnetic field and in section 4.4 we add a sink term to the energy equation emulating optically thin cooling by synchrotron radiation.

Apart from that we aim to answer which properties give rise to which features. In detail we will investigate the onset of accretion, launching of jet-like and slow outflows, rotation structures as well as turbulent behaviour of the torus and its surroundings.

4.1 Position and size of the torus

We will present a series of simulations testing several geometric set-ups of the torus. The parameters we will vary are the position of the inner border of the torus r_{in} and the location of the density maximum $r_{\rho_{\mathrm{max}}}$.

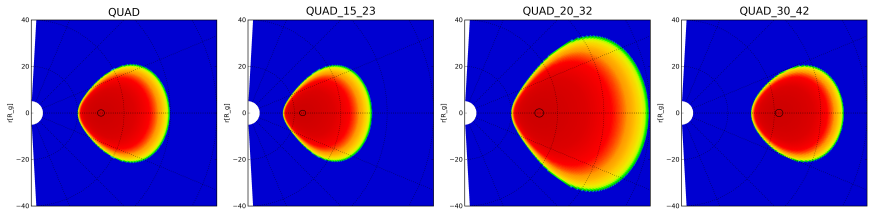

***Figure 4.1** – **Set-ups of the simulations** `QUAD`, `QUAD_15_23`, `QUAD_20_32`, `QUAD_30_42`. The panels show density maps of the initial configurations in logarithmic scale. The black contour marks $\rho = 0.99\rho_{\max}$ hence indicating the location of the density maximum.*

4.1.1 Set-up

The quadrupole set-up (`QUAD`) was used as the base configuration. In this configuration the inner edge of the torus lies at $r_{\text{in}} = 20\,\text{R}_\text{g}$ and its pressure and density maximum at $r_{\rho_{\max}} = 30\,\text{R}_\text{g}$. We varied these two parameters to investigate their effect on the torus' evolution. The tested cases are shown in table 4.1 and figure 4.1. We varied the radial position of the torus in cases

name	$r_{\text{in}}\,[R_\text{g}]$	$r_{\rho_{\max}}\,[R_\text{g}]$	τ_{MRI} at $r_{\text{in}}\,[lct]$	τ_{MRI} at $r_{\rho_{\max}}\,[lct]$
`QUAD`	20	30	562	1032
`QUAD_15_23`	15	23	365	693
`QUAD_20_32`	20	32	562	1137
`QUAD_30_42`	30	42	1032	1710

***Table 4.1** – **Set-up of the simulations** `QUAD_15_23`, `QUAD_20_32`, `QUAD_30_42`. The magnetic field is set up as described in section 3.1.*

`QUAD_15_23` and `QUAD_30_42` and the size of the torus in case `QUAD_20_32`. If accretion is coupled to the development of MRI we expect the onset of accretion to be correlated to the local growth rate of MRI at either the radius of the inner edge of the torus r_{in} or the position of the density maximum $r_{\rho_{\max}}$.

4.1.2 Results

The accretion rates for the tested cases are shown in figure 4.2. The onset of accretion seems to be a function of the radial position of the density maximum $r_{\rho_{\max}}$ rather then of the inner edge. For better visibility we plotted the smoothed accretion data scaling the time axis to the orbital period of $r_{\rho_{\max}}$ (figure 4.3). The hypothesis proves true as the steep rise of the accretion rate happens for all cases after approximately one orbit at the density maximum.

All cases show a similar overall structure and dynamics when scaled to the appropriate orbital periods. The fast wind sets off after approximately

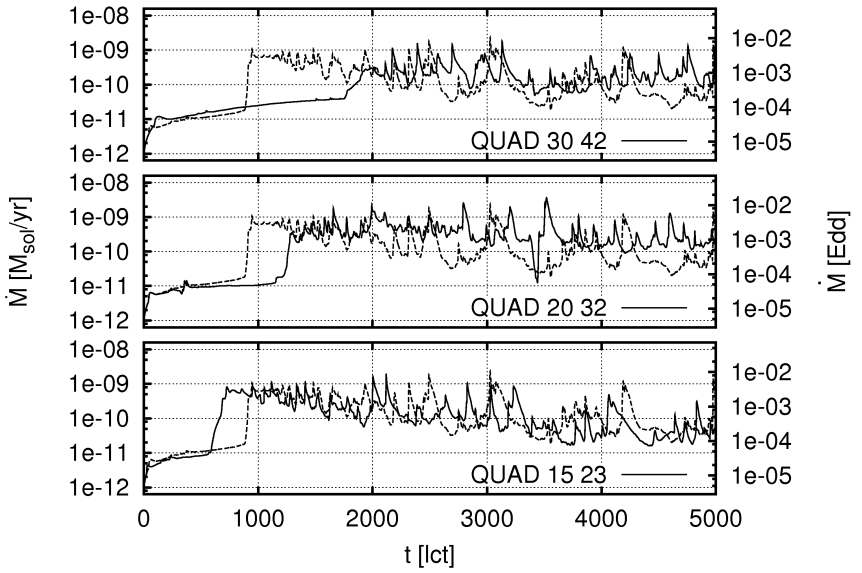

Figure 4.2 – Accretion rates for different initial torus positions. *The mass flux across the inner boundary of the simulated domain is plotted for the different magnetic set-ups. We assumed an accretion efficiency of $\eta = 0.1$ for the Eddington scale at the right vertical axis. As an application to accretion on a stellar black hole we assumed $M_{\mathrm{BH}} = 10 M_{\odot}$ and $\rho_{\mathrm{max}} = 10^{-7}\,\mathrm{g/cm^3}$ for the scale on the left vertical axis. The accretion rate of case* `QUAD` *is plotted dashed in every panel for comparison.*

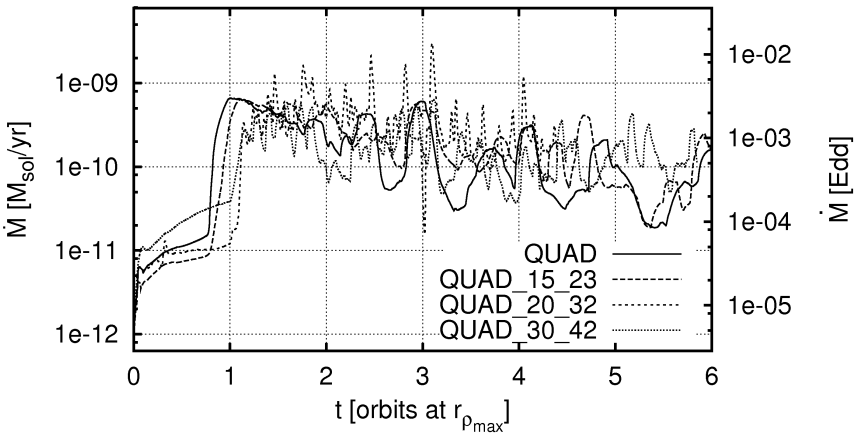

Figure 4.3 – Smoothed accretion rates for different initial torus positions. *Same as figure 4.2 but with smoothed data. The smoothing length is 100 lct. The plot were scaled to the orbital period of the radius of maximum density for each model.*

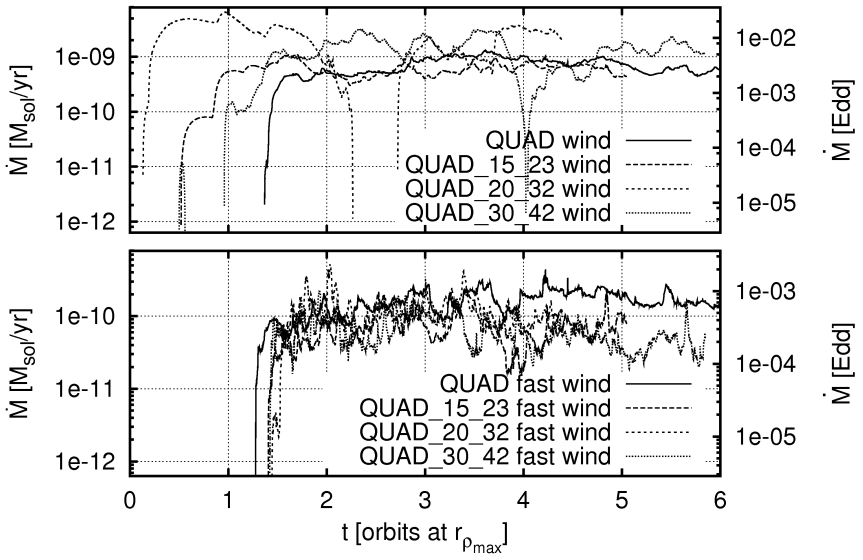

Figure 4.4 – Outflow rates for different initial torus positions. *The rate of mass flux through the outer boundary is plotted for the discussed set-ups. The upper panel shows the flux integrated over the whole outer boundary. The data of the lower panel was only integrated over boundary cells where $v_\mathrm{v} > 0.2$. Units are as described in figure 4.2.*

1.3 orbital periods in all cases (figure 4.4). Interestingly that is not the case for the total wind; the first set-up to start an outflow is case `QUAD_20_32`. Also this wind is the one transporting most mass outwards. There are two possible reasons for that: a) The back of the torus is located at $80\,\mathrm{R_g}$, which is further out than any other set-up, b) the torus is thicker and thus contains more mass than any other. If a) was the case, the next set-up to produce a wind should be `QUAD_30_42`, but this is not the case. Hence we assume that the larger volume and mass account for the stronger wind. Nevertheless the wind of case `QUAD_20_32` is not as stable as the others, as we observe a net inflow during the 3^{rd} orbit. The next set-up to produce a wind is case `QUAD_20_32`. We hold the torus' proximity to the black hole responsible for that.

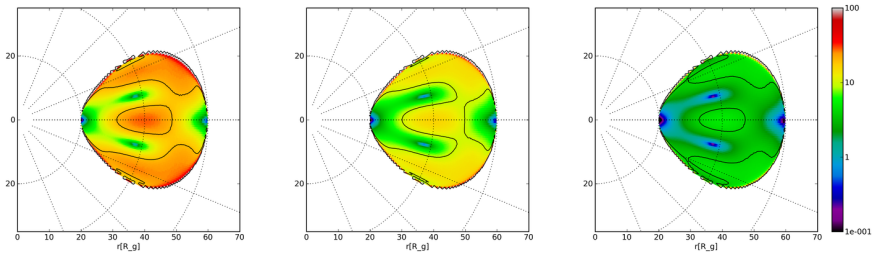

***Figure 4.5** – **Most unstable MRI modes of the simulations** `QUAD_BETA1.5` **and** `QUAD_BETA3`. The colour maps show the fastest growing perturbation wavelength in units of R_g in logarithmic scale for case `QUAD_BETA1.5` (left), `QUAD` (middle) and `QUAD_BETA3` (right) Contours are drawn at the typical wavelength (see table 4.2).*

4.2 Magnetic field strength of the plasma

The strength of the magnetic field can be measured in unit of the pressure by using the plasma parameter $\beta = 8\pi p_{\text{gas}}/B^2$. Without magnetic fields (i.e. $\beta = \infty$) accretion is inhibited and the torus remains as initialised (see section 3.2). It is subject to hydrodynamic instabilities but not to MRI. Large β tori will be unstable to perturbations of small wavelengths and vice versa. Natural limits on β are given by the size of the torus and the grid resolution.

We test the onset and the further behaviour of the accretion flow and the ejection of matter for several values of beta.

4.2.1 Set-ups

The starting point and reference again is the simulation `QUAD`. The inner border of the torus is located at $20\,R_g$, the density maximum at $30\,R_g$. The magnetic field forms a quadrupole.

name	description	typical $\lambda_{\max}[R_g]$
`QUAD`	reference, $\beta = 10^2$	10
`QUAD_BETA1.5`	like `QUAD` but with $\beta = 10^{1.5} \approx 31.6$	20
`QUAD_BETA3`	like `QUAD` but with $\beta = 10^3$	4

***Table 4.2** – **Set-up of the simulations** `QUAD_BETA1.5` **and** `QUAD_BETA3`. All properties of the torus except for the plasma β are as described in section 3.1.*

4.2.2 Results

The most unstable MRI mode can be resolved and fits into the torus in all cases. Therefore, from an analytical point of view, MRI should work about

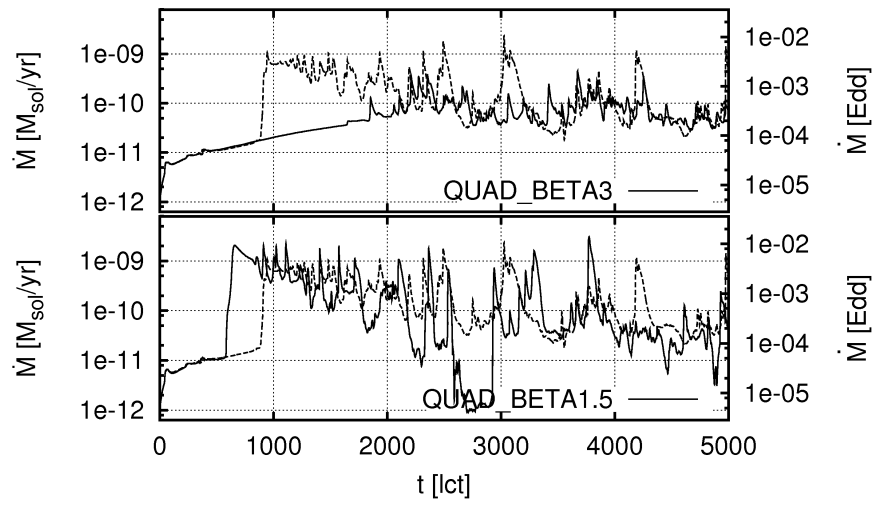

Figure 4.6* – *Accretion rates for different initial magnetic strength. *The mass flux across the inner boundary of the simulated domain is plotted for the different magnetic set-ups. We assumed an accretion efficiency of $\eta = 0.1$ for the Eddington scale at the right vertical axis. As an application to accretion on a stellar black hole we assumed $M_{\mathrm{BH}} = 10 M_{\odot}$ and $\rho_{\max} = 10^{-7}\,\mathrm{g/cm^3}$. The accretion rate of case `QUAD` is plotted dashed in every panel for comparison.*

the same in all three cases. But the results of the simulations differ strongly as the value of the plasma β changes (figure 4.7).

For the less magnetised case of $\beta = 10^{1.5} \approx 31.6$ we find accretion and ejection very similar to case `QUAD`. The fast winds are not as fast as in the model case and the torus gets disrupted more quickly. This can be explained by the higher magnetic pressure which literally pushes matter away. Why the jet-like outflows are a little bit slower than in `QUAD` can not be explained. But as the difference is not more than a few percent it could as well be a random result due to dynamic changes is the outflow speed.

For the less magnetised case of $\beta = 10^3$ we find the torus much more intact as in the other cases. It resides in its hydrodynamical equilibrium state as initialised. As opposed to the non magnetised case `NONMAG` an accretion channel on the equatorial plane builds up (figure 4.8). But instead of a fast outflow we also find accretion around the axis of rotation. Also the accretion rate does not expose a steep rise but it does show turbulent fluctuations.

This set-up is the only one that results in accretion via an equatorial disc but no jet-like outflow.

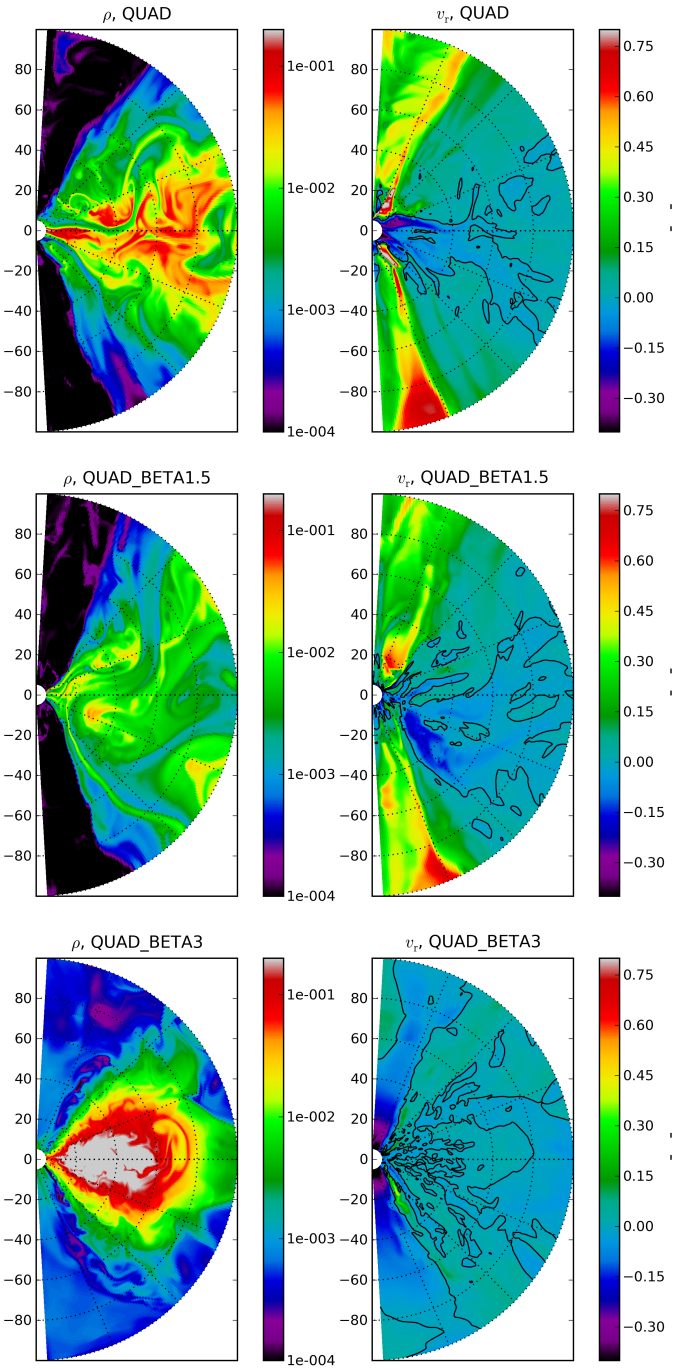

Figure 4.7 – Density and radial velocity after 5000 lct for different initial magnetic strength. *Density (logarithmic) and velocity (linear) are shown for the cases* `QUAD`*,* `QUAD_BETA1.5` *and* `QUAD_BETA3` *after 5000 lct.*

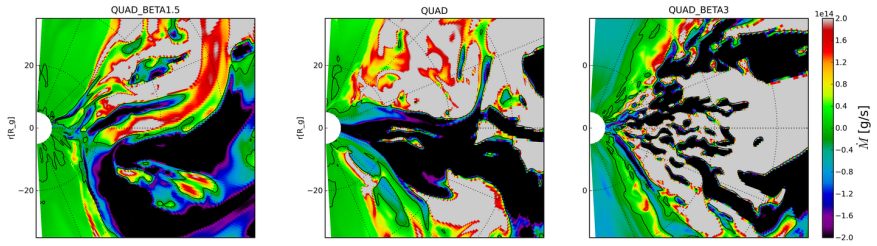

Figure 4.8 – Mass flux after 5000 lct for different initial magnetic strength. *Mass flux is shown for the cases* `QUAD`*,* `QUAD_BETA1.5` *and* `QUAD_BETA3` *after 5000 lct. Negative values denote infall.*

4.3 Magnetic field topology

Magnetic fields initiate and enhance accretion action. They are the crucial ingredient which causes angular momentum to be transported. Therefore it is reasonable to assume that the exact constitution of the magnetic field also determines the development and evolution of the disc and its outflows. We will experiment with the magnetic set-up to investigate how the accretion flow behaves under its influence.

4.3.1 Set-ups

We tested six different magnetic configurations shown in figure 4.9 and described in table 4.3. The average of the plasma β is approximately 100 in all simulations. That implies that in magnetic configurations of higher order (with more loops) the maxima and minima of magnetisation are more pronounced than in the low order configuration.

name	description
`DIP`	one poloidal loop
`QUAD`	two poloidal loops with contrary helicity
`SEXT`	three poloidal loops with alternating helicity
`OCT`	four poloidal loops with alternating helicity
`QUAD_MULT`	four radially stacked quadrupoles with alternating helicity
`MULT`	an arbitrary mixture of modes resembling a turbulent field

Table 4.3 – set-up of the simulations `DIP`***,*** `QUAD`***,*** `SEXT`***,*** `OCT`***,*** `QUAD_MULT` ***and*** `MULT`***.*** *The mean plasma β is 10^2 in all set-ups. All other properties are as described in section 3.1.*

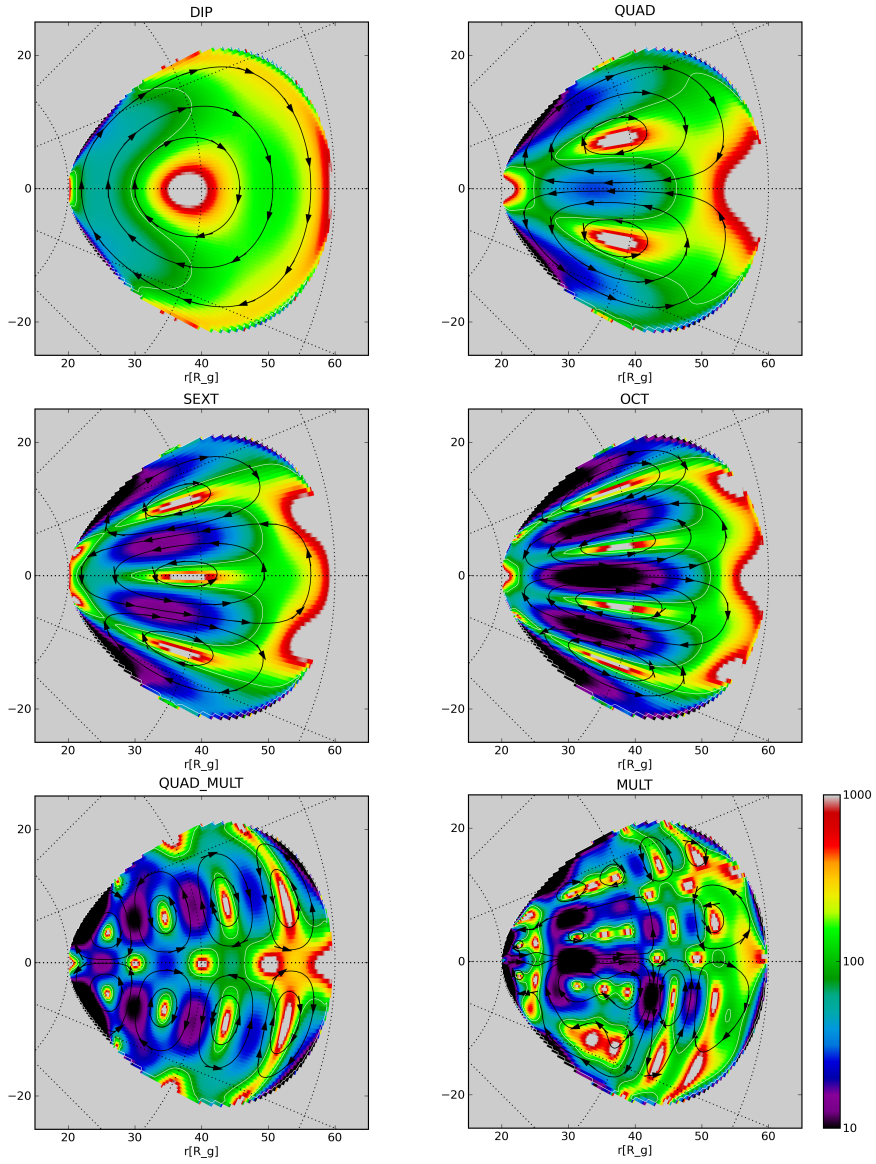

Figure 4.9 – ***Magnetic set-ups of cases*** `DIP`, `QUAD`, `SEXT`, `OCT`, `QUAD_MULT` ***and*** `MULT`. *Plasma* β *is shown in logarithmic colour scale ranging from* 10 *to* 1000. *Black lines with arrows indicate the magnetic field (density of the lines or alike does* not *reflect field strength). White lines indicate* $\beta = 100$.

4.3.2 Results

The structure of the accretion flow initially depends on the magnetic field setup. After the onset of accretion, matter concentrates in the centres of the magnetic loops, corresponding to region `I` in fig. 3.7. In that region, density, pressure and temperature are higher than in the surrounding area, while magnetic pressure is lower. Therefore, MRI is enhanced and matter is able to accrete. In fact, in the simulations we find that matter does not accrete mainly along the equatorial plane except for case `DIP`; it rather forms accretion channels of higher density and temperature as their surroundings. For case `QUAD` (`SEXT`, `OCT`), 2 (3, 4) channels form. After several 1000 lct these patterns are disrupted after being mixed heavily by turbulence.

The set-ups with a magnetic field of higher order lead to faster and more powerful accretion. We explain this by the fact that the wavelengths of the perturbations in the magnetic field determines the time scale on which MRI enhances them. The wavelength of the fastest growing wave in the centre of the torus is of the order of a few R_g, while the torus' thickness is approximately $40\,\mathrm{R_g}$ radially and vertically. In the case of the octupole, each magnetic loop has a vertical extension of about $10\,\mathrm{R_g}$, which makes this configuration more unstable to MRI than the others.

Furthermore, we find another explanation for the enhanced accretion in the cases with higher order magnetic geometry inspecting the mechanism of accretion; angular momentum is transported radially by the action of the r-ϕ-component of the stress tensor W, which is the sum of Reynolds and Maxwell stresses (equation (2.14)):

$$\mathsf{W} = \langle \boldsymbol{\delta v} \otimes \boldsymbol{\delta v} - \frac{\mathbf{B} \otimes \mathbf{B}}{4\pi\rho} \rangle,$$

where the angle bracketed variables denote mean values, δ stands for the fluctuation of a value and $\otimes$ is the dyadic product. For higher order magnetic setups, there is more magnetic energy in the radial component of the magnetic field as the loops are stacked vertically and their helicity alternates. Differential rotation will transform radial field lines into toroidal modes, which enhances accretion due to MRI.

Also, the higher order fields accrete along various paths, while in the dipole case matter accretes only along the equatorial plane. This enables more mass to flow inwards.

During the accretion phase, the rate fluctuates around a constant value of approximately $10^{-10}\,\mathrm{M_\odot/yr}$ for the case of a microquasar of $10\,\mathrm{M_\odot}$). The fluctuations have an amplitude of about two orders of magnitude. Case `DIP`, which lasted longer in enhancing its accretion, shows a somewhat higher accretion rate in the later phase of the simulation (figure 4.11). Looking at the integrated accretion rate (i.e. the so far accreted mass) in figure 4.12,

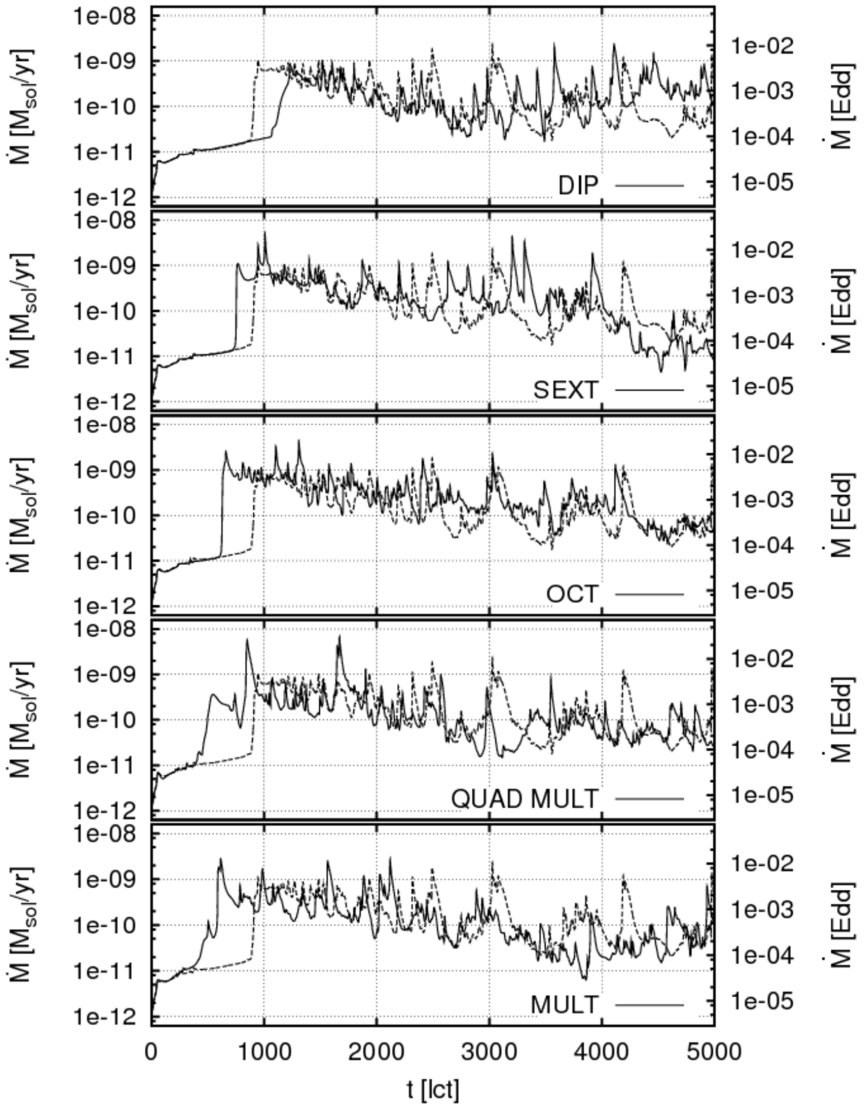

***Figure 4.10* – Accretion rates for different initial magnetic fields.** *The mass flux across the inner boundary of the simulated domain is plotted for the different magnetic set-ups. We assumed an accretion efficiency of* $\eta = 0.1$ *for the Eddington scale at the right vertical axis. As an application to accretion on a stellar black hole we assumed* $M_{\rm BH} = 10 M_\odot$ *and* $\rho_{\rm max} = 10^{-7}\,{\rm g/cm^3}$.

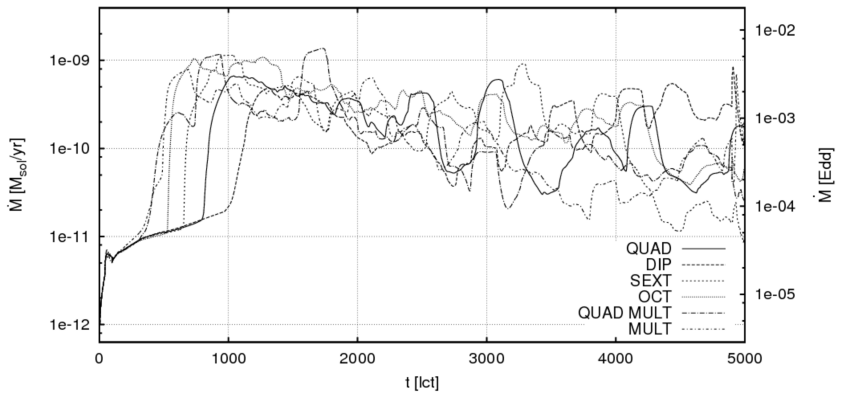

Figure 4.11 – Smoothed accretion rates for different initial magnetic fields. *Same as figure 4.10 but with smoothed data. The smoothing length is 200 lct.*

one finds that case `DIP` 'catches up' with the other simulations in terms of accreted mass. All of the setups accrete $\approx 4{\cdot}10^{15}$ g during the simulated time. This is equivalent to $\approx 10\%$ of the initial torus mass. Thus the accretion rate appears to be also a function of the mass which is still in the torus.

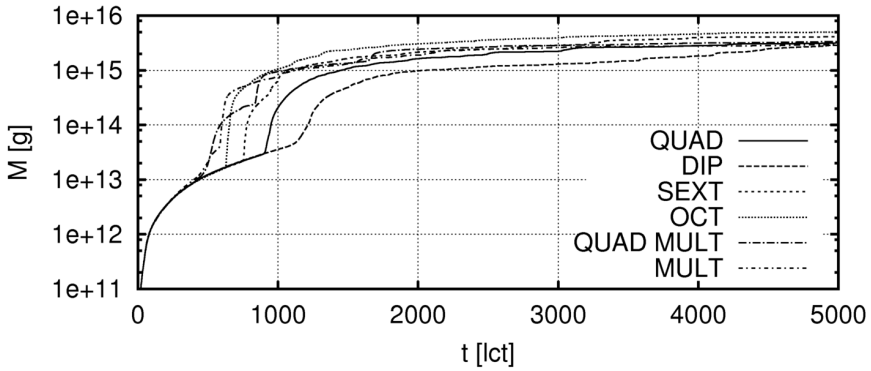

Figure 4.12 – Accreted mass for different initial magnetic fields. *The accretion rate was integrated over the elapsed time resulting in the total mass loss through the inner boundary. We assumed a black hole mass of* $10\,\mathrm{M}_\odot$ *and an initial maximum density of* $10^{-7}\,\mathrm{g/cm^3}$

4.4 Cooled accretion flows

Due to the presence of strong magnetic fields and hot (=fast) electrons, the most powerful cooling mechanism is non thermal synchrotron radiation. This emission will cool down parts of the disc and thus alter the overall dynamics. Therefore we expect the results to differ significantly from the model case `QUAD`.

To get reliable results on how much energy is emitted, where it is emitted and whether and how emission is correlated to accretion we implemented a energy sink emulating cooling via the synchrotron process (see section 2.3.4). Radiation is assumed to be radiated isotropically and integrated over all photon energies. Further interaction with matter is neglected as we are simulating the optically thin regime.

4.4.1 Set-ups

We used case `QUAD` as the basis and added a sink to the energy equation of the form (see equation (2.32)):

$$S_{\mathrm{synch}} = \partial_{\mathrm{t}} e_{synch} = 16 c \sigma_{\mathrm{T}} t_{TS} \frac{\varrho}{m_{\mathrm{p}}} P_{\mathrm{mag}} \Theta^2 e^{-1/\Theta}.$$

All other properties of the fluid are identical to case `QUAD`. This new set-up is referred to as `QUAD_SYN`.

4.4.2 Results

Also in the cooled case, matter starts to accrete soon after the beginning of the simulation (figure 4.13). The fact that it starts a few hundreds light crossing times earlier than in the non radiative case can be explained by the cooling down of the torus matter. As the parts of the torus where strong magnetic field occur cool down to $< 10^8$ K the torus is compressed, which enhances accretion (figure 4.15). The accretion rate does not fluctuate as strong as in case `QUAD`. This is also reflected in the power spectrum (figure 4.16) which is somewhat smaller in the radiative case.

The emitted synchrotron radiation is tightly correlated to the accretion rate. It follows the shape of the accretion not only on large time scales (figure 4.13) but also on short scales figure 4.14). We note that a rise in accretion is always preceded by a rise of synchrotron emission. The lapse between the maxima is only a few light crossing time. That means that most of the radiation must be emitted within few gravitational radii of the inner boundary. The emission map (figure 4.17) proves that the energy is only emitted from regions with sufficiently high density and mostly within $10\,\mathrm{R_g}$ from the centre of accretion. Also the emission is concentrated close to

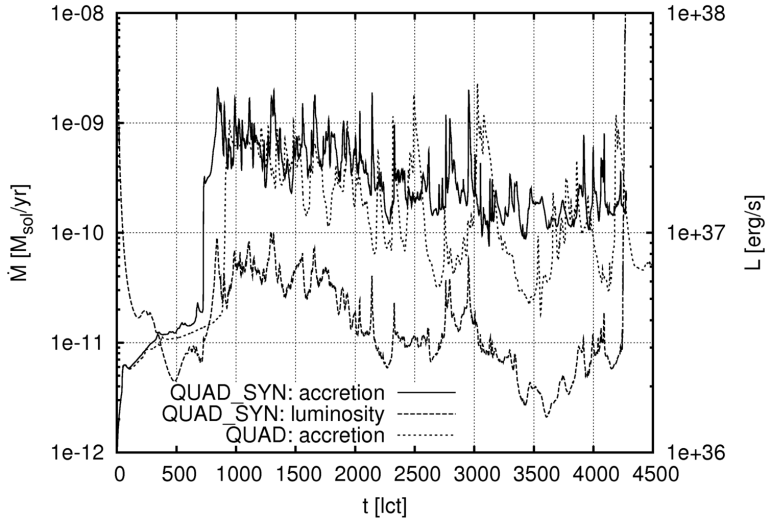

***Figure 4.13** – **Accretion rate and luminosity for case** `QUAD_SYN`. The plot shows accretion rate and synchrotron flux integrated over the whole domain for case `QUAD_SYN`. As an application to accretion on a stellar black hole we assumed $M_{\mathrm{BH}} = 10 M_{\odot}$ and $\rho_{\max} = 10^{-7}\,\mathrm{g/cm^3}$ for the left scale. The accretion rate of case `QUAD` is shown for comparison.*

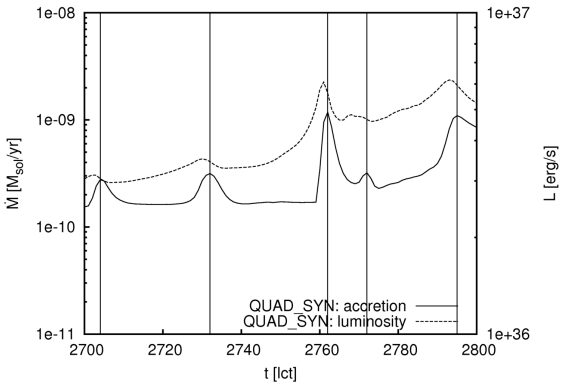

***Figure 4.14** – **Accretion rate and luminosity for case** `QUAD_SYN`. The plot shows a part of figure 4.13. Vertical lines indicate the local maxima of the accretion curve.*

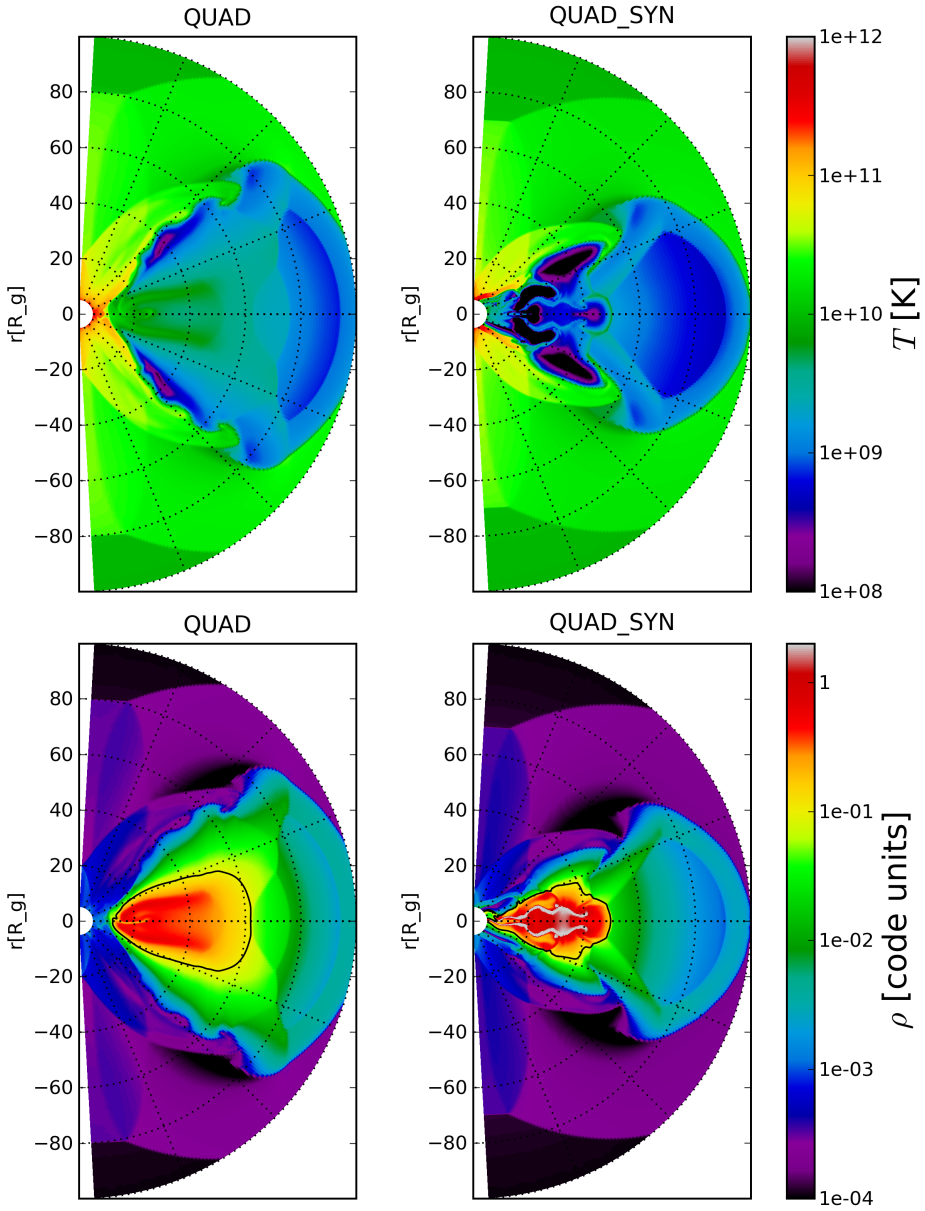

***Figure 4.15* – *Temperature and density for case* `QUAD_SYN`.** *The colour maps show temperature (upper panels) and density (lower panels) in logarithmic scale for case* `QUAD_SYN`*. Case* `QUAD` *is shown on the left hand side for comparison. The snapshots were taken after* 800 lct *when accretion already started in the radiative case but did not in the non radiative case.*

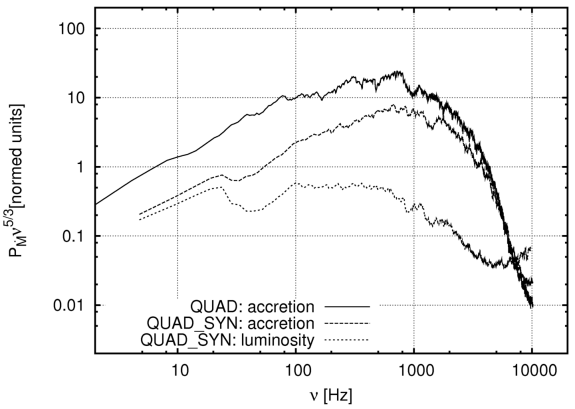

***Figure 4.16** – **Power spectra of accretion and luminosity.** The power spectra of the accretion rate of cases `QUAD` and `QUAD_SYN` and of the integrated synchrotron flux for case `QUAD_SYN` are plotted. The power was multiplied by $\nu^{5/3}$ so that a horizontal spectrum means a decrease with $\nu^{-5/3}$ as predicted in the case of turbulence. The spectra have been smoothed over half an order of magnitude for better readability. Also the steep parts at the beginning and end of the light curve (figure 4.13) have been removed before processing the spectrum as they altered the high frequency part of the spectrum significantly without being of scientific interest.*

the equator which means that different lines of sight will result in different observational features.

The power spectrum of the integrated emission (figure 4.16, short dashed) exhibits a very flat shape over almost 2 orders of magnitude. The decrease towards higher frequencies is less pronounced than in the accretion spectrum. That reflects that not all of the emission comes from the region close to the inner boundary (compare results of case `QUAD` in section 3.3.1). In the emitting regions of the torus the turbulent dynamics of the medium dominates the emission process, in contrast to the inner regions where the orbital revolution is determining dynamics. Thus turbulent motion is present on smaller scales when occurring further away from the black hole. That explains the rather large power of high frequencies in the emission power spectrum.

A surprising result is the absence of continuous winds (figure 4.18). While accretion behaves in almost the same manner as in the non radiating case, winds are totally different. Outflows at the outer boundary only occur episodically (only three events during 4000 lct) and fast winds are even less frequent. There is only one event observed after $\approx$ 2500 lct (figure 4.19). This fast outflow is only present on side of the accretion disc.

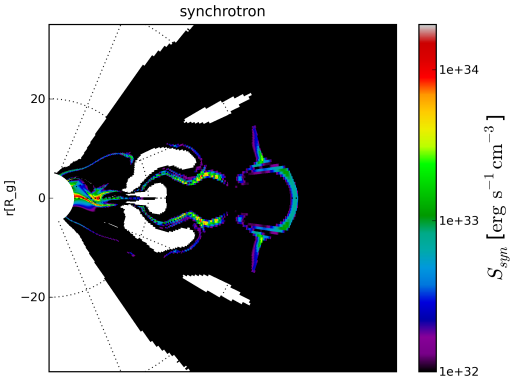

***Figure 4.17** – **Synchrotron emission map of case** `QUAD_SYN`. The plot shows energy loss per time and volume of the inner region of the simulated domain. Black indicates values $< 10^{32}$ while transparent regions do not expose any emission at all due to a vanishing magnetic field. The snapshot was taken after* 800 lct

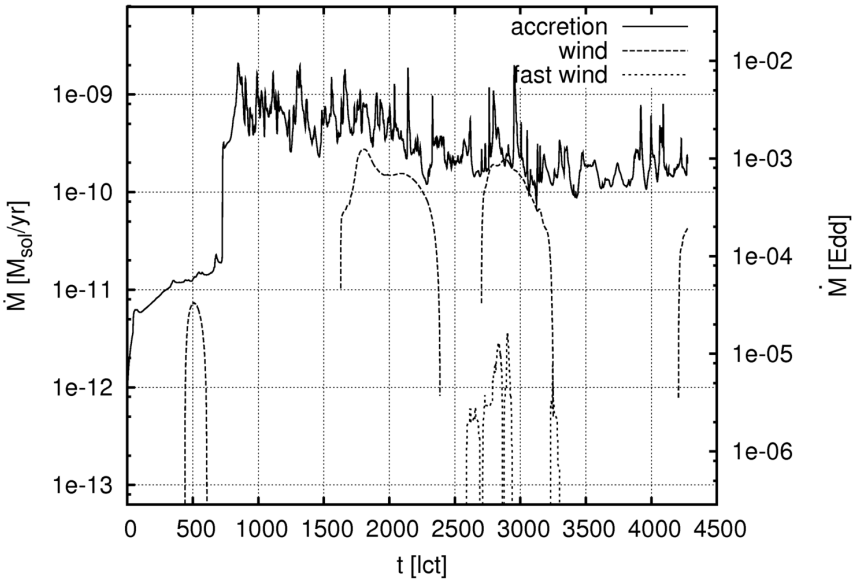

***Figure 4.18** – **Accretion and wind rate for case** `QUAD_SYN`. The plot shows mass fluxes through the inner (accretion) and outer (winds) boundary for case `QUAD_SYN`. For the physical units we assumed $M_{\mathrm{BH}} = 10 M_{\odot}$ and $\rho_{\max} = 10^{-7}\,\mathrm{g/cm^3}$.*

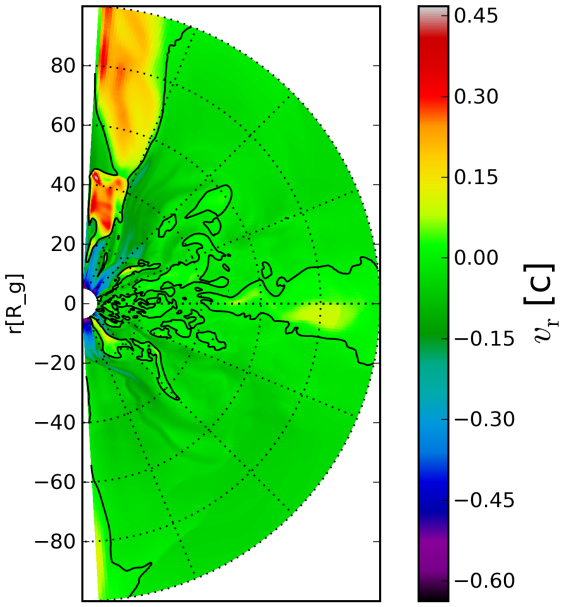

Figure 4.19 – Event of fast jet in case `QUAD_SYN`. *Radial velocity is plotted in linear colours coding. Black contours separate inflow from outflow regions. The plot shows a snapshot after* 2800 lct.

4.5 Discussion

We performed several numerical experiments to sort out the initial parameters of advection dominated accretion discs relevant for the observed features. These are the onset of turbulence in the torus, accretion rates and the ejection of spherical winds and fast jet-like outflows.

Effect of changing position and size of the torus. We altered position and size of the initial torus. The point in time where the accretion rates rise steeply, i.e. the onset of accretion is strongly correlated to the local orbital period at the density maximum. Since the characteristic time scale of MRI is proportional to and of the order of the orbital period, which suggests MRI as the dynamically dominant process in accretion. The formation of slow and fast winds and the onset of turbulence are identical to the model case `QUAD`.

Stronger and weaker magnetic field. In the model case `QUAD` the ratio of gas to magnetic pressure $\beta = 8\pi p_{\mathrm{gas}}/B^2$ is set to average 10^2. The relative magnetic field strength β was varied in order to test its influence on the accretion dynamics.

- `QUAD_BETA3`: For $\beta = 3$ (i.e. less magnetised torus matter) we get a result combining properties of the model case (β=100) and the non magnetised case ($\beta = \infty$):
  - **Accretion** does occur on the equatorial plane as torus matter looses angular momentum *and* spherically from the atmosphere. The accretion rate reaches the quasi-stationary value of case `QUAD` more than 1000 lct later than in the model case. No steep increase of accretion is observed.
  - **Winds** are much less pronounced than in the other cases. Fast winds are not present making accretion from the atmosphere possible, as described previously.

  The fastest growing unstable MRI mode has a wavelength of $\lambda_{\max} \approx 4\,\mathrm{R_g}$ so turbulence induced by MRI is possible in principle. Stronger perturbations than in the non magnetised case are present.

  Hence, fast outflows may be absent even if MRI drives turbulence and accretion is present.

- `QUAD_BETA1.5`: This case is quite similar to the model case `QUAD`. The jet-like outflow appears slower and a little bit more irregular but the differences are within the scope of the intrinsic variations from one orbit to the other for example.

Different magnetic field topologies. The six magnetic set-ups behave very similar. During the first 2000 lct we observed radial channels formed by accreting torus material. In the case of a dipole (`DIP`) there was one channel, in `QUAD` two, in `SEXT` three and so forth. These structures are destroyed soon by the turbulent action in the domain.

Accretion starts stronger and faster when smaller magnetic loops are present. These higher order magnetic fields appear to be more unstable to MRI than larger loops. A possible reason is that the loops, acting as seed perturbations are of the size of the fastest growing wavelength in the cases `OCT`, `MULT` and `QUAD_MULT` while the dipole loop in `DIP` is somewhat larger.

Influence of radiative cooling. Cooling has a strong effect on the accreting torus. It cools the torus matter down to less than 10^8 K. In the non cooled model case `QUAD` it remains around 10^{10} K. This causes the inner parts of the torus to contract. Density rises by a factor of a few while the vertical and radial extension of the torus decreases.

As accretion starts, the fluctuations are not as pronounced an in case `QUAD`. Integrating the synchrotron emission over the whole domain and comparing the achieved light curve the accretion rate one notes that an event of enhanced accretion is always preceded by a small rise in the light curve. This

is due to the fact that most of the synchrotron radiation is emitted close to the horizon of the black hole where the density is high and magnetic fields are strong.

Nevertheless the power spectra of accretion and luminosity indicate that emission is subject to faster variations than accretion. This reflects that the emission is also determined by the turbulence in the torus and not only by the dynamical time scales at the inner boundary as the accretion rate.

Outflows are suppressed strongly by the cooling mechanism. Slow occur occasionally but do not reach the same rates as in the non radiative case. Fast collimated outflows are even more scarce. Only one weak event was observed during 4200 lct of simulated time.

The fact that major differences exist between the results of non radiative simulations (case `QUAD`) and radiatively inefficient simulations (case `QUAD_SYN`) indicates that post-processing the data in order to obtain information about the radiative properties of the disc (e.g. Goldston *et al.*, 2005) will give unreliable results.

Ja und nein und beides nicht,
so wie Du es meinst.

— Das Südliche Orakel

5 Summary and conclusions

We performed spherical axisymmetric (2.5D) and 3-dimensional simulations of advection dominated accretion flows (ADAF). The applied code, PLUTO3.01, solves the equations of ideal magnetohydrodynamics using a conservative scheme based on the Harten-Lax-van Leer solver. Gravity was included as a pseudo Newtonian potential emulating a non rotating black hole.

These investigations can be applied to accreting black hole systems such as AGN and X-ray binaries. All set-ups except for the one including radiative cooling can be scaled to any black hole mass and initial torus density due to the absence of microscopic terms in the solved equations.

We investigated the influence of several modifications in the initial set-up: (1) the size and position of the torus (2) the strength and (3) the geometry of the magnetic field and (4) adding a synchrotron loss term to the energy equation. In doing so we attempt to get closer to realistic simulations ruling out the effects of too artificial, idealised set-ups.

The model case and basis for comparison was the case `QUAD`. It consisted of a torus with its density maximum at $30\,\mathrm{R_g}$. The magnetic field was initialised as a poloidal quadrupole field.

Set-up and hydrodynamic stability. The torus was set up to lie in the potential well of a effective potential, which is the sum of the gravitational potential and the potential arising from the Keplerian angular momentum of the matter. The torus rotated with its local Keplerian orbital period; the atmosphere was not rotating. The velocity field was perturbed with random noise of an amplitude of $0.01\,\mathrm{c}$ throughout the whole domain.

The set-up was proven to be hydrodynamically stable over the simulated time of 10^4 lct which corresponds to 10 orbits at the density maximum. In the absence of a magnetic field the torus remained at its original position being only perturbed a little bit on its surface. We explained these perturbation by friction with the non rotating atmosphere and as reactions to the initial random noise which has been added to the initial velocity field.

Accretion happens also in the hydrodynamic case. But instead of building up a quiet narrow accretion flow close to the equator of the disc, matter was falling in spherically from the atmosphere. A constant mass flow forms, only perturbed by the presence of the torus. This was in good agreement to the Bondi solution of spherical accretion.

Accretion. We found accretion in the magnetised case to start within approximately one orbital period at the density maximum. It reached a quasi stationary level instantly after the onset of accretion. The accretion rate corresponded to $10^9\,\mathrm{M}_\odot/\mathrm{yr}$ for a black hole of $10\,\mathrm{M}_\odot$ and an initial maximum density of $10^{-7}\,\mathrm{g/cm}^3$ or $0.1\,\dot{\mathrm{M}}_{\mathrm{Edd}}$, assuming an accretion efficiency of 10%.

The characteristic timescale of the accretion was verified with simulations in which the torus resides at different radii. Since the local orbital period was the characteristic timescale for MRI, this gives a strong argument in favour of MRI being the cause for the accretion.

The power of accretion was also influenced by the ratio of gas pressure to magnetic pressure (β) and the geometry of the magnetic field. For larger values of β accretion lasts longer to evolve but reaches the same value finally. In the case of smaller magnetic loops in the initial torus we found a faster onset of accretion.

Other differences in the structure of the accretion flow or its surroundings were soon smeared by the turbulent motion of the fluid.

Outflows. Two types of outflows were observed:

1. **Slow dense winds:** Torus matter was streaming spherically into the atmosphere from the surface of the torus except for its inner cusp. The velocity of this displacement was much smaller than the dynamical velocity of the torus. The atmosphere was filled partly with matter about twice as dense as the atmospheric value. Angular momentum was carried away mainly by this wind.

2. **Fast tenuous jet-like outflows:** Within an angle of 20° around the axis of rotation a fast outflow formed with a velocity of up to $0.6\,\mathrm{c}$. This velocity is in excellent agreement with observations of microquasar jets. The density in this outflow region equalled the numerical floor value. The Alfvén speed reached the speed of light. Due to the opening angle

of $\approx 40°$ and the velocity significantly smaller than the speed of light, it could not be interpreted as a *jet*. Nevertheless it might be the seed of one getting accelerated and collimated further outwards and/or by general relativistic effects of the rotation of the black hole not included in the simulations presented here.

The slow coronal wind formed in every tested set-up. Two configuration lacked a fast jet-like outflow:

- The less magnetised torus of case `QUAD_BETA3`: This case could give a hint at the answer of two unresolved questions in astrophysics:
  1. *What is the nature of the radio quiet quasars?* Since the main source of radio emission in quasars is assumed to have its origin in the jet, the question can be reworded to: *Why do some quasars not have jets?* The answer we proposed on the base of the test performed here is: Because matter is not magnetised enough to eject them.
  2. *Why do X-ray binaries have outbursts when passing from the hard to the soft state?* The hard state consists of a weakly magnetised ADAF, which has no jet or a very weak one. Synchrotron emission is produced by the dense hot parts of the torus and hardened via inverse Comptonisation. Thereafter high density matter is falling in from outer regions. This matter radiates the soft spectrum of a multi coloured black body. Before it replaces the ADAF totally, the inner thin gas of the ADAF is confronted with the piled up magnetic field from the denser outer matter. During this phase a fast jet can be produced as there is an abundance of magnetic energy striking low density matter. This configuration also favours the emission of synchrotron radiation which will rise for a short period before matter has cooled down and becomes optically thick due to the arriving infalling matter from further out.

- The cooled case including synchrotron emission `QUAD_SYN`:

  The absence of a fast outflow in the simulations including synchrotron cooling posed a more difficult problem to interpret. We assumed that configurations can be found which incorporate cooling *and* result in the ejection of jets. Further work is required here. At this point we can however state definitely that processing spectra, light curves and alike *after* simulating without taking into account radiative losses even from optically thin discs (e.g. Goldston *et al.*, 2005) will lead to unreliable results.

Retrograde rotation of the jet. In the fast outflows recurring events of counter-rotation, i.e. rotation in the opposite direction as the disc, were found. These occurred with an approximate mean frequency of 200 Hz and propagated outwards with the speed and in the direction of the fast outflow. We explained this counter-rotation by the interaction of the shearing term in the induction equation $R\,\mathbf{B}_\mathrm{p}\cdot\nabla\Omega$ and the dependence of angular momentum transport on the Maxwell stress $B_\phi\boldsymbol{\delta}\mathbf{B}_\mathrm{p}/4\pi\rho$. Bended magnetic field lines will seek relaxation. In the jet this can be achieved in the direction of the disc rotation as well as in the contrary direction. The direction seems to alternate periodically dragging along the jet matter. As the density is very low in the fast outflow, the magnetic field dominates the dynamics which leads to the observed counter-rotation.

This phenomenon can be interpreted as an *extreme zonal flow*, a 'low β version' of the zonal flows described by Johansen *et al.* (2009), who found zones of deviant rotation speed in shearing box simulations.

Unfortunately this rotation can not be observed easily in black hole jets. They do not exhibit line emission which would enable observers to test known jets for rotational motion.

By contrast, YSO-jets show line emissions which enable the measurement of intrinsic relative movement such as rotation. In spite of the differences between YSO jets and black hole jets, the process of ejection may be quite similar (Camenzind, 1990). Both require an at least partially ionised accretion disc what indicates a coupling to the magnetic fields in the disc in either case. Coffey *et al.* (2004, 2007) and Woitas *et al.* (2005) have carried out spectroscopic observations using the *Hubble space telescope imaging spectrograph* (HST/STIS) of the jets of TH28, RW Aur, LkHα 321, DG Tau, CW Tau and HH 30. They interpreted asymmetries found in the measured velocities as an indication for rotation of the jet. Our simulations affirmed the assumption that rotation is present in jets. Also retrograde rotation as found by Cabrit *et al.* (2006) in RW Aur could be caused by the mechanism we described. Arguments against the interpretation of the velocity profiles as a sign of rotation as put forth by Soker (2007) have to be revised considering the results presented here.

Look on, look on, look on!

— John Frusciante

6 Outlook

During the progress of this work we found that some initial properties of a simulation set-up are crucial for the further development of the disc and its outflows while others do not have any effect or the effect is cancelled by the turbulent evolution of the disc. In future works we will focus on the properties that *do* alter the disc dynamics durably. The following points require further detailed studies:

- The dependence on the strength of the magnetic field: Radial changes of the magnetisation could lead to a dynamic triggering of the fast jet-like outflow. Also the launching of jets in the case of very strong magnetic fields ($\beta \leq 10$) could give further insight into the switching between the low-hard and the high-soft state observed in X-ray binaries.

- The durability of the retrograde rotation of the jet: The exact mechanism leading to this unexpected feature remains unclear. Both analytical and numerical work is required to solve this problem.

- The absence of a jet-like outflow when including radiative losses in the simulations: Altering the magnetic field strength and other parameters could make the launching of a jet possible even in radiative simulations.

In a way, this work is also a collection of hints for future projects as every answer yields several questions.

A

Symbols and Constants

Symbols and constants used in this work are listed and explained below. They apply as far as no differing meaning is given in the text. Bold symbols ($\mathbf{v}$) describe vectors, cursive symbols scalars (v).

Table A.1 *– Symbols*

symbol	**meaning**	**cgs (Gaussian)**	**MKSA**
$l,\ h$	length, height	cm	10^{-2} m
λ	wavelength		
r	spherical radius		
R	cylindrical radius		
R_g	gravitational radius (GM/c^2)		
R_S	Schwarzschild radius ($2GM/c^2$)		
$m,\ M$	mass	g	10^{-3} kg
t	time	s	s
lct	light crossing time (GM/c^3)		
ρ	mass density	$\mathrm{g/cm^3}$	$10^3\ \mathrm{kg/m^3}$
Ω	angular frequency of a rotation	$\mathrm{1/s}$	$\mathrm{1/s}$
ω	angular frequency of a perturbation		
κ	epicyclic angular frequency		

continued on the next page...

symbol	meaning	cgs (Gaussian)	MKSA
$\mathbf{v}$, v	velocity	$^{\mathrm{m}}/_{\mathrm{s}}$	$10^{-2}\,^{\mathrm{m}}/_{\mathrm{s}}$
c_{s}	speed of sound		
$\mathbf{v_A}$	Alfvén velocity		
L	specific angular momentum	$^{\mathrm{cm}^2}/_{\mathrm{s}}$	$10^{-4}\,^{\mathrm{m}^2}/_{\mathrm{s}}$
g	gravitative acceleration	$^{\mathrm{cm}}/_{\mathrm{s}}$	$10^{-2}\,^{\mathrm{m}}/_{\mathrm{s}^2}$
p	gas pressure	ba	$0.1\,\mathrm{Pa} = 0.1\,^{\mathrm{kg}}/_{\mathrm{m\,s}^2}$
p_{mag}	magnetic pressure		
$\mathbf{E}, E_\alpha$	electric field	$^{\mathrm{statV}}/_{\mathrm{cm}}$	$2.99792458 \cdot 10^4\,^{\mathrm{V}}/_{\mathrm{m}}$
J	total current density	$^{\mathrm{esu}}/_{\mathrm{s}}$	$3.33564 \cdot 10^{-}10\,\mathrm{A}$
q	electric charge	esu	$3.33564 \cdot 10^{-}10\,\mathrm{C}$
E	energy	$\mathrm{erg} = {}^{\mathrm{gcm}^2}/_{\mathrm{s}^2}$	$10^{-7}\,\mathrm{J} = 10^{-7}\,^{\mathrm{kg\,m}^2}/_{\mathrm{s}^2}$
ϵ	internal energy		
$\mathcal{E}$	specific internal energy	$^{\mathrm{erg}}/_{\mathrm{g}}$	$10^{-4}\,^{\mathrm{J}}/_{\mathrm{kg}}$
e	energy density	$^{\mathrm{erg}}/_{\mathrm{cm}^3}$	$10^{-1}\,^{\mathrm{J}}/_{\mathrm{m}^3}$
S	source/sink of energy density	$^{\mathrm{erg}}/_{\mathrm{s\,m}^3}$	$10^{-1}\,^{\mathrm{J}}/_{\mathrm{s\,m}^3}$
P	power	$^{\mathrm{erg}}/_{\mathrm{s}}$	$10{-}7\,^{\mathrm{J}}/_{\mathrm{s}}$
$\mathcal{L}$	luminosity		
Φ	gravitational potential	$^{\mathrm{erg}}/_{\mathrm{g}}$	$10^{-4}\,^{\mathrm{J}}/_{\mathrm{kg}}$
$\mathbf{B}$	magnetic flux density	G	$10^{-4}\,\mathrm{T} = 10^{-4}\,^{\mathrm{kg}}/_{\mathrm{A\,s}^2}$

Table A.2 – *Constants*

Constant	Meaning	cgs (Gaussian)	MKSA
G	gravitational constant	$6.67259 \cdot 10^{-8}\,^{\mathrm{cm}^3}/_{\mathrm{g\,s}^2}$	$6.67259 \cdot 10^{-11}\,^{\mathrm{m}^3}/_{\mathrm{kg\,s}^2}$
c	speed of light in vacuum	$2.99792458 \cdot 10^{10}\,^{\mathrm{cm}}/_{\mathrm{s}}$	$2.99792458 \cdot 10^8\,^{\mathrm{m}}/_{\mathrm{s}}$
μ_0	magnetic permeability	$4\,\pi$	$4\,\pi \cdot 10^{-7}\ \frac{\mathrm{H}}{\mathrm{m}}\ \left[\hat{=}\frac{\mathrm{kg\,m}}{\mathrm{A}^2\mathrm{s}^2}\right]$
$M_\odot$	solar mass	$1.989 \cdot 10^{33}\,\mathrm{g}$	$1.989 \cdot 10^{30}\,\mathrm{kg}$
$\mathcal{R}$	universal gas constant	$8.31447 \cdot 10^7\,^{\mathrm{erg}}/_{\mathrm{K\,mol}}$	$8.31447\,^{\mathrm{J}}/_{\mathrm{K\,mol}}$
σ_{T}	Thompson cross section $(\frac{8\pi e^4}{3c^4 m_{\mathrm{e}}^2})$	$6.6524 \cdot 10^{-25}\,\mathrm{cm}^2$	$6.6524 \cdot 10^{-29}\,\mathrm{m}^2$

B
Useful equations

Some useful relations used in the main text that do not appear in most collections are listed below. It is not intended to give a complete list as there are numerous text books doing so (a good formulary is Diver (2001)).

Please note that in this chapter, f and g are arbitrary scalars and $\mathbf{u}$, $\mathbf{v}$ and $\mathbf{w}$ are arbitrary 3-dimensional vectors.

$$\mathbf{u} \otimes \mathbf{v} = \begin{pmatrix} u_1 v_1 & u_1 v_2 & u_1 v_3 \\ u_2 v_1 & u_2 v_2 & u_2 v_3 \\ u_3 v_1 & u_3 v_2 & u_3 v_3 \end{pmatrix} \tag{B.1}$$

$$\mathbf{u} \times (\mathbf{v} \times \mathbf{w}) = \mathbf{v}(\mathbf{u} \cdot \mathbf{w}) - \mathbf{w}(\mathbf{u} \cdot \mathbf{v}) \tag{B.2}$$

with the use of $\partial_t \rho = \nabla \cdot (\rho \mathbf{v})$:

$$\rho(\partial_t \frac{f}{\rho} + (\mathbf{v} \cdot \nabla)\frac{f}{\rho}) = \partial_t f + \nabla \cdot (f\mathbf{v}) \tag{B.3}$$

$$\nabla \cdot (\mathbf{u} \otimes \mathbf{v}) = (\nabla \cdot \mathbf{u})\mathbf{v} + (\mathbf{u} \cdot \nabla)\mathbf{v} \tag{B.4}$$

$$\nabla \cdot (\mathbf{v} \otimes \mathbf{u} - \mathbf{u} \otimes \mathbf{v}) = \nabla \times (\mathbf{u} \times \mathbf{v}) \tag{B.5}$$

References

M. Abramowitz and I. A. Stegun. *Handbook of Mathematical Functions*. New York: Dover, 1972, 1972.

H. Alfvén. On the cosmogony of the solar system. *Stockholms Observatoriums Annaler*, 14:2–+, 1942.

A. M. Anile. *Relativistic Fluids and Magneto-fluids*. Cambridge University Press, February 1990.

J. Arons. Photon bubbles - Overstability in a magnetized atmosphere. *ApJ*, 388:561–578, April 1992.

S. A. Balbus and J. F. Hawley. A powerful local shear instability in weakly magnetized disks. I - Linear analysis. II - Nonlinear evolution. *ApJ*, 376:214–233, July 1991.

S. A. Balbus and J. F. Hawley. Instability, turbulence, and enhanced transport in accretion disks. *Reviews of Modern Physics*, 70:1–53, January 1998.

S. A. Balbus. Turbulent Energy Transport in Nonradiative Accretion Flows. *ApJ*, 600:865–871, January 2004.

D. S. Balsara and D. S. Spicer. A Staggered Mesh Algorithm Using High Order Godunov Fluxes to Ensure Solenoidal Magnetic Fields in Magnetohydrodynamic Simulations. *Journal of Computational Physics*, 149:270–292, March 1999.

K. Beckwith, J. F. Hawley, and J. H. Krolik. The Influence of Magnetic Field Geometry on the Evolution of Black Hole Accretion Flows: Similar Disks, Drastically Different Jets. *ApJ*, 678:1180–1199, May 2008.

M. C. Begelman. Toward a unified theory of active galactic nuclei. *New York Academy Sciences Annals*, 470:51–70, 1986.

H. A. Bethe and C. L. Critchfield. The Formation of Deuterons by Proton Combination. *Physical Review*, 54:248–254, August 1938.

D. Biskamp. *Nonlinear Magnetohydrodynamics*. Nonlinear Magnetohydrodynamics, ISBN 0521599180, Cambridge University Press, Paperback, 1997., 1997.

R. D. Blandford and D. G. Payne. Hydromagnetic flows from accretion discs and the production of radio jets. *MNRAS*, 199:883–903, June 1982.

R. D. Blandford and R. L. Znajek. Electromagnetic extraction of energy from Kerr black holes. *MNRAS*, 179:433–456, May 1977.

G. Bodo, A. Mignone, F. Cattaneo, P. Rossi, and A. Ferrari. Aspect ratio dependence in magnetorotational instability shearing box simulations. *A&A*, 487:1–5, August 2008.

H. Bondi. On spherically symmetrical accretion. *MNRAS*, 112:195–+, 1952.

S. Brinkmann, M. Camenzind, and J. Gracia. Global structure of non-radiative and radiative accretion discs. *submitted to A&A*, -:–, 2008.

S. Brinkmann, M. Camenzind, and J. Gracia. Rotation structure and oscillation of accretion discs and their outflows. *submitted to A&A*, -:–, 2008.

S. Brinkmann. MHD-Instabilities in accretion discs: Simulation and analysis of the MRI. Master's thesis, Universität Heidelberg, 2004.

S. Cabrit, J. Pety, N. Pesenti, and C. Dougados. Tidal stripping and disk kinematics in the RW Aurigae system. *A&A*, 452:897–906, June 2006.

M. Camenzind. Magnetized Disk-Winds and the Origin of Bipolar Outflows. In G. Klare, editor, *Reviews in Modern Astronomy*, volume 3 of *Reviews in Modern Astronomy*, pages 234–265, 1990.

F. Casse. Vertical angular momentum transfer from accretion discs and the formation of large-scale collimated jets. *Plasma Physics and Controlled Fusion*, 50(12):124020–+, December 2008.

S. Chandrasekhar. The Stability of Non-Dissipative Couette Flow in Hydromagnetics. *Proceedings of the National Academy of Science*, 46:253–257, February 1960.

S. Chandrasekhar. *Hydrodynamic and hydromagnetic stability*. International Series of Monographs on Physics, Oxford: Clarendon, 1961.

D. Coffey, F. Bacciotti, J. Woitas, T. P. Ray, and J. Eislöffel. Rotation of Jets from Young Stars: New Clues from the Hubble Space Telescope Imaging Spectrograph. *ApJ*, 604:758–765, April 2004.

D. Coffey, F. Bacciotti, T. P. Ray, J. Eislöffel, and J. Woitas. Further Indications of Jet Rotation in New Ultraviolet and Optical Hubble Space Telescope STIS Spectra. *ApJ*, 663:350–364, July 2007.

J.-P. De Villiers and J. F. Hawley. Global General Relativistic Magnetohydrodynamic Simulations of Accretion Tori. *ApJ*, 592:1060–1077, August 2003.

A. Dedner, F. Kemm, D. Kröner, C.-D. Munz, T. Schnitzer, and M. Wesenberg. Hyperbolic Divergence Cleaning for the MHD Equations. *Journal of Computational Physics*, 175:645–673, January 2002.

L. Del Zanna, N. Bucciantini, and P. Londrillo. An efficient shock-capturing central-type scheme for multidimensional relativistic flows. II. Magnetohydrodynamics. *A&A*, 400:397–413, March 2003.

R. Descartes. *Le Monde, ou Traité de la Lumière*. 1664.

D. A. Diver. *A plasma formulary for physics, technology, and astrophysics*. A plasma formulary for physics, technology, and astrophysics by Declan A. Diver. Berlin ; New York : Wiley-VCH, c2001. ISBN : 3527402942, 2001.

W. G. Dixon. *Special relativity: the foundation of macroscopic physics*. Cambridge Univ. Press, 1978.

A. Dubey, L. B. Reid, K. Weide, K. Antypas, M. K. Ganapathy, K. Riley, D. Sheeler, and A. Siegal. Extensible Component Based Architecture for FLASH, A Massively Parallel, Multiphysics Simulation Code. *ArXiv e-prints*, March 2009.

A. S. Eddington. A limiting case in the theory of radiative equilibrium. *MNRAS*, 85:408–+, March 1925.

B. L. Fanaroff and J. M. Riley. The morphology of extragalactic radio sources of high and low luminosity. *MNRAS*, 167:31P–36P, May 1974.

R. P. Fender, T. M. Belloni, and E. Gallo. Towards a unified model for black hole X-ray binary jets. *MNRAS*, 355:1105–1118, December 2004.

M. Flaig, R. Kissmann, and W. Kley. Growth of the MRI in accretion discs - the influence of radiation transport. *MNRAS*, 394:1887–1896, April 2009.

M. Flock. —. Master's thesis, MPIA, Heidelberg, 2008.

P. C. Fragile, O. M. Blaes, P. Anninos, and J. D. Salmonson. Global General Relativistic Magnetohydrodynamic Simulation of a Tilted Black Hole Accretion Disk. *ApJ*, 668:417–429, October 2007.

J. Frank, A. R. King, and D. J. Raine. *Accretion Power in Astrophysics*. Cambridge University Press, 1985.

G. Galilei. *Discorsi*. 1638.

R. Giacconi, H. Gursky, F. R. Paolini, and B. B. Rossi. Evidence for x Rays From Sources Outside the Solar System. *Physical Review Letters*, 9:439–443, December 1962.

J. E. Goldston, E. Quataert, and I. V. Igumenshchev. Synchrotron Radiation from Radiatively Inefficient Accretion Flow Simulations: Applications to Sagittarius A*. *ApJ*, 621:785–792, March 2005.

J. Goodman and G. Xu. Parasitic instabilities in magnetized, differentially rotating disks. *ApJ*, 432:213–223, September 1994.

J. Gracia, J. Peitz, C. Keller, and M. Camenzind. Evolution of bimodal accretion flows. *MNRAS*, 344:468–472, September 2003.

L. Hartmann, N. Calvet, E. Gullbring, and P. D'Alessio. Accretion and the Evolutiion of T Tauri Disks. *ApJ*, 495:385–+, March 1998.

E. Hatziminaoglou, J. Fritz, A. Franceschini, A. Afonso-Luis, A. Hernán-Caballero, I. Pérez-Fournon, S. Serjeant, C. Lonsdale, S. Oliver, M. Rowan-Robinson, D. Shupe, H. E. Smith, and J. Surace. Properties of dusty tori in active galactic nuclei - I. The case of SWIRE/SDSS quasars. *MNRAS*, 386:1252–1264, May 2008.

J. F. Hawley and S. A. Balbus. A powerful local shear instability in weakly magnetized disks. III - Long-term evolution in a shearing sheet. IV - Non-axisymmetric perturbations. *ApJ*, 400:595–621, December 1992.

J. F. Hawley, K. Beckwith, and J. H. Krolik. General relativistic MHD simulations of black hole accretion disks and jets. *Astrophysics and Space Science*, 311:117–125, October 2007.

J. C. Hayes, M. L. Norman, R. A. Fiedler, J. O. Bordner, P. S. Li, S. E. Clark, A. ud-Doula, and M.-M. Mac Low. Simulating Radiating and Magnetized Flows in Multiple Dimensions with ZEUS-MP. *ApJS*, 165:188–228, July 2006.

I. V. Igumenshchev, X. Chen, and M. A. Abramowicz. Accretion discs around black holes: two-dimensional, advection-cooled flows. *MNRAS*, 278:236–250, January 1996.

I. V. Igumenshchev, R. Narayan, and M. A. Abramowicz. Three-dimensional Magnetohydrodynamic Simulations of Radiatively Inefficient Accretion Flows. *ApJ*, 592:1042–1059, August 2003.

J. D. Jackson. *Classical electrodynamics*. 92/12/31, New York: Wiley, 1975, 2nd ed., 1975.

A. Johansen, A. Youdin, and H. Klahr. Zonal Flows and Long-lived Axisymmetric Pressure Bumps in Magnetorotational Turbulence. *ApJ*, 697:1269–1289, June 2009.

I. Kant. *Allgemeine Naturgeschichte und Theorie des Himmels*. 1755.

J. Kepler. *Astronomia Nova*. 1609.

J. Kepler. *Harmonices Mundi*. 1619.

H. Klahr and W. Kley. 3D-radiation hydro simulations of disk-planet interactions. I. Numerical algorithm and test cases. *A&A*, 445:747–758, January 2006.

G. P. Kuiper. On the Interpretation of β Lyrae and Other Close Binaries. *ApJ*, 93:133–+, January 1941.

A. Lawrence. Classification of active galaxies and the prospect of a unified phenomenology. *Publications of the Astronomical Society of the Pacific*, 99:309–334, May 1987.

R. J. LeVeque . *Finite Volume Methods for Hyperbolic Problems*. Cambridge University Press, 2002.

D. N. C. Lin and J. E. Pringle. Numerical Simulation of Mass Transfer and Accretion Disc Flow in Binary Systems. In P. Eggleton, S. Mitton, and J. Whelan, editors, *Structure and Evolution of Close Binary Systems*, volume 73 of *IAU Symposium*, pages 237–+, 1976.

R. Lüst. Die Entwicklung einer um einen Zentralkörper rotierenden Gasmasse. I. Lösungen der hydrodynamischen Gleichungen mit turbulenter Reibung. *Zeitschrift für Naturforschung*, 7a:87–98, 1952.

J. C. McKinney and R. D. Blandford. Stability of relativistic jets from rotating, accreting black holes via fully three-dimensional magnetohydrodynamic simulations. *MNRAS*, 394:L126–L130, March 2009.

J. C. McKinney and C. F. Gammie. A Measurement of the Electromagnetic Luminosity of a Kerr Black Hole. *ApJ*, 611:977–995, August 2004.

J. C. McKinney. General relativistic magnetohydrodynamic simulations of the jet formation and large-scale propagation from black hole accretion systems. *MNRAS*, 368:1561–1582, June 2006.

A. Mignone, G. Bodo, S. Massaglia, T. Matsakos, O. Tesileanu, C. Zanni, and A. Ferrari. PLUTO: A Numerical Code for Computational Astrophysics. *ApJS*, 170:228–242, May 2007.

A. Mignone, M. Ugliano, and G. Bodo. A five-wave Harten-Lax-van Leer Riemann solver for relativistic magnetohydrodynamics. *MNRAS*, pages 114–+, February 2009.

A. B. Mikhailovskii, J. G. Lominadze, R. M. O. Galva˜O, A. P. Churikov, O. A. Kharshiladze, N. N. Erokhin, and C. H. S. Amador. Nonlocal magnetorotational instability. *Physics of Plasmas*, 15(5):052109–+, May 2008.

A. Müller. *Black hole astrophysics: magnetohydrodynamics on the Kerr geometry*. PhD thesis, PhD Thesis, Combined Faculties for the Natural Sciences and for Mathematics of the University of Heidelberg, Germany. VI + 129 + XXXVIII pp. (2004), December 2004.

J. Muzerolle, K. L. Luhman, C. Briceño, L. Hartmann, and N. Calvet. Measuring Accretion in Young Substellar Objects: Approaching the Planetary Mass Regime. *ApJ*, 625:906–912, June 2005.

M. Oda. CYG X-1 - A candidate of the black hole. *Space Science Reviews*, 20:757–813, September 1977.

B. Paczynsky and P. J. Wiita. Thick accretion disks and supercritical luminosities. *A&A*, 88:23–31, August 1980.

J. C. B. Papaloizou and J. E. Pringle. The time-dependence of non-planar accretion discs. *MNRAS*, 202:1181–1194, March 1983.

K. G. Powell, P. L. Roe, T. J. Linde, T. I. Gombosi, and D. L. de Zeeuw. A Solution-Adaptive Upwind Scheme for Ideal Magnetohydrodynamics. *Journal of Computational Physics*, 154:284–309, September 1999.

R. A. Remillard and J. E. McClintock. X-Ray Properties of Black-Hole Binaries. *Annual Review of Astronomy and Astrophysics*, 44:49–92, September 2006.

M. M. Romanova, A. K. Kulkarni, and R. V. E. Lovelace. Unstable Disk Accretion onto Magnetized Stars: First Global Three-dimensional Magnetohydrodynamic Simulations. *ApJ*, 673:L171–L174, February 2008.

G. Rüdiger, R. Hollerbach, F. Stefani, T. Gundrum, G. Gerbeth, and R. Rosner. The Traveling-Wave MRI in Cylindrical Taylor-Couette Flow: Comparing Wavelengths and Speeds in Theory and Experiment. *ApJ*, 649:L145–L147, October 2006.

G. B. Rybicki and A. P. Lightman. *Radiative processes in astrophysics*. New York, Wiley-Interscience, 1979. 393 p., 1979.

E. E. Salpeter. Accretion of Interstellar Matter by Massive Objects. *ApJ*, 140:796–800, August 1964.

M. Schmidt. 3C 273 : A Star-Like Object with Large Red-Shift. *Nature*, 197:1040–+, March 1963.

N. I. Shakura and R. A. Sunyaev. Black holes in binary systems. Observational appearance. *A&A*, 24:337–355, 1973.

S. L. Shapiro and S. A. Teukolsky. *Black Holes, White Dwarfs and Neutron Stars, The physics of compact objects*. John Wiley & sons, 1983.

I. S. Shklovskii. The Nature of the X-Ray Source Sco X-1. *Astronomicheskii Zhurnal*, 44:930–+, 1967.

F. H. Shu. *Physics of Astrophysics, Vol. I.* Physics of Astrophysics, Vol. I, by Frank H. Shu. Published by University Science Books, ISBN 0-935702-64-4, 429pp, 1991., 1991.

S.-A. Sørensen, T. Matsuda, and T. Sakurai. Computer simulations of gas flow around close binary systems. *Astrophysics and Space Science*, 33:465–480, April 1975.

N. Soker. Further Indications Against Jet Rotation in Young Stellar Objects. *ArXiv Astrophysics e-prints*, astro-ph/0703474, March 2007.

S. Soldi, M. Türler, S. Paltani, H. D. Aller, M. F. Aller, G. Burki, M. Chernyakova, A. Lähteenmäki, I. M. McHardy, E. I. Robson, R. Staubert, M. Tornikoski, R. Walter, and T. J.-L. Courvoisier. The multiwavelength variability of 3C 273. *A&A*, 486:411–425, August 2008.

A. M. Stirling, R. E. Spencer, C. J. de la Force, M. A. Garrett, R. P. Fender, and R. N. Ogley. A relativistic jet from Cygnus X-1 in the low/hard X-ray state. *MNRAS*, 327:1273–1278, November 2001.

J. M. Stone, T. A. Gardiner, P. Teuben, J. F. Hawley, and J. B. Simon. Athena: A New Code for Astrophysical MHD. *ApJS*, 178:137–177, September 2008.

E. F. Toro. Computational Methods for Hyperbolic Equations. In S. Massaglia, G. Bodo, A. Mignone, and P. Rossi, editors, *Lecture Notes in Physics, Berlin Springer Verlag*, volume 754 of *Lecture Notes in Physics, Berlin Springer Verlag*, pages 3–69, 2008.

E. F. Toro. *Riemann Solvers and Numerical Methods for Fluid Dynamics: A Practical Introduction*. Springer-Verlag Berlin and Heidelberg, 2nd edition, 2009.

N. J. Turner, J. M. Stone, J. H. Krolik, and T. Sano. Local Three-dimensional Simulations of Magnetorotational Instability in Radiation-dominated Accretion Disks. *ApJ*, 593:992–1006, August 2003.

N. J. Turner, O. M. Blaes, A. Socrates, M. C. Begelman, and S. W. Davis. The Effects of Photon Bubble Instability in Radiation-dominated Accretion Disks. *ApJ*, 624:267–288, May 2005.

Y. Uchiyama, C. M. Urry, C. C. Cheung, S. Jester, J. Van Duyne, P. Coppi, R. M. Sambruna, T. Takahashi, F. Tavecchio, and L. Maraschi. Shedding New Light on the 3C 273 Jet with the Spitzer Space Telescope. *ApJ*, 648:910–921, September 2006.

M.-H. Ulrich. 3C 273 - A review of recent results. *Space Science Reviews*, 28:89–104, March 1981.

C. M. Urry and P. Padovani. Unified Schemes for Radio-Loud Active Galactic Nuclei. *Publications of the Astronomical Society of the Pacific*, 107:803–+, September 1995.

M. van der Klis. Millisecond Oscillations in X-ray Binaries. *Annual Review of Astronomy and Astrophysics*, 38:717–760, 2000.

M. van der Klis. The QPO phenomenon. *Astronomische Nachrichten*, 326:798–803, November 2005.

E. P. Velikhov. Stability of an Ideally Conducting Liquid Flowing Between Cylinders Rotating in a Magnetic Field. *Sov. Phys. JETP*, 36:1398–1404, 1959.

H von Helmholtz. *Vorträge und Reden*, volume 1, chapter Ueber die Wechselwirkung der Naturkräfte und die darauf bezüglichen neuesten Ermittelungen der Physik, pages 48–83. Friedrich Vieweg und Sohn, 4th edition, 1896.

C. F. von Weizsäcker. Über die Entstehung des Planetensystems. *Zeitschrift für Astrophysik*, 22:319–355, 1943.

C. F. von Weizsäcker. Die Rotation kosmischer Gasmassen. *Zeitschrift für Naturforschung*, 3a:524–539, 1948.

G. Wardziński and A. A. Zdziarski. Thermal synchrotron radiation and its Comptonization in compact X-ray sources. *MNRAS*, 314:183–198, May 2000.

J. Woitas, F. Bacciotti, T. P. Ray, A. Marconi, D. Coffey, and J. Eislöffel. Jet rotation: Launching region, angular momentum balance and magnetic properties in the bipolar outflow from RW Aur. *A&A*, 432:149–160, March 2005.

M. M. Woolfson. *The Origin and Evolution of the Solar System*. The Origin and Evolution of the Solar System, published by the Institute of Physics Publishing, Bristol, 2000., 2000.

C. Zanni, A. Ferrari, R. Rosner, G. Bodo, and S. Massaglia. MHD simulations of jet acceleration from Keplerian accretion disks. The effects of disk resistivity. *A&A*, 469:811–828, July 2007.

A life without friends is possible
but meaningless.

— based on Victor von Bülow

Acknowledgments

Thank you!

- Vero: porque me apoyas y me motivas y me iluminas el día y la noche.
- meiner Mutter: weil Du mich immer wieder motiviert hast und Rückschläge immer wieder mit Humor und Verständnis aufgenommen hast.
- meinem Vater: weil Du mir als Kind Turbomaschinen erklärt hast und damit wohl meine Begeisterung für die Strömungslehre begründet hast.
- Max Camenzind: weil Du immer an mich und meine Arbeit geglaubt hast und mich mit immer neuen Einsichten in die Welt der kompakten Objekte angetrieben hast.
- Hubert Klahr: weil mich unsere Gespräche über Codes, Planitesimale und Akkretion immer wieder aufs Neue inspiriert haben.
- Immo Appenzeller: weil Sie meine Begeisterung für die Astronomie in Ihren Vorlesungen nährten und mich nicht nur in der Diplomprüfung sondern nun auch in der Disputation begleiten.
- Ulrich Platt: weil Sie sich sofort bereit erklärten, mein Prüfer zu sein.
- John Miller and the SISSA group: because I learned a lot about passion and science in Trieste.
- Silvano Massaglia, Andrea Mignone e il gruppo di Torino: perché mi hanno ricevuto con grande amicizia a Torino e mi hanno aiutato a conoscere e dominare PLUTO.
- Thomas Mädler: weil wir, wenn alle anderen schon unter dem Tisch liegen, immer noch über schwarze Löcher reden können
- Damian 'Bambam' Mädler Jofre: weil Dein Lachen einfach ansteckend ist.
- Der Theoriegruppe der Sternwarte und der Planetengruppe des MPIA: weil es einfach Spaß macht, solche Kollegen zu haben.
- Ciani und Iyari: weil Ihr mich mit Eurem Lachen immer wieder daran erinnert, was wirklich wichtig ist. Und weil Ihr mich am Wochenende meist erfolgreich davon abhaltet, über Akkretion nachzudenken.